ISSN 1997-308X
eISSN 2412-8767

ИЗВЕСТИЯ ВУЗОВ
ПОРОШКОВАЯ МЕТАЛЛУРГИЯ И ФУНКЦИОНАЛЬНЫЕ ПОКРЫТИЯ

POWDER METALLURGY AND FUNCTIONAL COATINGS

2023
Том 17 № 1
Vol. 17 No. 1
powder.misis.ru

ISSN 1997-308X
eISSN 2412-8767

POWDER METALLURGY AND FUNCTIONAL COATINGS

Scientific and Technical Journal
Founded in 2007
Four issues per year

2023
Vol. 17 No. 1
Том 17 № 1

ИЗВЕСТИЯ ВУЗОВ
ПОРОШКОВАЯ МЕТАЛЛУРГИЯ И ФУНКЦИОНАЛЬНЫЕ ПОКРЫТИЯ

Научно-технический журнал
Основан в 2007 г.
Выходит 4 раза в год

POWDER METALLURGY AND FUNCTIONAL COATINGS

SCIENTIFIC AND TECHNICAL JOURNAL
FOUNDED IN 2007
FOUR ISSUES PER YEAR

http://powder.misis.ru

ISSN 1997-308X
eISSN 2412-8767

Founder:

National University of Science
and Technology "MISIS"
Address: 4 Leninskiy Prosp., Moscow 119049, Russian Federation
http://www.misis.ru

Editor-in-Chief

Evgeny A. Levashov
Prof., Dr. Sci. (Eng.), Acad. of the RANS, NUST MISIS, Moscow, Russian Federation

Journal is included into the List of peer-reviewed scientific publications recommended by the Highest Attestation Commission of the Ministry of Education and Science of the Russian Federation for publishing the results of doctoral and candidate dissertations.
Abstracting/Indexing: Scopus, Russian Science Citation Index (RSCI), Ulrich's Periodicals Directory, VINITI Database (Abstract Journal).

Editorial Board

M. I. Alymov – Dr. Sci. (Eng.), Corresponding Member of the RAS, Merzhanov Institute of Structural Macrokinetics and Materials Sciences of the RAS, Chernogolovka, Russia
A. P. Amosov – Prof., Dr. Sci. (Phys.-Math.), Samara State Technical University, Samara, Russia
G. A. Bagliuk – Prof., Dr. Sci. (Eng.), Acad. of the NASU, IPMS NASU, Kiev, Ukraine
I. V. Blinkov – Prof., Dr. Sci. (Eng.), NUST MISIS, Moscow, Russia
M. V. Chukin – Prof., Dr. Sci. (Eng.), Magnitogorsk State Technical University, Magnitogorsk, Russia
H. Danninger – Prof., Dr. Sci., Vienna University of Technology, Vienna, Austria
B. Derin – Assoc. Prof., Dr. Sci. (Phil.), Istanbul Technical University, Maslak, Istanbul, Turkey
V. Yu. Dorofeyev – Prof., Dr. Sci. (Eng.), South-Russian State Polytechnical University (NPI), Novocherkassk, Russia
Yu. Estrin – Prof., Dr. Sci. (Nat.), Monash University, Clayton, Australia
A. Ph. Ilyushchanka – Prof., Dr. Sci. (Eng.), Acad. of the NAS of Belarus, State Research and Production Powder Metallurgy Association, Minsk, Belarus
Yu. R. Kolobov – Prof., Dr. Sci. (Phys.-Math.), Federal Research Center of Problems of Chemical Pfysics and Medicinal Chemistry of the RAS, Chernogolovka, Russia
V. S. Komlev – Prof., Dr. Sci. (Eng.), Corresponding Member of the RAS, Institute of Metallurgy of the RAS, Moscow, Russia
I. Konyashin – Prof., Dr. Sci. (Econ.), Element Six GmbH, Burghaun, Germany
Yu. M. Korolyov – Prof., Dr. Sci. (Eng.), Scientific and Technical Association "Powder Metallurgy", Moscow, Russia
V. I. Kostikov – Prof., Dr. Sci. (Eng.), Corresp. Member of the RAS, NUST MISIS, Moscow, Russia
D. Yu. Kovalev – Dr. Sci. (Phys.-Math.), Merzhanov Institute of Structural Macrokinetics and Materials Sciences of the RAS, Chernogolovka, Russia
S. A. Kulinich – Assoc. Prof., PhD (Chem.), Tokai University, Hiratsuka, Kanagawa, Japan
S. V. Kuzmin – Prof., Dr. Sci. (Eng.), Corresponding Member of the RAS, Volgograd State Technical University, Volgograd, Russia
V. P. Kuznetsov – Prof., Dr. Sci. (Eng.), Ural Federal University, Ekaterinburg, Russia
Yu. V. Levinsky – Prof., Dr. Sci. (Eng.) Merzhanov Institute of Structural Macrokinetics and Materials Sciences of the RAS, Chernogolovka, Russia
A. E. Ligachyov – Prof., Dr. Sci. (Phys.-Math.), Prokhorov General Physics Institute of the RAS, Moscow, Russia
V. Yu. Lopatin – Cand. Sci., NUST MISIS, Moscow, Russia
A. A. Lozovan – Prof., Dr. Sci (Eng.), Moscow Aviation Institute (NRU), Moscow, Russia
V. I. Lysak – Prof., Dr. Sci. (Eng.), Acad. of the RAS, Volgograd State Technical University, Volgograd, Russia
A. V. Makarov – Dr. Sci. (Eng.), Corresponding Member of the RAS, M.N. Mikheev Institute of Metal Physics of the Ural Branch of the RAS, Ural Federal University, Ekaterinburg, Russia
L. L. Mishnaevsky – Dr. Habil. (Eng.), Technical University of Denmark, Roskilde, Denmark
A. S. Mukasyan – Prof., Dr. Sci. (Phys.-Math.), University of Notre Dame College of Engineering, Notre Dame, USA
S. A. Oglezneva – Prof., Dr. Sci. (Eng.), Perm National Research Polytechnical University, Perm, Russia
S. S. Ordanian – Prof., Dr. Sci. (Eng.), St. Petersburg State Technological Institute (Technical University), St. Petersburg, Russia
R. Orrù – Prof., Dr. Sci. (Eng.), University of Cagliari, Cagliari, Italy
I. B. Panteleev – Prof., Dr. Sci. (Eng.), St. Petersburg State Technological Institute (Technical University), St. Petersburg, Russia
F. Peizhong – Prof., Dr. Sci., China University of Mining and Technology, Xuzhou, P.R. China
C. Pengwan – Prof., Dr. Sci., Beijing Institute of Technology, Beijing, P.R. China
M. I. Petrzhik – Dr. Sci. (Eng.), NUST MISIS, Moscow, Russia
Yu. S. Pogozhev – Assoc. Prof., Cand. Sci. (Eng.), NUST MISIS, Moscow, Russia
V. V. Polyakov – Prof., Dr. Sci. (Phys.-Math.), Altai State University, Barnaul, Russia
A. A. Popovich – Prof., Dr. Sci. (Eng.)., Corresp. Member of the RANS, St. Petersburg State Polytechnical University (National Research University), St. Petersburg, Russia
S. E. Porozova – Dr. Sci. (Eng.), Perm National Research Polytechnical University, Perm, Russia
A. A. Rempel – Prof., Dr. Sci. (Eng.), Acad. of the RAS, Institute of Metallurgy of the Ural Branch of the RAS, Ekaterinburg, Russia
F. Rustichelli – Prof., Dr. Sci. (Phys.), University of Marches, Ancona, Italy
S. D. Shlyapin – Prof., Dr. Sci. (Eng.), Moscow Aviation Institute (NRU), Moscow, Russia
D. V. Shtansky – Dr. Sci. (Phys.-Math.), NUST MISIS, Moscow, Russia
P. A. Vityaz' – Prof., Dr. Sci. (Eng.), Acad. of the NAS of Belarus, Minsk, Belarus
A. A. Zaitsev – Assoc. Prof., Cand. Sci. (Eng.), NUST MISIS, Moscow, Russia
Zh. YongTing – Prof., Dr. Sci., Harbin Institute of Technology, Harbin, P.R. China
F. Zhengyi – Prof., Dr. Sci., Wuhan University of Technology, Wuhan, P.R. China

Editorial Staff

Address: NUST MISIS,
build 1, 4, Leninskiy Prosp., Moscow 119049, Russian Federation

Phone: +7 (495) 638-45-35. ***E-mail:*** izv.vuz@misis.ru

Certificate of registration **No. FS77-27955** (12.04.2007)
Re-registration **PI No. FS77-79230** (25.09.2020)

PM & FC © NUST MISIS, Moscow, 2023

Articles are available under Creative Commons
Attribution Non-Commercial No Derivatives

Leading Editor: A.A. Kudinova
Executive Editor: O.V. Sosnina
Layout Designer: V.V. Rasenets

Signed print 14.03.2023. Format 60×90 $^1/_8$
Offset paper No. 1. Digital printing. Quires 10.5
Order 16913. Free price
Printed in the printing house of the MISIS Publish House
4 bld. 1 Leninskiy Prosp., Moscow, 119049 Russian Federation
Phone/fax: +7 (499) 236-76-17

ИЗВЕСТИЯ ВУЗОВ ПОРОШКОВАЯ МЕТАЛЛУРГИЯ И ФУНКЦИОНАЛЬНЫЕ ПОКРЫТИЯ

НАУЧНО-ТЕХНИЧЕСКИЙ ЖУРНАЛ
ОСНОВАН В 2007 Г.
ВЫХОДИТ 4 РАЗА В ГОД

http://powder.misis.ru

ISSN 1997-308X
eISSN 2412-8767

Учредитель:

МИСИС
УНИВЕРСИТЕТ
НАУКИ И ТЕХНОЛОГИЙ

ФГАОУ ВО Национальный исследовательский
технологический университет «МИСИС»
Адрес: 119049, Москва, Ленинский пр-т, 4
https://www.misis.ru

Главный редактор

Евгений Александрович Левашов
д.т.н., академик РАЕН, профессор, НИТУ МИСИС, г. Москва

Журнал включен в Перечень рецензируемых научных изданий, рекомендованных ВАК Минобрнауки РФ для публикации результатов диссертаций на соискание ученых степеней.
Журнал включен в базы данных: Scopus, Russian Science Citation Index (RSCI), Ulrich's Periodicals Directory, РИНЦ, БД/РЖ ВИНИТИ.

Редакционная коллегия

М. И. Алымов – д.т.н., чл.-корр. РАН, проф., ИСМАН, г. Черноголовка
А. П. Амосов – д.ф.-м.н., проф., СамГТУ, г. Самара
Г. А. Баглюк – д.т.н., акад. НАНУ, проф., ИПМ НАН Украины, г. Киев
И. В. Блинков – д.т.н., проф., НИТУ МИСИС, г. Москва
П. А. Витязь – д.т.н., акад. НАНБ, проф., НАН Беларуси, г. Минск
В. Ю. Дорофеев – д.т.н., проф., ЮРГПУ (НПИ), г. Новочеркасск
А. А. Зайцев – к.т.н., доц., НИТУ МИСИС, г. Москва
А. Ф. Ильющенко – д.т.н., акад. НАН Беларуси, проф., ГНПО ПМ НАН Беларуси, г. Минск
Д. Ю. Ковалев – д.ф.-м.н., ИСМАН, г. Черноголовка
Ю. Р. Колобов – д.ф.-м.н., проф., ФИЦ ПХФ и МХ РАН, г. Черноголовка
В. С. Комлев – д.т.н., чл.-корр. РАН, проф., ИМЕТ РАН, г. Москва
Ю. М. Королев – д.т.н., проф., НТА «Порошковая металлургия», г. Москва
В. И. Костиков – д.т.н., чл.-корр. РАН, проф., НИТУ МИСИС, г. Москва
В. П. Кузнецов – д.т.н., проф., УрФУ, г. Екатеринбург
С. В. Кузьмин – д.т.н., чл.-корр. РАН, проф., ВолгГТУ, г. Волгоград
Ю. В. Левинский – д.т.н., проф., ИСМАН, г. Черноголовка
А. Е. Лигачев – д.ф.-м.н., проф., ИОФ РАН, г. Москва
А. А. Лозован – д.т.н., проф., МАИ (НИУ), г. Москва
В. Ю. Лопатин – к.т.н., доц., НИТУ МИСИС, г. Москва
В. И. Лысак – д.т.н., акад. РАН, проф., ВолгГТУ, г. Волгоград
А. В. Макаров – д.т.н., чл.-корр. РАН, ИФМ УрО РАН, УрФУ, г. Екатеринбург
С. А. Оглезнева – д.т.н., проф., ПНИПУ, г. Пермь
С. С. Орданьян – д.т.н., проф., СПбГТИ (ТУ), г. Санкт-Петербург
И. Б. Пантелеев – д.т.н., проф., СПбГТИ (ТУ), г. Санкт-Петербург
М. И. Петржик – д.т.н., проф., НИТУ МИСИС, г. Москва
Ю. С. Погожев – к.т.н., доц., НИТУ МИСИС, г. Москва
В. В. Поляков – д.ф.-м.н., проф., АлтГУ, г. Барнаул
А. А. Попович – д.т.н., чл.-корр. РАЕН, проф., СПбГПУ, г. Санкт-Петербург
С. Е. Порозова – д.т.н., проф., ПНИПУ, г. Пермь
А. А. Ремпель – д.т.н., акад. РАН, проф., ИМЕТ УрО РАН, г. Екатеринбург
М. В. Чукин – д.т.н., проф., МГТУ, г. Магнитогорск
С. Д. Шляпин – д.т.н., проф., МАИ (НИУ), г. Москва
Д. В. Штанский – д.ф.-м.н., проф. НИТУ МИСИС, г. Москва
C. Pengwan – Dr. Sci., Prof., Beijing Institute of Technology, Beijing, P.R. China
H. Danninger – Dr. Sci., Prof., Vienna University of Technology, Vienna, Austria
B. Derin – Dr. Sci. (Phil.), Assoc. Prof., Istanbul Technical University, Maslak, Istanbul, Turkey
Yu. Estrin – Dr. Sci. (Nat.), Prof., Monash University, Clayton, Australia
F. Peizhong – Dr. Sci., Prof., China University of Mining and Technology, Xuzhou, P.R. China
F. Zhengyi – Dr. Sci., Prof., Wuhan University of Technology, Wuhan, P.R. China
I. Konyashin – Dr. Sci. (Econ.), Prof., Element Six GmbH, Burghaun, Germany
S. A. Kulinich – PhD (Chem.), Associate Prof., Tokai University, Hiratsuka, Kanagawa, Japan
L. L. Mishnaevsky – Dr. Habil. (Eng.), Technical University of Denmark, Roskilde, Denmark
A. S. Mukasyan – Dr. Sci. (Phys.-Math.), Prof., University of Notre Dame College of Engineering, Notre Dame, USA
R. Orrù – Dr. Sci. (Eng.), Prof., University of Cagliari, Cagliari, Italy
F. Rustichelli – Dr. Sci. (Phys.), Prof., University of Marches, Ancona, Italy
Zh. YongTing – Dr. Sci., Prof., Harbin Institute of Technology, Harbin, P.R. China

---

Редакция журнала

Адрес: 119049, Москва,
Ленинский пр-т, 4, стр. 1. НИТУ МИСИС

Тел.: +7 (495) 638-45-35. ***Эл. почта:*** izv.vuz@misis.ru

Свидетельство о регистрации № **ФС77-27955** от 12.04.2007 г.
Перерегистрация 25.09.2020 г. **ПИ № ФС77-79230**

ПМ и ФП
ИЗВЕСТИЯ ВУЗОВ

© НИТУ МИСИС, Москва, 2023

BY NC ND

Статьи доступны под лицензией Creative Commons Attribution Non-Commercial No Derivatives

Ведущий редактор: А.А. Кудинова
Выпускающий редактор: О.В. Соснина
Дизайн и верстка: В.В. Расенець

Подписано в печать 14.03.2023. Формат 60×90 $^1/_8$
Бум. офсетная № 1. Печать цифровая. Усл. печ. л. 10,5
Заказ 16913. Цена свободная
Отпечатано в типографии Издательского Дома МИСИС
119049, г. Москва, Ленинский пр-т, 4, стр. 1
Тел./факс: +7 (499) 236-76-17

Contents

Theory and Processes of Formation and Sintering of Powder Materials

Self-Propagating High-Temperature Synthesis

Nanostructured Materials and Functional Coatings

Application of Powder Materials and Functional Coatings

Содержание

Теория и процессы формования и спекания порошковых материалов

Самораспространяющийся высокотемпературный синтез

Наноструктурированные материалы и функциональные покрытия

Применение порошковых материалов и функциональных покрытий

Theory and Processes of Formation and Sintering of Powder Materials
Теория и процессы формования и спекания порошковых материалов

UDC 621.762

https://doi.org/10.17073/1997-308X-2023-1-5-11

Research article
Научная статья

Obtaining and properties of rolled products from clad powders NPG-80 and Nibon-20

I. M. Mal'tsev ✉, Yu. A. Getmanovsky

Nizhny Novgorod State Technical University named after R.E. Alekseev (NNSTU)
24 Minina Str., Nuzhny Novgorod 603950, Russian Federation

✉ Maltcev@nntu.ru

Abstract. Antifriction tape sealing materials (TSM) are used in the manufacture of turbines. This work studied the mechanism of the increase in thickness of rolled products. The study showed that internal oxides of powder particles, which are reduced during sintering and annealing in hydrogen, cause a change in the size of tapes and compacts from NPG-80 and Nibon-20 clad powders. The distinctive feature of powders used in the work is the presence of a nickel shell around the particle of the solid lubricant (graphite or boron nitride). It was shown that an increase in sintering temperature and heating time to isothermal holding intensifies the growth of the tapes and samples The studies carried out point to a relationship between reduction processes occurring in hydrogen during heating, sintering, and annealing of NPG-80 and Nibon-20 powders with an increase in the thickness of the tape containing the solid lubricant in its composition. An increase in the duration of heating to isothermal holding at 1150 °C is accompanied by an increase in the thickness of rolled stock. Sintering of TSM Nibon-20 in the first mode (4 h to 1150 °C) gives an increase in thickness by 5–7 %, whereas sintering in the second mode (9 h to 1150 °C) gives an increase of 12–13 %. For NPG-80, the increase in thickness is 3–7 % and 8–11 %, respectively. This leads to some decrease in the physical and mechanical properties of TSM. Lower temperatures and higher heating rates are recommended for the sintering of sheet materials from NPG-80 and Nibon-20 in the hydrogen atmosphere. The increase in thickness of TSM from clad powders NPG-80 and Nibon-20 can be avoided if the sintering (heating) is carried out under pressure. By the method of electric rolling and subsequent hot rolling TSM is obtained from Nibon-20.

Keywords: turbines, sealing materials, rolling, clad powders, NPG-80, Nibon-20, electric rolling, annealing, sintering, properties

For citation: Mal'tsev I.M., Getmanovsky Yu.A. Obtaining and properties of rolled products from clad powders NPG-80 and Nibon-20. *Powder Metallurgy and Functional Coatings*. 2023;17(1):5–11. https://doi.org/10.17073/1997-308X-2023-1-5-11

Получение и свойства проката из плакированных порошков НПГ-80 и Нибон-20

И. М. Мальцев ✉, Ю. А. Гетмановский

Нижегородский государственный технический университет им. Р.Е. Алексеева
Россия, 603950, г. Нижний Новгород, ул. Минина, 24

✉ Maltcev@nntu.ru

Аннотация. При изготовлении турбин применяются антифрикционные ленточные уплотнительные материалы (ЛУМ). Проведено изучение механизма роста толщины проката. Установлено, что внутренние оксиды частиц порошка, восстанавливающиеся при спекании и отжиге в водороде, вызывают изменение размеров лент и прессовок из плакированных порошков НПГ-80 и Нибон-20. Отличительной особенностью используемых в работе порошков является наличие вокруг частицы твердой смазки (графита или нитрида бора) оболочки из никеля. Показано, что повышение температуры спекания и времени нагрева до изотермической выдержки интенсифицирует рост лент и образцов. Проведенные исследования свидетельствуют о связи восстановительных процессов, протекающих в водороде при спекании и отжиге порошков НПГ-80 и Нибон-20, содержащих в своем составе твердую смазку, с ростом толщины ленты. Увеличение продолжительности нагрева до изотермической выдержки при температуре 1150 °С сопровождается ростом толщины проката. Спекание ЛУМ Нибон-20 по 1-му режиму (4 ч до 1150 °С) создает прирост толщины на 5–7 %, а по 2-му (9 ч до 1150 °С) – на 12–13 %. Для НПГ-80 увеличение толщины призошло на 3–7 и 8–11 % соответственно. Вследствие этого происходит снижение физико-механических свойств ЛУМ. Для спекания в атмосфере водорода листовых материалов из НПГ-80 и Нибон-20 предпочтительно использование более низких температур и более высоких скоростей нагрева. Возможно устранение роста толщины ЛУМ из плакированных порошков НПГ-80 и Нибон-20 применением спекания (нагрева) под давлением. Методом электропрокатки и последующей горячей прокатки получен ЛУМ из порошка Нибон-20 при отсутствии роста толщины материала.

Ключевые слова: турбины, уплотнительные материалы, прокатка, плакированные порошки, НПГ-80, Нибон-20, электропрокатка, отжиг, спекание, свойства

Для цитирования: Мальцев И.М., Гетмановский Ю.А. Получение и свойства проката из плакированных порошков НПГ-80 и Нибон-20. *Известия вузов. Порошковая металлургия и функциональные покрытия*. 2023;17(1):5–11. https://doi.org/10.17073/1997-308X-2023-1-5-11

Introduction

Antifriction tape sealing materials (TSM) are used in the manufacture of turbines. TSM close the gap between the turbine blades and the turbine housing. The tapes must have a specific set of properties, e.g., wear out when a turbine blade cuts into them, have a low coefficient of friction and have heat resistance and heat stability. Most commonly, for the creation of TSM, powder metallurgy methods are used. Powder materials for TSM are compositions from a matrix on a nickel or nichrome base with inclusions of solid lubricants (hexagonal boron nitride ($_h$BN) with a crystal lattice similar to graphite and also graphite) evenly distributed in it and are characterized by a certain level of porosity.

The main forming techniques used for the processing of such materials are extrusion and roll forming. At present, tape roll forming from composite powder materials has been successfully introduced on an industrial scale at PJSC Vyksunsky Metallurgical Plant (Vyksa, Porous Rolled Stock Production Unit) [1–8]. Industrial technology of TSM comprises charge preparation, strip rolling, sintering and hot rolling to clad the primary powder material with compact heat-resistant substrates.

TSM rolling technology features a set of technological hindrances: difficulties in forming highly fluid powder compositions, restrictions on the amount of introduced non-forming powder phase (solid lubricant), and the formation of a film from a layer of solid lubricants particles on rolling mill rolls. These factors are detrimental to the rolling forming.

This work studied the mechanism of the increase in thickness of rolled products. It was found that internal oxides of powder particles, which are reduced during sintering and annealing in hydrogen cause a change in the size of tapes and compacts from NPG-80 and Nibon-20 clad powders. The study revealed that an increase in sintering temperature and heating time to isothermal holding intensifies the growth of the tapes and samples. Particular features of sintering and annealing of the TSM were studied, and a new forming method of powder compositions by electric rolling has been developed to eliminate technological limitations that hinder the development of a new generation of TSMs containing up to 80 vol.% of solid lubricant particles. The aim of the study was to obtain materials from clad powders NPG-80 and Nibon-20 by rolling, including electric and hot rolling.

Materials and Methods

The distinctive feature of powders used in the work is the presence of a 9–12 μm thick nickel shell around the particle of the solid lubricant (graphite or boron nitride), see Fig. 1. Table 1 summarizes the technological properties and composition of powders used to obtain sheets; the sheets were rolled on 200 mm diameter rolls and sintered in two modes in hydrogen: mode *1* – heating for 4 h to t = 1150 °C, holding for 2 h at this temperature, cooling in a furnace down to 400 °C, and then in the air; mode *2* – heating for 9 h to t = 1150 °C, holding for 2 h, cooling in a furnace down to 400 °C and then in the air.

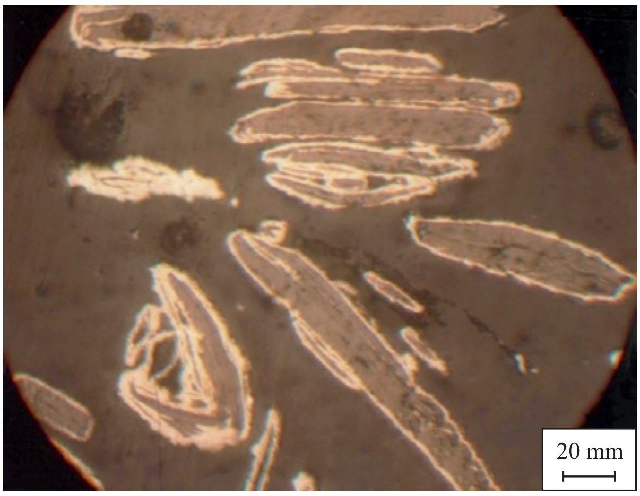

Fig. 1. The structure of the +0.100 mm size particles of the NPG-80 powder

Рис. 1. Структура частиц фракции +0,100 мм порошка НПГ-80

Table 1. **Technological properties and size range of powders**

Таблица 1. **Технологические свойства и фракционный состав порошков**

Powder type	Bulk density, g/cm^3	Tap density, g/cm^3	Size range, %, by particle size, mm					
			–0.400 +0.200	–0.200 +0.160	–0.160 +0.100	–0.100 +0.063	–0.063 +0.050	–0.050
Nibon-20	1.02	1.35	0.20	0.20	2.50	9.80	4.20	82.0
NPG-80	1.39	1.76	–	9.74	18.98	21.84	12.01	42.4

Table 2. **Influence of the sintering mode on the physical and mechanical properties of the tape**

Таблица 2. **Влияние режима спекания на физико-механические свойства ленты**

Sintering mode	Powder type	Tap density, g/cm^3	Porosity, %	σ_v, MPa	*HB*, MPa
1	NPG-80	3.90	30	3.80	24
	Nibon-20	3.84	31	2.90	–
2	NPG-80	3.60	35	2.50	15
	Nibon-20	3.26	42	2.66	–

A study of the tape properties after sintering showed that an increase in the duration of heating to isothermal holding at $t = 1150$ °C is accompanied by an increase in the thickness of the rolled product. Sintering of the tape from Nibon-20 powder in mode *1* leads to an increase in thickness by 5–7 %, whereas sintering in mode 2 gives a thickness increase of 12–13 %. For NPG-80, the increase in thickness is 3–7 % and 8–11 %, respectively. This, in turn, leads to worsening of physical and mechanical properties of the tape (see Table 2).

A change in the material properties also occurs when the samples are annealed in hydrogen for 2 h at $t = 950$ °C after sintering and subsequent hot rolling (Table 3). Similarly to sintering, annealing also leads to the thickening of the NPG-80 tape by 7 % and the Nibon-20 tape by 10 %. Repeated annealing of these tapes results in an increase in their thickness by 4–5 %. The observed changes in the geometry of the tapes lead to a deterioration of the properties of the antifriction sealing material due to an increase in porosity. To identify the causes associated with an increase in the thickness of powder rolled stock during sintering and annealing, the powders were reduced for 1 h at $t = 300$ °C in hydrogen. Table 4 shows the properties of the powders after annealing.

Table 3. **Properties of the powder tapes after annealing**

Таблица 3. **Свойства порошковых лент после отжига**

Material	Processing	σ_v, MPa	*HB*, MPa	Porosity, %	Tap density, g/cm^3
Nibon-20	Hot rolling	9.5	8.0	30	3.96
	Annealing	4.5	4.0	56	2.50
NPG-80	Hot rolling	21.0	28.0	28	4.80
	Annealing	18.0	17.0	30	4.60

Table 4. **Technological properties of the powders before and after the annealing**

Таблица 4. **Технологические свойства порошков до и после отжига**

Powder type	Powder condition	Size range, %, by particle size, mm						Bulk density, g/cm^3	Tap density, g/cm^3
		–0.400 +0.200	–0.200 +0.160	–0.160 +0.100	–0.100 +0.063	–0.063 +0.050	–0.050		
Nibon-20	Pre-annealing	0.6	0.2	2.5	9.8	4.2	82.0	1.02	1.35
	Post-annealing	2.6	0.2	7.3	17.0	16.5	56.4	0.89	1.02
NPG-80	Pre-annealing	–	9.7	19.0	21.8	12.0	42.4	1.39	1.76
	Post-annealing	1.1	3.6	19.7	29.0	8.8	32.5	1.01	1.25

The study of powders showed that the content of fine particles mainly changes during annealing (see Table 4). Besides, there is a decrease in the mass (by 5 %) of powder samples annealed in a reducing medium (hydrogen), which indicates a considerable oxidation of the powder in the as-received state. The study of the powder particles by the breakdown voltage method demonstrated that oxides are located both inside and outside the nickel shell. See [7; 8] for the details on the technique for determining the breakdown voltage of powder filling and the device used for the implementation of this technique. Experimentally measured average thickness of the oxide layer was $1.7\cdot10^{-5}$ mm, whereas the thickness of the shell determined microscopically had a mean value of $9\cdot10^{-3}$ mm. Measurement of the oxide layer of the shell of the powders after reduction showed that during annealing there is a sharp decrease in its thickness down to a value of $1.06\cdot10^{-6}$ mm.

The study of shrinkage kinetics during sintering on Nibon-20 samples of different density sintered in hydrogen at $t = 800$, 900, and 1000 °C revealed that an increase in the sintering temperature leads to a decrease in the samples' density (Fig. 2).

The reduction reactions occurring inside the nickel shell cause the formation of moisture, while heating creates an excess pressure of superheated vapours, leading to swelling of the powder particles and, consequently, an increase in the thickness of the TSM sample. These processes are intensified if the duration of heating to the temperature of isothermal sintering increases, when the process of thermal consolidation of particles has approximately the same rate as the reduction reaction (see Table 2). An increase in the initial density of the pellets creates the conditions for a greater decrease in density when the sintering temperature is increased (see Fig. 2). This is due to the fact that samples of clad particles have a higher gas pressure inside the shell when they first form a denser metal matrix, which prevents the gas from escaping from the clad particle during heating. The through porosity also decreases.

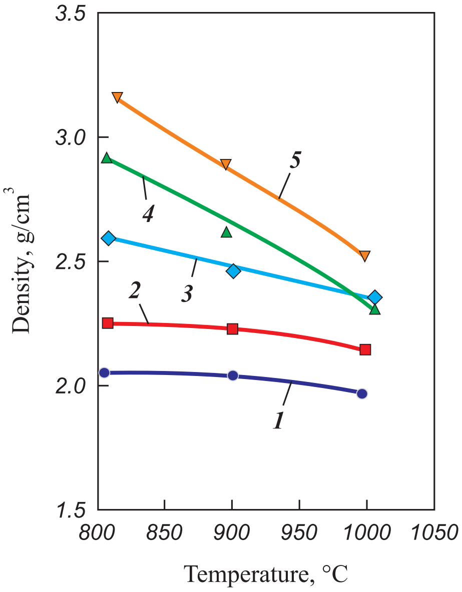

Fig. 2. The dependence of the density of Nibon-20 pellets on the sintering temperature
Extrusion pressure, t/cm^2: ***1*** – 0.5; ***2*** – 1.0; ***3*** – 1.5; ***4*** – 2.0; ***5*** – 2.5

Рис. 2. Зависимость плотности брикетов из Нибон-20 от температуры спекания
Давление прессования, т/см^2: ***1*** – 0,5; ***2*** – 1,0; ***3*** – 1,5; ***4*** – 2,0; ***5*** – 2,5

The *X*-ray phase analysis was not carried out due to technical difficulties in obtaining samples already containing 80 vol.% solid lubricant (graphite or boron nitride). The studies carried out demonstrated that sintering sheet materials from powders of solid lubricants clad with nickel in a hydrogen atmosphere to obtain the required properties is recommended in lower temperatures and at higher heating rates.

Overcoming the issue

The increase in thickness of TSM from clad powders NPG-80 and Nibon-20 can be avoided if the sintering (heating) is carried out under pressure. There are methods of rolling the powder, combined with its heating in a furnace placed above horizontally arranged rolls. In this case, difficulties arise with uniform heating of the powder bulk and its transfer into the forming zones. There are also methods of electric sintering in rolls with alternating electric current supplied to the rolls in different design options [2–4], however, there are issues associated with the stationarity of the rolling and electric sintering process.

NNSTU has developed a method for electric pulse sintering of metal powder and a device for the implementation of this method [5]. The device consists of a rolling mill and an electric pulse generator. A pulsed electric current with an adjustable duty cycle is supplied to the electrode rolls isolated from the rolling stand. Electric current runs directly between the rolls. To manufacture the TSM, high-density pulsed currents are used: 10^8–10^9 A/m^2.

The rolling of various powders and compositions at the electric rolling plant revealed the features of the technology of forming and sintering by a new method. The interrelation of particle sizes, their elastic properties and the reduction factor of the powder material with the type of the electric rolling process has been established. Based on the mathematical modelling of the temperature field in the particle–contact–particle system, a method of analytical calculations was developed. This method allows for determining the mechanism (solid- or liquid-phase) of the powder electric sintering process during rolling based on its known parameters of electric rolling and the technological, electrical, and physical properties of powders [6].

Experimental tape materials based on iron powders, corrosion-resistant steels, and composite materials have been obtained by the electric rolling method [6].

The solid lubricant particles of boron nitride in the TSM act as dielectric particles located in the conductive metal matrix of the material and affect the electric rolling. The properties of electrically rolled powder materials largely depend on the Joule effect ability – with the growth of the effect, the strength of interparticle contacts and the entire electrically rolled material increases. Electrical and physical effects that strengthen the material and the interparticle contact itself arise, if during forming of a metal powder by rolling and other forming methods, an electric current and an electromagnetic field are applied to the deformation zone [7; 8]. Here, the electrical and physical properties of the conductor material itself, the electric and plastic effect, and other effects have an important role, which attracts a lot of attention of foreign and domestic researchers [9–16].

The emergence of a pulsed electromagnetic field and the flow of current through the formed powder material have expanded the possibilities of the rolling forming technique. For example, the shedding of the edges of the tape during the rolling of highly fluid powders was eliminated, having a positive effect on the macrostructure of the powder tribotechnical sealing material. This was especially noticeable on such important powders as Nibon-20 and NPG-80, compositions of nichrome and boron nitride powders. The pinch effect, which leads to compression of the conducting powder body, increased the density of the material [7], which allowed for the obtaining of powder rolled stock with a higher interparticle contact strength [12].

Under the conditions of forming at low pressure (100 MPa) and concomitant passing of a high density current through the compact from Nibon-20 powder, a sealing powder material with a porosity of only 3 % was obtained. Other tape materials can also be produced by electric rolling. The results of studies in the field of electric compacting of metal powder materials show the hardening of metal materials under the influence of an electromagnetic field [13–20]. Modern technologies of metal materials processing use high-density currents [21–23].

The use of traditional elements of technology together with the introduction of electric rolling allowed for the developing of a new version of the technology for obtaining rolled TSM from Nibon-20 powder. The powder was rolled on an electric rolling plant [5] in rolls with a 0.2 m diameter and a width of 0.02 m with an electric current applied to the forming center. The properties of the finished strips were similar to the properties to rolled stock sintered in furnaces at a temperature of 900 °C. The resulting tapes were cut and placed in packages of 0.3 mm thick NP-2 nickel foil. The resulting assembly was subjected to hot rolling on an installation designed by NNSTU at a temperature of 850 °C with a degree of deformation of 20–25 % in a hydrogen medium. Fig. 3 shows the exterior of nickel-clad sealing materials.

Physical and mechanical properties of the obtained material meet the requirements for sealing elements of turbines, for example, for TSM based on nichrome with solid lubricant from boron nitride. For instance, the investigated material from Nibon-20 has a tensile strength of 130–135 MPa, a hardness of 80–86 MPa, a relative density of 94–95 %, and a thickness of the sealing material layer of 2.00–2.22 mm. The advantage of this material is the high content of the non-forming phase (boron nitride), which reaches 80 vol.% in TSM – an unprecedented case.

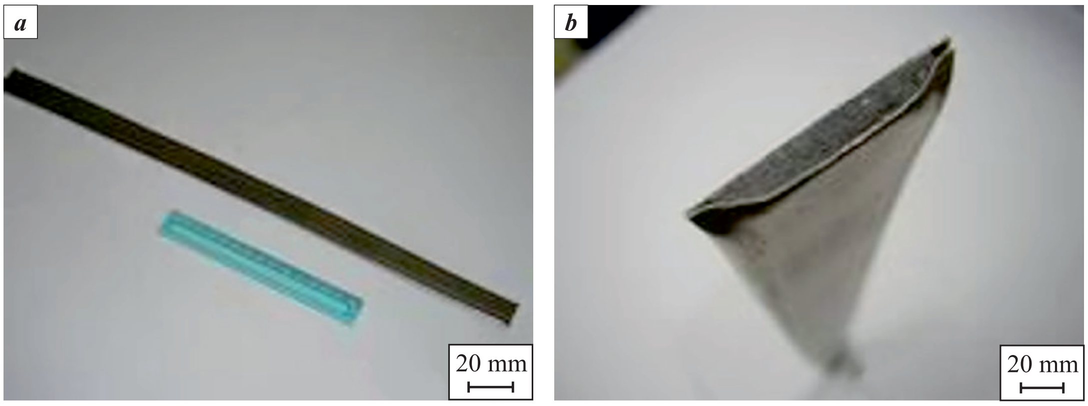

Fig. 3. Nickel-clad TSM element from Nibon-20 powder
a – the exterior of the tape, ***b*** – its cross-section

Рис. 3. Внешний вид элемента ЛУМ, плакированного никелем, из порошка Нибон-20
a – внешний вид ленты, ***b*** – ее торцевой срез

Fig. 4. The microstructure of TSM from NPG-80 powder after electric rolling and subsequent hot rolling
White substance – nickel, dark – graphite

Рис. 4. Микроструктура ЛУМ из порошка НПГ-80 после электропрокатки и последующей горячей прокатки
Белая структура – никель, темная – графит

Fig. 4 shows the structure of the TSM from NPG-80. In this case, a 5–20 μm thick metallic nickel matrix has a texture stretching along the direction of rolling.

Conclusion

The study showed that internal oxides of powder particles, which are reduced during sintering and annealing in hydrogen, cause a change in the size of tapes and compacts from NPG-80 and Nibon-20 clad powders. An increase in sintering temperature and heating time to isothermal holding intensifies the growth of the tapes and samples. The properties of TSMs containing solid lubricants depend on the rolling and sintering conditions.

The use of electric rolling for clad Nibon-20 and NPG-80 powders allows for forming of compositions containing up to 80 vol.% solid lubricant, the tape of this composition is suitable for subsequent hot rolling in packs. Such a technology allows to create TSM with a high content of graphite or boron nitride.

References / Список литературы

1. Sorokin V.K. Production of powdered products. Moscow: Metallurgizdat, 2002. 296 p. (In Russ.).

Сорокин В.К. Производство порошкового проката. М.: Металлургиздат, 2002. 296 с.

2. Olevsky E.A., Aleksandrova E.V., Ilyina A.M., Novoselov A.N., Pelve K.Yu., Grigoriev E.G. Electroconsolidation of powder materials. I. Methods of low and high-voltage consolidation. *Fizika i khimiya obrabotki materialov*. 2013;(2):53–64. (In Russ.).

Олевский Е.А., Александрова Е.В., Ильина А.М., Новоселов А.Н., Пельве К.Ю., Григорьев Е.Г. Электроконсолидация порошковых материалов. I. Методы низковольтной и высоковольтной консолидации. *Физика и химия обработки материалов*. 2013;(2):53–64.

3. Olevsky E.A., Aleksandrova E.V., Ilyina A.M., Novoselov A.N., Pelve K.Yu., Grigoriev E.G. Electroconsolidation of powder materials. II. Consolidated materials and simulation of the processes of consolidation. *Fizika i khimiya obrabotki materialov*. 2013;(4):45–68. (In Russ.).

Олевский Е.А., Александрова Е.В., Ильина А.М., Новоселов А.Н., Пельве К.Ю., Григорьев Е.Г. Электроконсолидация порошковых материалов. II. Консолидированные материалы и моделирование процессов консолидации. *Физика и химия обработки материалов*. 2013;(4):45–68.

4. Olevsky E.A., Aleksandrova E.V., Ilyina A.M., Dudina D.V., Novoselov A.N., Pelve K.Y., Grigoryev E.G. Outside mainstream electronic databases: Review of studies conducted in the USSR and post-soviet countries on electric current-assisted consolidation of powder materials. *Materials*. 2013;6(10):4375–4440.
https://doi.org/10.3390/ma6104375

5. Mal'tsev I.M., Petrikov V.G. Installation for electric pulsed sintering of conducting powders during rolling. *Powder Metallurgy and Metal Ceramics*. 1993;32(3):277–279.
https://doi.org/10.1007/BF00559764

6. Mal'tsev I.M. Properties of powdered electric rolling. *Zagotovitel'nye proizvodstva v mashinostroenii*. 2011;(9): 30–38. (In Russ.).

Мальцев И.М. Свойства порошкового электропроката. *Заготовительные производства в машиностроении*. 2011;(9):30–38.

7. Mal'tsev I.M. The effect of the electromagnetic field and skin and pinch effects on electrorolling metal powder materials under high-density pulse currents. *Russian Journal of Non-Ferrous Metals*. 2009;50(2):142–146.
https://doi.org/10.3103/S1067821209020138

8. Mal'tsev I.M. Electrical rolling of a metal powder in roll electrodes with a high-density current. *Russian Journal of Non-Ferrous Metals*. 2010;51(4):342–346.
https://doi.org/10.3103/S1067821210040152

9. Guan L., Tang G., Chu P.K. Recent advances and challenges in electroplastic manufacturing processing of metals. *Journal of Materials Research*. 2010;25(7):1215–1224.
https://doi.org/10.1557/JMR.2010.0170

10. Nguyen-Tran H.D., Oh H.S., Hong S.T, Han H.N, Cao J., Ahn S.H., Chun D.M. A review of electrically-assisted manufacturing. *International Journal of Precision Engineering and Manufacturing-Green Technology*. 2015;2(4):365–376.
https://doi.org/10.1007/s40684-015-0045-4

11. Xiang S., Xinfang Z. Dislocation structure evolution under electroplastic effect. *Materials Science and Engineering: A*. 2019;761:138026.
https://doi.org/10.1016/j.msea.2019.138026

12. Mal'tsev I.M. Research of electrorolled materials. *Zavodskaya laboratoriya. Diagnostika materialov*. 2018; 84(11):36–41. (In Russ.).
https://doi.org/10.26896/1028-6861-2018-84-11-36-41

Мальцев И.М. Исследование электропрокатаных материалов. *Заводская лаборатория. Диагностика материалов*. 2018;84(11):36–41.
https://doi.org/10.26896/1028-6861-2018-84-11-36-41

13. Pan L, He W., Gu B. Effects of electric current pulses on mechanical properties and microstructures of as-quenched

medium carbon steel. *Materials Science and Engineering: A*. 2016;662:404–411.
https://doi.org/10.1016/j.msea.2016.03.031

14. Tyler J., Grimm, Laine Mears. Electrically assisted pulse forming using closed-loop force control. *Journal of Manufacturing Processes*. 2021;71:528–540.
https://doi.org/10.1016/j.jmapro.2021.09.029

15. Morsi K., El-Desouky A., Johnson B., Mar A., Lanka S. Spark plasma extrusion (SPE): Prospects and potential. *Scripta Materialia.* 2009;61(4):395–398.
https://doi.org/10.1016/j.scriptamat.2009.04.026

16. Desouky A.El., Moon K.S., Kassegne S.K., Morsi K. Green Compact temperature evolution during current-activated tip-based sintering (CATS) of nickel. *Metals*. 2013;3(2):178–187.
https://doi.org/10.3390/met3020178

17. Zhyltsov A., Kondratenko I., Vasyuk V. Linear electromechanical transducer in the systems of welded joints of electrodynamic processing. In: *Handbook of research on energy-saving technologies for environmentally-friendly agricultural development*. IGI Global, 2020. P. 32.
https://doi.org/10.4018/978-1-5225-9420-8.ch016

18. Fais A., Actis Grande M., Forno I. Influence of processing parameters on the mechanical properties of Electro-Sinter-Forged iron based powders. *Materials & Design*. 2016;93:458–466.
https://doi.org/10.1016/j.matdes.2015.12.142

19. Deng H., Dong J., Boi F., Saunders T., Hu C., Grasso S. Magnetic field generated during electric current-assisted sintering: from health and safety issues to Lorentz force effects. *Metals*. 2020;10(12):1653.
https://doi.org/10.3390/met10121653

20. Wang Q., Ma Z., Wang X., Zhai Z. Study on the electromagnetic stress of the crack tip on a current-carrying metal plate. *Shenyang Jianzhu Gongcheng Xueyuan Xuebao (Ziran Kexue Ban)*. 2010;26(3):571–574.

21. Stolyarov V., Rubanik V. Cold rolling electrostimulation of hard-deform alloys. *Key Engineering Materials.* 2022;910:308–313. https://doi.org/10.4028/p-fcq55e

22. Pan L., He W., Gu B. Non-uniform carbon segregation induced by electric current pulse under residual stresses. *Journal of Materials Processing Technology*. 2015;226: 247–254. https://doi.org/10.1016/j.jmatprotec.2015.07.017

23. Sorokova S.N., Knyazeva A.G., Pobol A.I., Goranskyi G.G. Mathematical modeling of pulsed electro contact sintering of carbide powder composition. *Advanced Materials Research.* 2014;1040:495–499.
https://doi.org/10.4028/www.scientific.net/AMR.1040.495

Information about the Authors

Il'ya M. Mal'tsev – Cand. Sci. (Eng.), Associate Prof. of the Department "Materials science, technologies of materials and heat treatment of metals" of Nizhny Novgorod State Technical University (NNSTU) n.a. R.E. Alekseev
ORCID: 0000-00023464-9372
E-mail: Maltcev@nntu.ru

Yurii A. Getmanovsky – department assistant "Materials science, technologies of materials and heat treatment of metals" of NNSTU n.a. R.E. Alekseev
ORCID: 0000-0002-4338-3414
E-mail: getmanovskij@yandex.ru

Сведения об авторах

Илья Михайлович Мальцев – к.т.н, доцент кафедры «Материаловедение, технологии материалов и термическая обработка металлов», Нижегородский государственный технический университет (НГТУ) им. Р.Е. Алексеева
ORCID: 0000-00023464-9372
E-mail: Maltcev@nntu.ru

Юрий Андреевич Гетмановский – ассистент кафедры «Материаловедение, технологии материалов и термическая обработка металлов», НГТУ им. Р.Е. Алексеева
ORCID: 0000-0002-4338-3414
E-mail: getmanovskij@yandex.ru

Contribution of the Authors

I. M. Mal'tsev – research guidance, basic concept statement, statement of research goals and objectives, drawing conclusions, calculations conducting, samples testing, research results analysis, text writing and correction.

Yu. A. Getmanovsky – preparation, conducting and management of experiments, resources provision, research results processing.

Вклад авторов

И. М. Мальцев – руководство исследованием, постановка основной концепции, постановка целей и задач исследования, формулирование выводов, проведение расчетов, тестирование образцов, анализ результатов исследования, написание и корректировка текста.

Ю. А. Гетмановский – подготовка, проведение и руководство экспериментами, ресурсное обеспечение, обработка результатов исследований.

Received 23.03.2022
Revised 29.04.2022
Accepted 11.05.2022

Статья поступила 23.03.2022 г.
Доработана 29.04.2022 г.
Принята к публикации 11.05.2022 г.

Theory and Processes of Formation and Sintering of Powder Materials
Теория и процессы формования и спекания порошковых материалов

UDC 621.318.122

https://doi.org/10.17073/1997-308X-2023-1-12-20

Research article
Научная статья

Prediction of the concentration inhomogeneity of powder magnetic hard alloys based on the Fe–Cr–Co–Mo system and the effect of Sm additions on their magnetic properties

M. A. Marieva ✉, A. A. Shatsov

Perm National Research Polytechnic University
29 Komsomolskiy Prosp., Perm 614990, Russian Federation

✉ marievamar@rambler.ru

Abstract. Hysteresis alloys based on Fe–Cr–Co system are extensively used in the instrument-making industry as a material for synchronous motors of navigation systems, in the electronic industry, and other mechanical engineering fields. The following requirements are imposed on Fe–Cr–Co alloys: temperature stability of magnetic characteristics over time, manufacturability, low porosity and concentration inhomogeneity, which allow to obtain high-quality magnetic and mechanical properties. Materials based on conventional alloying systems, such as Fe–Cr–Co, have outlived themselves. An urgent line of the development of new materials and improvement of the properties of existing ones is alloying with rare-earth metals. The effect produced by Sm addition on powder analogs of Fe–Cr–Co system remains unstudied. In this paper, 22Kh15K4MS powder magnetic hard alloy alloyed with samarium in an amount of 0.5 wt. % was studied. The billets were obtained by cold pressing at a pressure of 600 MPa followed by vacuum sintering. The concentration inhomogeneity of Cr, Co, Mo, Sm was determined after 12 different sintering modes. A model of diffusion homogenization of ridge alloys, which allows to numerically evaluate the effect of sintering modes on the concentration inhomogeneity, was plotted. The distributions of chromium, cobalt, and molybdenum correspond to the asymptotically logarithmically normal law. Samarium is unevenly distributed in the structure. The effect of samarium additions on the magnetic properties of the alloy has been demonstrated. The alloying of 22Kh15K4MS alloy with 0.5 wt. % of samarium allows to obtain powder hysteresis magnets with a coercive force in the range from 3.9 to 33.0 kA/m and a residual magnetic induction from 0.44 to 0.95 T.

Keywords: hard magnetic alloy, powder alloy, magnetic properties, concentration inhomogeneity, diffusion, concentration variation coefficient, Fe– Cr–Co–Mo

For citation: Marieva M.A., Shatsov A.A. Prediction of the concentration inhomogeneity of powder magnetic hard alloys based on the Fe–Cr–Co–Mo system and the effect of Sm additions on their magnetic properties. *Powder Metallurgy and Functional Coatings*. 2023;17(1):12–20. https://doi.org/10.17073/1997-308X-2023-1-12-20

Прогнозирование концентрационной неоднородности порошковых магнитотвердых сплавов на основе системы Fe–Cr–Co–Mo и влияние добавок Sm на их магнитные свойства

М. А. Мариева ✉, А. А. Шацов

Пермский национальный исследовательский политехнический университет
Россия, 614990, г. Пермь, Комсомольский пр-т, 29

marievamar@rambler.ru

Аннотация. Гистерезисные сплавы на основе системы Fe–Cr–Co широко применяют в приборостроении в качестве материала для синхронных двигателей навигационных систем, в электронной промышленности и других областях машиностроения. К сплавам Fe–Cr–Co предъявляется ряд требований: температурная стабильность магнитных характеристик во времени, технологичность изготовления, низкая пористость и концентрационная неоднородность, – позволяющих добиваться сочетания высоких магнитных и механических свойств. Материалы на основе традиционных систем легирования, такие как Fe–Cr–Co, исчерпывают себя. Актуальным направлением при разработке новых материалов и повышении свойств существующих является легирование редкоземельными металлами. Эффект, производимый добавкой Sm на порошковые аналоги системы Fe–Cr–Co, остается неизученным. В работе исследован магнитотвердый порошковый сплав 22Х15К4МС, легированный самарием в количестве 0,5 мас. %. Заготовки получены методом холодного прессования при давлении 600 МПа и последующим спеканием в вакууме. Определена концентрационная неоднородность Cr, Co, Mo, Sm после 12 различных режимов спекания. Построена модель диффузионной гомогенизации гребневых сплавов, позволяющая численно оценивать влияние режимов спекания на концентрационную неоднородность. Распределения хрома, кобальта и молибдена соответствуют асимптотически логарифмически нормальному закону, самарий распределен в структуре неравномерно. Показано влияние добавок самария на магнитные характеристики сплава. Легирование сплава 22Х15К4МС самарием в количестве 0,5 мас. %. позволяет получать порошковые гистерезисные магниты с коэрцитивной силой 3,9–33,0 кА/м и остаточной магнитной индукцией 0,44–0,95 Тл.

Ключевые слова: магнитотвердый сплав, порошковый сплав, магнитные свойства, концентрационная неоднородность, диффузия, коэффициент вариации концентрации, Fe–Cr–Co–Mo

Для цитирования: Мариева М.А., Шацов А.А. Прогнозирование концентрационной неоднородности порошковых магнитотвердых сплавов на основе системы Fe–Cr–Co–Mo и влияние добавок Sm на их магнитные свойства. *Известия вузов. Порошковая металлургия и функциональные покрытия*. 2023;17(1):12–20.
https://doi.org/10.17073/1997-308X-2023-1-12-20

Introduction

In order to obtain materials with specified characteristics, it is necessary to establish the relationship between structure and properties [1]. Porosity and concentration inhomogeneity have a considerable effect on the processes of structure formation and magnetic properties of alloys [2–4], reducing their mechanical, physical and performance characteristics [5]. The inhomogeneity of alloys is estimated using diffusion coefficients [6–8], however, their determination does not allow to predict the concentration inhomogeneity with reasonable accuracy, since it is associated not only with diffusion, but also depends on a number of other factors [9; 10]. The study of diffusion at the stage of sintering of powder materials is performed using diffusion couples, however, the application of this method within multicomponent systems results in considerable experimental difficulties [11; 12]. The numerical methods for solving homogenization equations [13–15] do not take into account the properties of powder particles, their shape and defectiveness, and models based on statistical processing of data on diffusion homogenization provide only qualitative information on the element distribution. One of the modern approaches to the study of diffusion is the experimental study of homogenization patterns [13].

In work [16], the non-monotonic effect of concentration inhomogeneity on the magnetic properties of a material was proved experimentally. Furthermore, there is an approach based on the assertion that the homogenization process has a noticeable effect on the properties due to a change in the phase composition and distribution of phases, and a parallel transformation of the porous structure. In this paper, such a statistical value as concentration variation coefficient (V) was taken as a criterion for the inhomogeneity of the alloying element distribution. The technique allows to determine and predict the inhomogeneity and distribution of elements, provides a criterion for comparing the homogeneity of powder steels and alloys, allows to select the composition of materials and the technology for their production. The validity of this method for assessing inhomogeneity has been repeatedly confirmed in works [1; 11].

Recently, the alloys based on Fe–Cr–Co system with alloying additions, including rare-earth metals, have been extensively studied. The ferromagnetic materials based on $SmCo_5$, Sm_2Co_{17} compounds are widely used for the production of permanent magnets [17]. They exhibit a high Curie temperature, anisotropy field, and remanence, but exhibit high hardness and poor processibility. The alloys of Fe–Cr–Co system exhibit a high temperature stability, corrosion resistance, ductility and lower production costs compared to hard magnets made of rare-earth metals. In work [18], the alloying of a cast alloy of Fe–Cr–Co system with samarium up to 2 wt. % resulted in a significant increase in its magnetic properties: $BH_{\max}$ by 86 %, B_r by 47 %, and H_c by 28.7 %. The described approach to the alloying of chromel-copel alloys is of scientific and practical interest, however, the impact of concentration inhomogeneity on the effect of samarium additions has not been studied.

The study is aimed at the development of a homogenization model for predicting the modes of sintering of concentration-inhomogeneous powder hard magnetic alloys based on Fe–Cr–Co system with samarium.

Research methodology

This paper investigates the samarium-alloyed 22Kh15K4MS powder alloy, which exhibits the following chemical composition, wt. %:

Fe	Cr	Co	Mo	Si	Sm
57.0	22.5	15.0	4.0	1.0	0.5

The following powders of metals and alloys were used as initial components of the charge: chromium PKh-1S (TU 14-5-298-99, average particle size r = 10 µm, standard deviation σ = 5 µm); cobalt GP-OK (TU 1793-008-92, r = 24 µm, σ = 13 µm); iron OSCh 6-2 (TU 6-09-05808008-262-92, r = 2 µm, σ = 2 µm); ferrosilicon FS50 (GOST 1415-93-92, r = 8 µm, σ = 4 µm); molybdenum MPCh (TU 48-19-69-80, r = 2 µm, σ = 1 µm); samarium-cobalt (GOST 21559-76, r = 39 µm, σ = 21 µm).

The charge was sieved through a mesh with a cell size of 63 µm and averaged in a mixer with a shifted rotation axis for 8 h.

The sample billets were obtained by cold pressing at a pressure of 600 MPa, followed by vacuum sintering with a residual pressure of 10^{-2} Pa according to the modes specified in Table 1.

The sintering temperature range was selected on the basis of the fact that sintering at temperatures below 1200 °C results in obtaining magnets with a non-magnetic γ-phase production. Increasing the sintering temperature up to 1400 °C causes the evaporation of components from the surface of the billets. In both cases, these processes lead to the deterioration of the magnetic properties of the alloy [19].

All samples were quenched in 15 % aqueous NaCl solution at the temperature starting from 1250 °C. The aging of the billets was performed sequentially at 9 stages, and the processing indices are provided in Table 2. The main parameters and the shape of the magnetic hysteresis loop of the test samples were determined by means of "Permagraph L" hysteresis graph (Magnet-Physik, Germany) with PERMA software after the quenching and multistage aging.

Table 1. **The sintering modes of 22Kh15K4MS alloy with 0.5 wt. % Sm**

Таблица 1. **Режимы спекания сплава 22Х15К4МС с 0,5 мас. % Sm**

Sample No.	Sintering temperature, °C	Holding time, h
1	1250	1, 3, 8
2	1300	
3	1350	
4	1380	

To examine the patterns of changes in the concentration inhomogeneity of element distribution during sintering, the concentrations of Cr, Co, Mo, and Sm were measured at 100 points being equidistant from each other on the surface of the section. The concentrations were measured by the method of X-ray microanalysis, using "Tescan Mira 3" electron microscope (Tescan, Czech Republic). The measure of concentration inhomogeneity is the relative fluctuation of concentration, i.e. the concentration variation coefficient V, being equal to the ratio of the square root of the concentration dispersion to its average value:

$$V = \frac{\sqrt{D}}{C}, \tag{1}$$

where D is the element concentration dispersion, and C is the average concentration [16].

The assumption of the logarithmic normality of the distributions was tested using Pearson's χ^2 test. The entire measurement range of the random variable was divided into disjoint intervals k. In accordance with the given division, the number of sample values that fell within the i-th interval (designated as n_i). The obtained histogram of the sampling distribution serves as the basis for selecting the distribution law [20]. The value characterizing the deviation of the sample distribution from the predicted one is determined by the following formula:

$$\chi^2 = \frac{(n_i - np_i)^2}{np_i}, \tag{2}$$

Table 2. **Billet aging modes**

Таблица 2. **Режимы старения заготовок**

Stage No.	Aging temperature, °C	Holding time, min
1	670	30
2	640	40
3	600	40
4	575	40
5	555	30
6	535	30
7	525	30
8	500	30
9	480	30

where n is the sample volume; n_i is the number of sample elements, falling within the i-th interval; p_i is the probability that the random variable under study falls into the i-th interval, calculated in accordance with the hypothetical distribution law $F(x)$.

In order to predict the concentration inhomogeneity, the following homogenization equation was used:

$$V_j = \alpha_j \exp\left(\beta_j t c_j^{2/3} \exp\left[-\frac{Q_j}{RT}\right]\right), \qquad (3)$$

where V_j and c_j are the variation coefficient and the average concentration of the j-th matrix component; t (h) and T (K) are the sintering time and temperature, respectively; R is the gas constant, J/(mol·K); Q_j is the effective activation energy of mutual diffusion in the system, J/(mol·K); α_j and β_j are the coefficients [16].

Research result and disussion

The structure of the alloys after quenching represented an α-solid solution of Cr, Co, Mo, and Si. Samarium was in the form of individual inclusions (Fig. 1) with very low solubility in the α-phase. The presence of dark areas in Fig. 1 testifies to the residual porosity of the material.

The first stage was to obtain the values of the concentration inhomogeneity for Cr, Co, Mo, Sm. The concentration inhomogeneity decreased with an increase in the sintering temperature and holding time (Table 3).

To determine the law of distribution of concentrations, Pearson's χ^2 criterion was calculated after each of 12 sintering modes. No distributions corresponding to the normal law were identified for chromium. 7 distributions out of 12 distributions corresponded to the logarithmically normal law. A similar pattern was observed when calculating χ^2 for cobalt and molybdenum. Samarium is unevenly distributed in the structure, so it is impossible to establish the law of its distribution within the specified scope of the experiment.

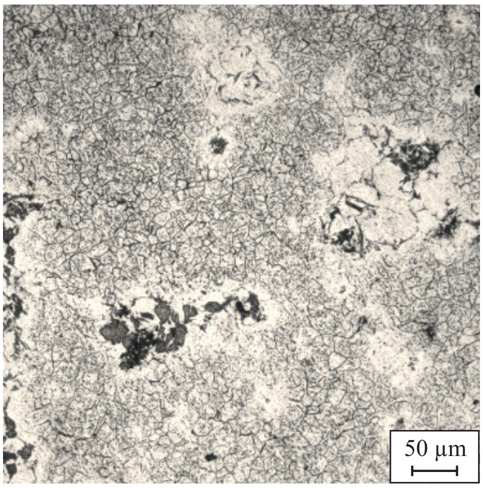

Fig. 1. The microstructure of 22Kh15K4MS alloy alloyed with 0.5 wt. % of Sm after the quenching

Рис. 1. Микроструктура сплава 22Х15К4МС, легированного 0,5 мас. % Sm, после закалки

Upon the construction of element distribution histograms, the entire range of data was divided into 8 intervals (Fig. 2). The distribution histograms of chromium, cobalt, and molybdenum exhibited a right-hand asymmetry, which increased with rising temperature and sintering time.

The approximation of experimental data (Table 3, numerator) allowed to determine α_j, β_j coefficients of the homogenization equation, activation energy Q (Table 4),

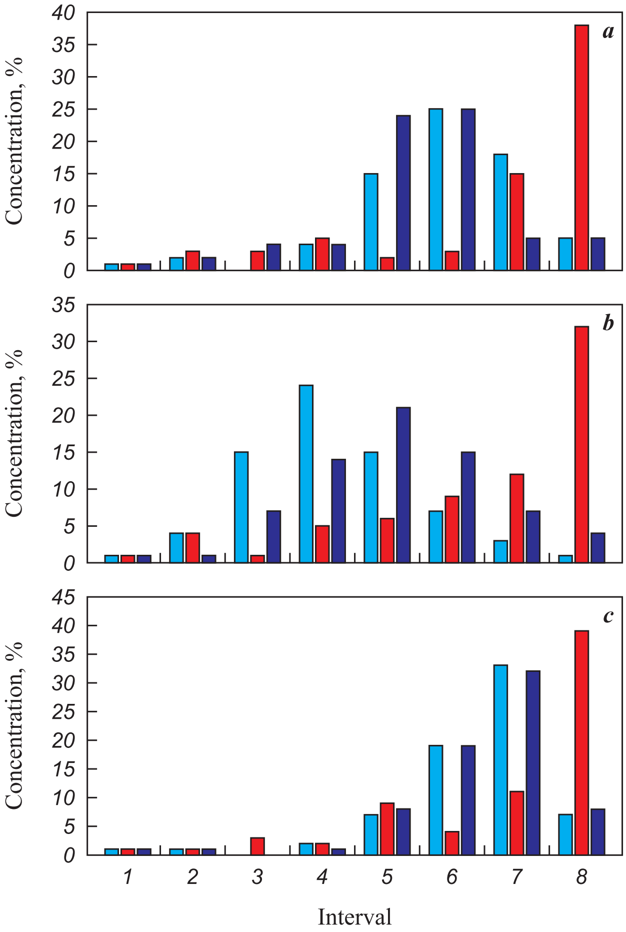

Fig. 2. Distribution histograms of cobalt concentrations (***a***), molybdenum (***b***) and chromium (***c***) after sintering at a temperature of 1250 °C, 3 h
🟦 – observed distribution, 🟥 – expected normal distribution,
■ – expected log-normal distribution

Рис. 2. Гистограммы распределения концентраций кобальта (***a***), молибдена (***b***) и хрома (***c***) после спекания при температуре 1250 °С в течение 3 ч
🟦 – наблюдаемое распределение, 🟥 – ожидаемое распределение по нормальному закону, ■ – ожидаемое распределение по логарифмически нормальному закону

Table 3. **Experimental (numerator) and predicted (denominator) concentration variation coefficients**

Таблица 3. **Экспериментальные (числитель) и прогнозируемые (знаменатель) коэффициенты вариации концентрации**

Sintering mode	Sintering temperature, °C	Holding time during sintering, ч	*V*			
			Cr	Co	Mo	Sm
1	1250	1	0.16 0.15	0.30 0.20	0.52 0.37	0.87 –
2		3	0.14 0.15	0.14 0.18	0.29 0.29	1.07 –
3		8	0.12 0.14	0.13 0.13	0.21 0.23	0.88 –
4	1300	1	0.20 0.15	0.19 0.19	0.34 0.31	0.70 –
5		3	0.17 0.15	0.18 0.17	0.25 0.29	1.08 –
6		8	0.09 0.13	0.11 0.12	0.29 0.22	1.03 –
7	1350	1	0.11 0.13	0.10 0.90	0.33 0.31	1.23 –
8		3	0.15 0.15	0.20 0.14	0.30 0.27	1.19 –
9		8	0.10 0.11	0.90 0.70	0.20 0.20	1.15 –
10	1380	1	0.15 0.14	0.16 0.17	0.34 0.31	0.91 –
11		3	0.11 0.15	0.10 0.12	0.18 0.27	0.70 –
12		8	0.09 0.10	0.06 0.07	0.16 0.19	1.66 –

as well as the predicted values *V* (Table 3, denominator). Due to the uneven distribution of samarium in the structure and high values of concentration inhomogeneity, the prediction of V_{Sm} was not performed.

The dependence of V_e ratio (the experimental coefficient of variation) to V_p ratio (predicted) on the sintering mode was plotted (Fig. 3). The closest V_e and V_p ratios were obtained upon modes *4*, *6*, *8*, *9*, *10*, which correspond to sintering at temperatures of 1300 °C (1 and 8 h), 1350 °C (3 and 8 h), and 1380 °C (1 h).

Q_{Cr} values correspond to the activation energy of chromium in the α-Fe phase of the cast alloy obtained in work [21]. The activation energy amounted to 197 ± 10 kJ/(mol·K) for the alloy with 25.8 wt. % of Cr, which is likely associated with the formation of low-soluble compounds during the heating. Q_{Co} value appeared to be higher than the one specified in the literary sources [22].

An increase in sintering temperature and sintering time resulted in an increase in homogeneity and a decrease in *V* coefficient. Activation energy Q_{Mo} appeared to be at the level of activation energy in binary alloys of iron with

Table 4. **Activation energies and equation coefficients**

Таблица 4. **Энергии активации и коэффициенты уравнений**

Element	*Q*, kJ/(mol·K)	α	β
Cr	209.2	0.157	0.252
Co	288.0	0.207	5.134
Mo	282.0	0.340	1.190
Sm	40.3	0.940	0.003

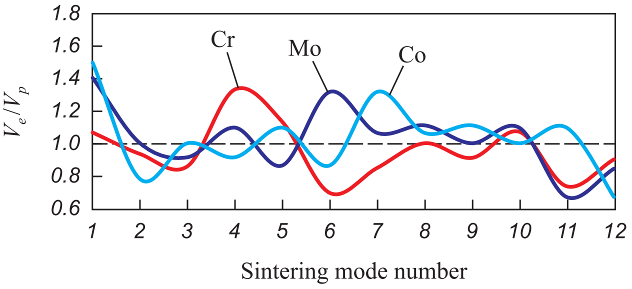

Fig. 3. The dependence of V_e ratio (experimental) to V_p ratio (predicted) on the sintering mode

Рис. 3. Зависимость отношения $V_э$ (эксперимент) к $V_п$ (прогноз) от режима спекания

Mo [20], which is associated with a high ratio of surfaces and the formation of low-soluble compounds during the heating. In Fe–6%Mo alloy, the activation energy is at the level of 262.5 J/(mol·K), and in powder alloy Q_{Mo} it accounts for 282 J/(mol·K) (Table 4).

Sintering at 1250 °C allows to obtain V at the level of 0.16–0.12 for Cr, 0.3–0.1 for Co, at the level of 0.5–0.2 for Mo, and at the level of 0.9–1.1 for Sm, depending on the sintering time. It is noted that the resulting concentration inhomogeneity is directly proportional to the atomic mass of the element. An increase in the sintering temperature up to 1300 °C results in V decrease only after 8 h of holding: 0.09 for Cr and 0.11 for Co, the inhomogeneity values remain the same for Mo. The lowest values of concentration inhomogeneity were obtained after sintering at 1380 °C for 8 h: 0.09 for Cr, 0.06 for Co, and 0.16 for Mo. A further increase in the sintering temperature requires more energy and may result in intense evaporation of chromium from the surface of the billets, which, in turn, will lead to inhomogeneity of the chemical composition between the surface layer and the volume of the sample and a decrease in magnetic properties [5; 23]. Thus, for powder magnets made of 22Kh15K4MS alloy, alloyed with Sm, the optimal sintering mode is the one at a temperature of 1350 °C for 1–3 h. The concentration inhomogeneity of Cr, Co, and Mo, depending on the holding time, varies within 0.01–0.06 (Table 3). The application of quenching after sintering allows to reduce the concentration inhomogeneity of chromium and cobalt to the level of $V = 0.06 \div 0.08$ [24].

The magnetic properties of the samples after sintering for 8 h, quenching, and multistage aging (see Table 2) at various sintering temperatures (Fig. 4) were determined. Upon an increase in sintering temperature from 1250 to 1380 °C, an increase in the level of magnetic properties by 18–20 % was observed, which is associated with a decrease in the concentration inhomogeneity of the alloy (Table 3). The optimum magnetic properties were also obtained after sintering at 1350 °C.

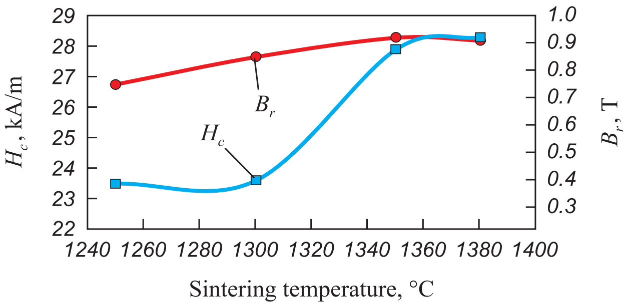

Fig. 4. The dependence of coercive force (H_c) and magnetic induction (B_r) on the sintering temperature

Рис. 4. Зависимость коэрцитивной силы (H_c) и магнитной индукции (B_r) от температуры спекания

For testing the homogenization model as per equation (3), the sintering time for each mode and element was calculated. Table 5 shows the calculated sintering time for the element with the longest homogenization time at a given temperature. According to the results obtained, the level of concentration inhomogeneity is achieved in a shorter time at temperatures of 1250 and 1300 °C (1, 3 and 8 h), 1350 °C (1–3 h), 1380 °C (1 h). At sintering temperatures of 1350 °C, 1380 °C and holding time of 3–8 h, the calculated sintering time significantly exceeds the actual time. This is associated with the fact that the activation energy may not match the value used in the calculation. The used effective activation energy is applicable precisely for this process at the boundary of the existing model.

Table 5. **Calculated sintering times**

Таблица 5. **Расчетные значения времени спекания**

Sintering temperature, °C	Element with the longest homogenization time	V	Holding time during sintering, h	
			Actual	Calculated
1250	Co	0.30	1	0.82
	Mo	0.29	3	1.10
	Mo	0.21	8	3.20
1300	Mo	0.34	1	0.61
	Mo	0.25	3	2.10
	Mo	0.29	8	2.90
1350	Mo	0.33	1	0.61
	Mo	0.30	3	0.83
	Cr	0.10	8	11.80
1380	Mo	0.34	1	0.61
	Co	0.10	3	6.90
	Co	0.06	8	13.50

To assess the effect of samarium addition on the magnetic properties of 22Kh15K4MS alloy, the multistage aging of samples without samarium as well as samples with 0.5 wt. % of Sm was performed. The fastest growth of the magnetic properties (B_r and H_c) of the alloy with 0.5 wt. % of Sm occurred at the first three stages of aging. In subsequent stages, only H_c growth continued. Upon that, the magnetic induction B_r reached its peak at the 4th stage of aging with further permanent decrease (Table 6).

The rectangularity coefficient of magnetic hysteresis loop (C_r) had the highest value after the 3rd stage of aging (Table 6). Compared to the initial alloy, C_r is 9–11 % higher for the alloyed alloy under this heat treatment mode. According to the *X*-ray diffraction analysis performed in work [25], the diffraction peaks corresponding to Sm_2Co_{17} (64.9°, 74.68°) and $SmCo_5$ (50.798°) phases were identified in the samples after aging, except for the α-phase. This, in turn, testifies to the redistribution of samarium during aging and the production of a stoichiometric composition distinct from the initial component.

Conclusions

1. The distributions of chromium, cobalt, and molybdenum correspond to the asymptotically logarithmically normal law. Samarium is unevenly distributed in the structure, therefore, it is impossible to establish the law of its distribution within the specified scope of the experiment. The homogenization process did not effect the homogeneity of samarium distribution, which is apparently associated with the non-solubility of Sm in iron.

2. A complete statistical description of the distribution of Cr, Co, Mo of 22Kh15K4MS ridge alloy with the addition of samarium in the amount of 0.5 wt. % is presented. Based on the experimental determination of *V* criterion, a homogenization equation, which allows to numerically evaluate the effect of sintering modes on the concentration inhomogeneity, was obtained.

Table 6. **Magnetic properties of the 22Kh15K4MS alloy with a additive of samarium after aging**

Таблица 6. **Магнитные свойства сплава 22Х15К4МС с добавкой самария после старения**

Aging temperature, °C:	22Х15К4МС		22Х15К4МС + + 0,5 % Sm	
	H_c, kA/m	B_r, T	H_c, kA/m	B_r, T
670	2.7	0.40	3.9	0.44
640	5.1	0.77	6.5	0.82
600	8.5	0.97	10.7	0.93
575	16.8	0.99	19.5	0.95
555	24.7	0.99	26.4	0.92
535	28.4	0.98	29.7	0.90
525	28.4	0.93	29.4	0.86
500	31.3	0.92	32.9	0.86
480	32.1	0.92	33.0	0.85
BH_{max}, kJ/m^3	12		11	
C_r, at 600 °C	0.66		0.73	

3. The optimal sintering mode for powder magnets made of samarium-alloyed 22Kh15K4MS alloy was experimentally selected.

4. The alloying of 22Kh15K4MS alloy with samarium in an amount of 0.5 wt. % makes it possible to obtain powder hysteresis magnets with a coercive force of 3.9–33.0 kA/m and a residual magnetic induction of 0.44–0.95 T at C_r up to 0.73, which constitutes an actual index for precision tool-making.

References / Список литературы

1. Antsiferov V.N., Beklemyshev A.M., Gilev V.G., Porozova S.E., Shveikin G.P. Problems of powder materials science. Part 2: Highly porous permeable materials. Ekaterinburg: Ural Branch of the Russian Academy of Sciences, 2002. 261 p. (In Russ.).

   Анциферов В.Н., Беклемышев А.М., Гилев В.Г., Порозова С.Е., Швейкин Г.П. Проблемы порошкового материаловедения. Часть 2: Высокопористые проницаемые материалы. Екатеринбург: УрО РАН, 2002. 261 с.
2. Yamashita M., Fujimura S. Sintered Fe–Cr–Co type magnetic alloy and method for producing article made thereof: Pat. 4601876 (USA). 1986.
3. Ternero F., Rosa L.G., Urban P., Montes J.M., Cuevas F.G. Influence of the total porosity on the properties of sintered materials – A review. *Metals*. 2021;11(5):730. https://doi.org/10.3390/met11050730
4. Bocchini G.F. The influences of porosity on the characteristics of sintered materials. *International Journal of Powder Metallurgy* (Princeton, New Jersey). 1986;07: 185–186, 188. https://doi.org/10.4271/860148
5. Ustyuhin A.S., Alymov M.I., Milyaev I.M. Magnetic hysteresis properties of Fe–26Cr–16Co hard magnetic alloys. *Letters on Materials*. 2014;4(1):59–61. (In Russ.). https://doi.org/10.22226/2410-3535-2014-1-59-61

   Устюхин А.С., Алымов М.И., Миляев И.М. Магнитные гистерезисные свойства Fe–26Cr–16Co порошковых магнитотвердых сплавов. *Письма о материалах*. 2014;4(1):59–61. https://doi.org/10.22226/2410-3535-2014-1-59-61
6. Zhang B. Calculation of self-diffusion coefficients in iron. *AIP Advances*. 2014;4(1):017128. https://doi.org/10.1063/1.4863462
7. Xiao Y.Z., Ji-Hua Z., Yuan W., Xu-Sheng Y., Turab L., Hong-Hui W. Machine learning assisted design of FeCoNiCrMn high-entropy alloys with ultra-low hydrogen diffusion coefficients. *Acta Materialia*. 2022; 224:117535. https://doi.org/10.1016/j.actamat.2021.117535
8. Serin B., Ellickson R.T. Determination of diffusion coefficients. *Journal of Chemical Physics*. 1941;(9):742–747.
9. Balogh J., Kemény T., Vincze I., Bujdosó L., Tóth L., Vincze G. Amorphous alloy formation by mechanical

alloying and consecutive heat treatment in $Fe_{50}B_{50}$ powder mixture. *Journal of Applied Physics*. 1995;77(10): 4997–5003. https://doi.org/10.1063/1.359522

10. Ivasishin O.M., Eylon D., Bondarchuk V.I., Savvakin D.G. Diffusion during powder metallurgy synthesis of titanium alloys. *Defect and Diffusion Forum*. 2008;277:177–185. https://doi.org/10.4028/www.scientific.net/DDF.277.177
11. Dash A., Paul A. Body diagonal diffusion couple method for estimation of tracer diffusion coefficients in a multi-principal element alloy. https://doi.org/10.48550/arXiv.2205.06550 (accessed: 25.11.2022).
12. Purdy G.R., Kirkaldy J.S. Homogenization by diffusion. *Metallurgical Transactions*. 1971;2(2):371–378. https://doi.org/10.1007/BF02663324
13. Antsiferov V.N., Peshcherenko S.N., Kurilov P.G. Mutual diffusion and homogenization in powder materials. Moscow: Metallurgiya, 1988. 152 p. (In Russ.).

    Анциферов В.Н., Пещеренко С.Н., Курилов П.Г. Взаимная диффузия и гомогенизация в порошковых материалах. М.: Металлургия, 1988. 152 с.
14. Bulanov V.Ya., Krashaninin V.A., Oglezneva S.A. Modeling of homogenization of binary powder alloys. *Konstruktsii iz kompozitsionnykh materialov*. 2006;(4): 181–187. (In Russ.).

    Буланов В.Я., Крашанинин В.А., Оглезнева С.А. Моделирование гомогенизации бинарных порошковых сплавов. *Конструкции из композиционных материалов*. 2006;(4):181–187.
15. Engquist B., Souganidis P.E. Asymptotic and numerical homogenization. *Acta Numerica*. 2008;(17):147–190. https://doi.org/10.1017/S0962492906360011
16. Ryaposov I.V., Kleiner L.M., Shatsov A.A. Concentration-precision non-uniform soft-magnetic alloys based on the system Fe–Si–Al. *Vestnik Permskogo natsional’nogo issledovatel’skogo politekhnicheskogo universiteta. Mashinostroenie, materialovedenie*. 2011;13(3):92–102. (In Russ.).

    Ряпосов И.В., Клейнер Л.М., Шацов А.А. Концентрационно-неоднородные прецизионные магнитно-мягкие сплавы на основе системы Fe–Si–Al. *Вестник Пермского национального исследовательского политехнического университета. Машиностроение, материаловедение*. 2011;13(3):92–102.
17. Ormerod J. Powder metallurgy of rare earth permanent magnets. *The International Journal of Powder Metallurgy*. 1989;25(3):197–205.
18. Tao S., Ahmad Z., Zhang P., Zheng X., Zhang S. Effects of Sm on structural, textural and magnetic properties of Fe–28Cr–20Co–3Mo–2V–2Ti hard magnetic alloy. *Journal of Alloys and Compounds*. 2020;816:152619. https://doi.org/10.1016/j.jallcom.2019.152619
19. Ustyukhin A., Alymov M., Ashmarin A., Milyaev I., Zelenskii V., Ankudinov A. The phase composition of powder hard magnetic Fe-30Cr-(8-24)Co alloys sintered under different temperature conditions. *Doklady Akademii Nauk*. 2018;482(2):172–176. (In Russ.). https://doi.org/10.31857/S086956520003475-5

    Устюхин А.С., Алымов М.И., Ашмарин А.А., Миляев И.М., Зеленский В.А. Анкудинов А.Б. Исследование фазового состава порошковых магнитотвердых сплавов Fe–30Cr–(8–24)Co, спеченных при различных температурных режимах. *Доклады Академии наук*. 2018;483(2):172–176. https://doi.org/10.31857/S086956520003475-5
20. Akhnazarova S.L., Kafarov V.V. Methods of organization of experiment in chemical technology. Moscow: Vysshaya shkola, 1978. 319 p. (In Russ.).

    Ахназарова С.Л., Кафаров В.В. Оптимизация эксперимента в химии и химической технологии. М.: Высшая школа, 1978. 319 с.
21. Blanter M.E. Theory of heat treatment Moscow: Metallurgiya, 1984. 328 p. (In Russ.).

    Блантер М.Е. Теория термической обработки. Учебник для вузов. М.: Металлургия, 1984. 328 с.
22. Pavlinov L.V. Diffusion in binary and multicomponent alloys based on iron in the region of α- and γ-solid solutions. Obninsk: Fiziko-energeticheskii institut, 1976. 38 p. (In Russ.).

    Павлинов Л.В. Диффузия в двойных и многокомпонентных сплавах на основе железа в области α- и γ-твердых растворов. Обнинск: Физико-энергетический институт, 1976. 38 с.
23. Ustyukhin A.S., Ankudinov A.B., Zelenskii V.A., Milyaev I.M., Alymov M.I. Improvement of magnetic properties by hot rolling of sintered powder alloy in the Fe–Cr–Co system. *Doklady Physical Chemistry*. 2017;476(2):193–196. https://doi.org/10.1134/S0012501617100074

    Устюхин А.С., Анкудинов А.Б., Зеленский В.А. Миляев И.М., Алымов М.И. Эффект повышения магнитных свойств при горячей прокатке спеченного порошкового сплава системы Fe–Cr–Co. *Доклады Академии наук*. 2017;476(6):656–659. https://doi.org/10.7868/S0869565217300120
24. Marieva M.A., Shatsov A.A. Control of hysteretic properties in powder alloys based on the Fe–Cr–Co system. *Powder Metallurgy and Functional Coatings*. 2021; 15(3):14–21. (In Russ.). https://doi.org/10.17073/1997-308X-2021-3-14-21

    Мариева М.А., Шацов А.А. Управление гистерезисными свойствами в порошковых сплавах на основе системы Fe–Cr–Co. *Известия вузов. Порошковая металлургия и функциональные покрытия*. 2021;15(3):14–21. https://doi.org/10.17073/1997-308X-2021-3-14-21
25. Marieva M.A., Kozvonin V.A., Shatsov A.A. Increasing the rectangularity of the loop of magnetic hysteresis of magnetic hysteresis based on the Fe–Cr–Co system due to the alloying Sm. *Bulletin PNRPU. Mechanical engineering, materials science*. 2021;23(3):39–46. (In Russ.).

    Мариева М.А., Козвонин В.А., Шацов А.А. Повышение прямоугольности петли магнитного гистерезиса магнитотвердого сплава на основе системы Fe–Cr–Co за счет легирования Sm. *Вестник Пермского национального исследовательского политехнического университета. Машиностроение, материаловедение*. 2021;23(3):39–46.

Information about the Authors

Marya A. Marieva – Postgraduate Student of the Department of metal science, thermal and laser processing of metals, Perm National Research Polytechnic University
ORCID: 0000-0002-6599-5091
E-mail: marievamar@rambler.ru

Alexandr A. Shatsov – Dr. Sci. (Eng.), Prof. of the Department of metal science, thermal and laser processing of metals, Perm National Research Polytechnic University
ORCID: 0000-0002-2723-964X
E-mail: shatsov@pstu.ru

Сведения об авторах

Мария Александровна Мариева – аспирант кафедры «Металловедение, термическая и лазерная обработка металлов», Пермский национальный исследовательский политехнический университет
ORCID: 0000-0002-6599-5091
E-mail: marievamar@rambler.ru

Александр Аронович Шацов – д.т.н., профессор кафедры «Металловедение, термическая и лазерная обработка металлов», Пермский национальный исследовательский политехнический университет
ORCID: 0000-0002-2723-964X
E-mail: shatsov@pstu.ru

Contribution of the Authors

M. A. Marieva – conducting of calculations, experiments and testing of samples; processing and analysis of research results; writing the text of the article.
A. A. Shatsov – scientific of guidance, formation of the basic concept, statement of research goal and objectives, resources provision, preparation of the experiments, correction the text of the article and conclusions.

Вклад авторов

М. А. Мариева – проведение расчетов, экспериментов и испытаний образцов; обработка и анализ результатов исследования; написание текста статьи.
А. А. Шацов – научное руководство, формирование основной концепции, постановка цели и задачи исследования, обеспечение ресурсами, подготовка экспериментов, корректировка текста статьи и выводов.

Received 07.07.2022
Revised 27.07.2022
Accepted 01.08.2022

Статья поступила 07.07.2022 г.
Доработана 27.07.2022 г.
Принята к публикации 01.08.2022 г.

Self-Propagating High-Temperature Synthesis
Самораспространяющийся высокотемпературный синтез

UDC 536.74, 621.762.2

https://doi.org/10.17073/1997-308X-2023-1-21-27

Research article
Научная статья

Fabrication of (Ti–Al–Si)/(Ti–C)/Ti – layered alloy by SHS pressing

P. A. Lazarev, M. L. Busurina, A. N. Gryadunov,
A. E. Sytschev, A. F. Belikova

Merzhanov Institute of Structural Macrokinetics and Materials Science of the Russian Academy of Sciences
8 Akademican Osip'yan Str., Chernogolovka, Moscow region 142432, Russian Federation

Lazarev@ism.ac.ru

Abstract. A metal–carbide–intermetallic material based on combustion products of the layer system (Ti–Al–Si)/(Ti–C)/Ti was for the first time obtained with the help of self-propagating high-temperature synthesis (SHS) combined with pressing. Exothermic synthesis from elementary powders was carried out at a pressure of 10 MPa, and pressing of the hot synthesis product was carried out at a pressure of 100 MPa. It has been shown that SHS pressing contributes to the formation of permanent joints of «metal/carbide/intermetallic» layers. The main features of microstructure formation, phase composition, and strength properties of transition zones at the boundary between reacting SHS compositions, Ti–C and Ti–Al–Si and Ti-metal substrate are investigated. It is shown that during SHS reaction, a homogeneous microstructure of Ti–C and Ti–Al–Si layers with an insignificant content of cracks and pores is formed. The thickness of the transition zone between the layers was at least 15 μm. The main phase formed in the combustion product of Ti–Al–Si layer is, according to the results of *X*-ray phase analysis, triple phase $Ti_{20}Al_3Si_9$, the content of which, calculated by the Rietveld method, was at least 87 wt. %. In addition, the combustion product contains a secondary phase of Ti_3Al in the amount of 13 wt. %. The energy dispersion analysis revealed that diffusion of aluminium through the titanium carbide layer into the titanium substrate to a depth of approx. 30 μm is observed. Microhardness value of the combustion product of Ti–Al–Si layer was about 10 GPa. The rectilinear nature of crack propagation in the synthesized combustion product of Ti–Al–Si layer, as well as the Palmquist crack resistance coefficient varying within 5.1–5.7 $MPa{\cdot}m^{1/2}$, indicate the fragility of the material.

Keywords: layered material, intermetallic compound, SHS-pressing, Ti–Al–Si

For citation: Lazarev P.A., Busurina M.L., Gryadunov A.N., Sytschev A.E., Belikova A.F. Fabrication of (Ti–Al–Si)/(Ti–C)/Ti – layered alloy by SHS pressing. *Powder Metallurgy and Functional Coatings*. 2023;17(1):21–27. https://doi.org/10.17073/1997-308X-2023-1-21-27

Получение слоевого (Ti–Al–Si)/(Ti–C)/Ti сплава методом СВС-прессования

П. А. Лазарев, М. Л. Бусурина, А. Н. Грядунов,
А. Е. Сычев, А. Ф. Беликова

Институт структурной макрокинетики и проблем материаловедения им. А.Г. Мержанова РАН
Россия, 142432, Московская обл., г. Черноголовка, ул. Академика Осипьяна, 8

Lazarev@ism.ac.ru

Аннотация. Методом самораспространяющегося высокотемпературного синтеза (СВС), совмещенного с прессованием, впервые получен металло-карбидно-интерметаллидный материал на основе продуктов горения слоевой системы

(Ti–Al–Si)/(Ti–C)/Ti. Экзотермический синтез из элементарных порошков осуществляли при давлении 10 МПа, а прессование горячего продукта синтеза – при давлении 100 МПа. В работе продемонстрировано, что в результате СВС-прессования формируется неразъемное соединение слоев «метал/карбид/интерметаллид». Исследованы основные особенности формирования микроструктуры, фазовый состав и прочностные свойства переходных зон на границе между реагирующими СВС-составами Ti–C и Ti–Al–Si и Ti-металлической подложкой. Показано, что в процессе СВС-реакции формируется однородная микроструктура слоев Ti–C и Ti–Al–Si с незначительным содержанием трещин и пор. Толщина переходной зоны между слоями составила не менее 15 мкм. Основной фазой, формирующейся в продукте горения слоя на основе Ti–Al–Si, является, по результатам рентгенофазового анализа, тройная фаза $Ti_{20}Al_3Si_9$, содержание которой, посчитанное по методу Ритвельда, составило не менее 87 мас.%. Кроме того, в продукте горения присутствует вторичная фаза Ti_3Al в количестве 13 мас.%. Результаты энергодисперсионного анализа показали, что наблюдается диффузия алюминия сквозь слой карбида титана в титановую подложку на глубину ~30 мкм. Значение микротвердости продукта горения слоя на основе Ti–Al–Si составило около 10 ГПа. Прямолинейный характер распространения трещин в синтезированном продукте горения слоя Ti–Al–Si, а также варьирующийся в пределах 5,1–5,7 МПа·м$^{1/2}$ коэффициент трещиностойкости по Палмквисту говорят о хрупкости материала.

Ключевые слова: слоевой материал, интерметаллид, СВС-прессование, Ti–Al–Si

Для цитирования: Лазарев П.А., Бусурина М.Л., Грядунов А.Н., Сычев А.Е., Беликова А.Ф. Получение слоевого (Ti–Al–Si)/(Ti–C)/Ti сплава методом СВС-прессования. *Известия вузов. Порошковая металлургия и функциональные покрытия*. 2023;17(1):21–27. https://doi.org/10.17073/1997-308X-2023-1-21-27

Introduction

Obtaining layered systems and permanent joints of various metal-intermetallic materials constitutes a significant task for modern industry, particularly for aerospace applications, taking into account the unique combination of physical and mechanical characteristics of metal-intermetallic layered composites [1]. Material microstructure development, oriented towards a specific set of structural and functional characteristics, represents an urgent task in materials science. Ti–Al titanium aluminides can be distinguished among a variety of intermetallic compounds, which need to increase their temperature resistance to oxidation and deformation [2–4]. Titanium-based alloys with other light elements (Mg, Si etc.) appear to be highly promising for high-temperature applications in a variety of industries, particularly for use as protective coatings. Silicon appears to be a compelling choice for a reinforcing component (Ti_5Si_3) in a TiAl-based composite and also positively affects the resistance of titanium and its alloys to high-temperature oxidation [5; 6].

Since the well-known methods for producing the required materials (hot isostatic pressing [7] and spark plasma sintering [8]) are costly and technically demanding, it is essential to find new, technologically simplified methods for their production. Self-propagating high-temperature synthesis (SHS) may be a promising way of solving the problem of obtaining metal-intermetallic layered materials [9]. During the SHS process, a large amount of heat released can be used not only for further processing of the material or formation of its structure, but also as a source of additional heat for joining (welding, repairing) heterogeneous materials and applying coatings [10; 11]. For instance, Ti–Al–Si alloys were produced by SHS in work [12] upon the interaction of titanium, silicon, and AlSi30 alloy followed by the addition of alloying elements. A method for the production of Ti–Al–Si alloys with an aluminum content ranging from 8 to 20 %[1] and a silicon content of 10–20 % has been elaborated in works [13–15]. Combining the SHS method and pressing may be used to produce layered and graded carbide-hardened materials, as well as permanent joints of heterogeneous materials and protective coatings. The SHS-pressing method was used to obtain NiAl–Ni layer compositions [16] and multilayer systems “hard alloy–intermetallic–metal” [17].

In this paper, the features of the formation of microstructure and strength properties of transition zones at the boundary between reacting SHS compounds and Ti-substrate in a layer system (Ti–Al–Si)/(Ti–C)/Ti have been investigated.

Experimental procedures

The following metal powders were used in the experiment: Si (semiconductor silicon, solar-grade, ~100 μm, at least 99 %), Ti (PTM, <100 μm, 99.2 %), and Al (ASD-4, ~10 μm, 99.20 %) to obtain a powder reaction mixture of 74.1Ti–6.3Al–19.6Si (%); incendiary mixture Ti/C (black) (50/50 %); titanium foil (Ti) of 200 μm thick. The mass ratio of layers 1-layer/2-layer/Ti-substrate was approximately ~90/8/2 %. Composition of the reaction mixture based on Ti–Al–Si was chosen to obtain the phase $Ti_{20}Al_3Si_9$. The initial powder blank of the 1st layer was obtained by dry mixing in a mortar, followed by pressing of cylindrical samples 30 mm in diameter and 16 mm in height with a relative density of 0.6. The compressed samples were placed in a reaction compression mold (Fig. 1), pre-mounted on a Ti substrate.

---

[1] Here in after – wt. %.

To obtain a nonporous material, SHS pressing technique described in [18; 19] has been used, while exothermic synthesis was carried out at a pressure of 10 MPa, and pressing of the synthesis product was carried out at a pressure of 100 MPa. The exposure time under load was 3 s.

The microstructure of the synthesized alloy was studied using an "Zeiss Ultra plus 55" field emission scanning electron microscope. *X*-ray phase analysis (XRD) was performed on a DRON-3 diffractometer using CuK_α radiation. Microhardness (H_μ) was measured on a PMT-3 hardness tester using the Vickers method (indentation of a tetrahedral diamond pyramid with a load of 100 g). Crack formation was studied by the method of indentation by the Vickers diamond pyramid *HV* at a higher load of up to 30 kg.

Results and discussion

Preliminary thermodynamic calculations performed in the software "Thermo"[2] clearly revealed that the largest thermal effect is observed in the layer based on the Ti–C system for which the adiabatic combustion temperature was 2617 °C and the enthalpy of formation was 176 kJ/mol. During the combustion of Ti–C reaction composition, the melting of the surface layer of the titanium substrate ($t_{\mathrm{Ti}}^{\mathrm{melt}}$ = 1670 °C) and the formation of the Ti/TiC transition zone is most likely to occur. Adiabatic combustion temperature of Ti–C is much higher than combustion temperature of Ti–Al–Si layer, equal to 1259 °C [15] which also affects the diffusion interaction and formation of a transition zone between Ti–C and Ti–Al–Si layers and provides a strong interpase connection between the Ti-substrate and the Ti–C carbide layer.

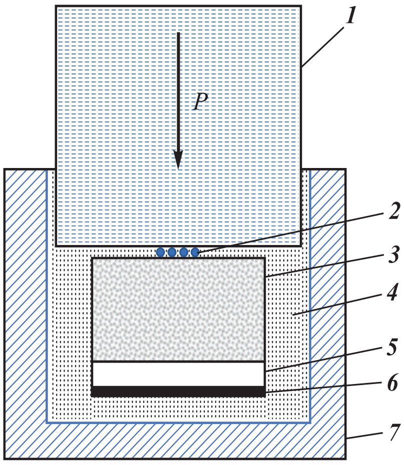

Fig. 1. Scheme of experiments on SHS pressing
1 – upper punch, ***2*** – igniting spiral W,
3 – Ti–Al–Si layer, ***4*** – SiO_2 heat insulator, ***5*** – Ti–C layer,
6 – Ti-substrate, ***7*** – mold

Рис. 1. Схема проведения экспериментов по СВС-прессованию
1 – верхний пуансон, ***2*** – поджигающая спираль W,
3 – слой Ti–Al–Si, ***4*** – теплоизолятор SiO_2, ***5*** – слой Ti–C,
6 – Ti-подложка, ***7*** – пресс-форма

Figure 2 represents the microstructure and element distribution map of Ti, Al, Si and C in the synthesised alloy. A firm contact between the layers with the absence of any defects (pores, cracks) has been formed. This indicates a high quality of diffusion interaction of the elements between the layers.

As shown by XRD (Fig. 3), the 1st layer conforms to an alloy based on the main phase $Ti_{20}Al_3Si_9$ (PDF 01-079-2701) with a hexagonal close-packed (HCP) lattice; furthermore, there is a secondary ordered phase Ti_3Al with a superstructure $D0_{19}$ (PDF 52-859), which exhibits a HCP latitude (spatial group *P*63/*mmc*). The content

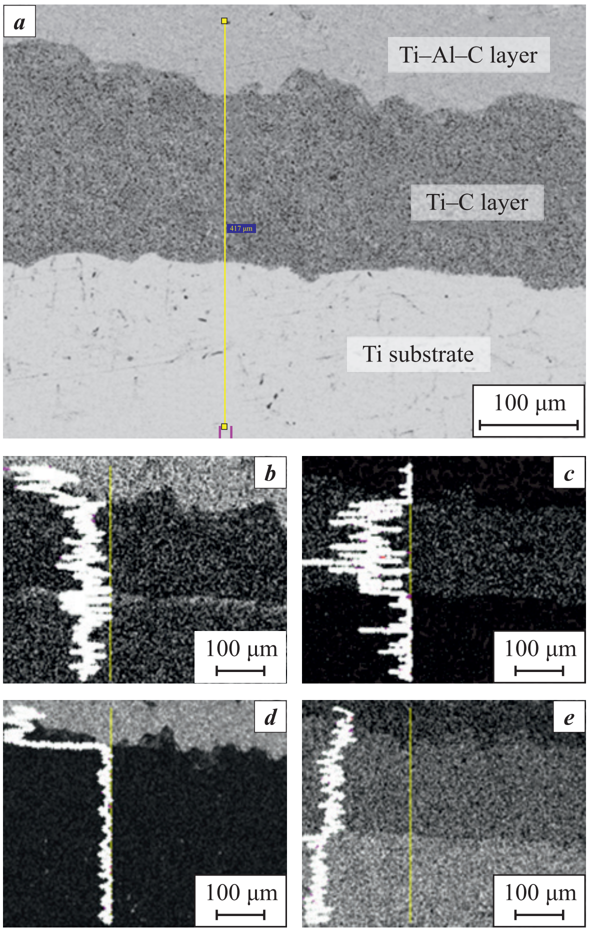

Fig. 2. Photo of the microstructure (***a***) and element distribution map in the synthesised alloy
b – Al, ***c*** – C, ***d*** – Si, ***e*** – Ti

Рис. 2. Фотография микроструктуры (***a***) и карта распределения элементов в синтезированном сплаве
b – Al, ***c*** – C, ***d*** – Si, ***e*** – Ti

---

[2] *Program for thermodynamics equilibrium calculations "THERMO"*. URL: http://www.ism.ac.ru/thermo (accessed: 15.02.2022).

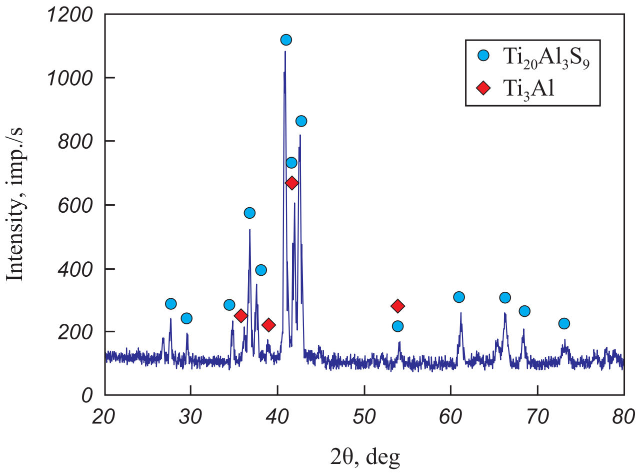

Fig. 3. *X*-ray data of a synthesized alloy based on the Ti–Al–Si system (1st layer)

Рис. 3. Данные РФА синтезированного сплава на основе системы Ti–Al–Si (1-й слой)

of the main phase $Ti_{20}Al_3Si_9$ (calculated by the Rietveld method) was 87 %, the phase Ti_3Al – 13 %. According to the data obtained by energy-dispersive analysis (EDA), the 2nd layer conforms to the phase $TiC_{0.66}$ (cubic structure *Fm*3*m*), and the 3rd layer conforms to titanium in a substrate made of titanium foil. The transition zones between the layers do not exceed 10–15 μm.

According to the concentration profile of the element distribution between the layers (Fig. 4) a slight increase of aluminium concentration in the boundary area between Ti/TiC layers can be observed due to the melting of the titanium foil caused by heat release during reaction in the Ti–C layer and diffusion of aluminium into the titanium substrate through the Ti–C layer. Upon that, the depth of Al diffusion into the Ti substrate is rather shallow ~30 μm. Silicon concentration during transition from the Ti–Al–Si layer to Ti–C drops sharply and remains at zero values in the 2nd and 3rd layers.

Microhardness (H_μ) of each of the layers of the synthesized gradient material is presented in Table. The highest H_μ value (~12.3 GPa) corresponds to a Ti–C-based layer, the lowest is for a titanium substrate (4.1 GPa). Microhardness of Ti–Al–Si layer is ~10.1 GPa.

When an indenter is inserted at a load of more than 30 kg into a Ti–Al–Si-based layer, radial cracks are formed in the corners of the Vickers pyramid imprints in the area of maximum tension stresses (Fig. 5, *a*, *b*). The formation of main concomitant cracks and their

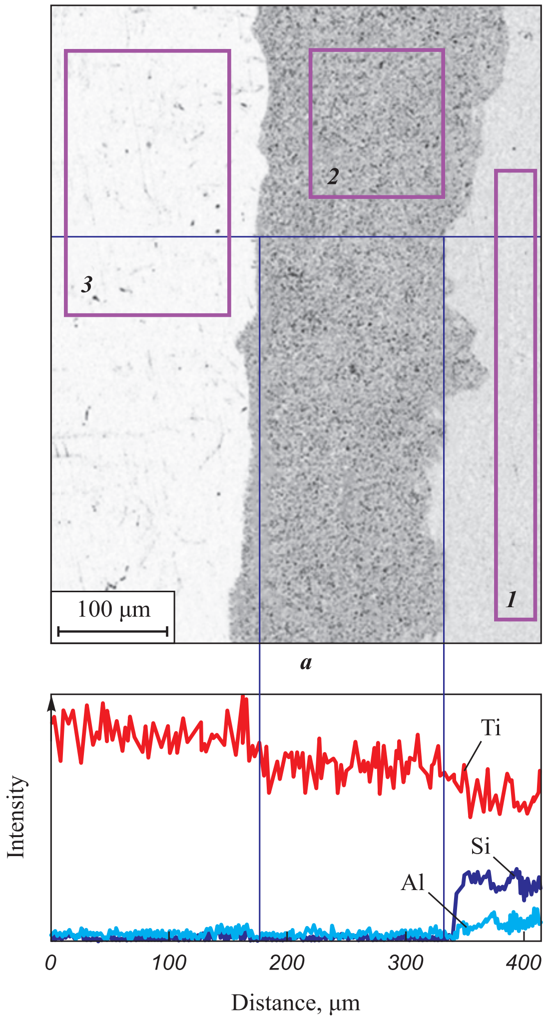

Range	C	Al	Si	Ti	Phase
1	3.92	8.08	26.21	61.78	$Ti_{20}Al_3Si_9$
2	39.23	1.99	0.46	58.32	$TiC_{0.66}$
3	6.16	0.27	0.27	90.60	Ti (substrate)

b

Fig. 4. Concentration profile of element distribution between the layers (***a***) and EDA data, wt. % (***b***)

Рис. 4. Концентрационный профиль распределения элементов между слоями (***a***) и данные ЭДА, мас. % (***b***)

Microhardness values in layers of the synthesized material

Значения микротвердости в слоях синтезированного материала

Layer		Microhardness H_μ, GPa	Cracking resistance coefficient K_{1c}, MPa·m$^{1/2}$
No.	Composition		
1	Ti–Al–Si	10.1	5.1–5.7 (this work)
2	Ti–C	12.3	2.5–4.3 [24]
3	Ti-substrate	4.1	50–55 [25]

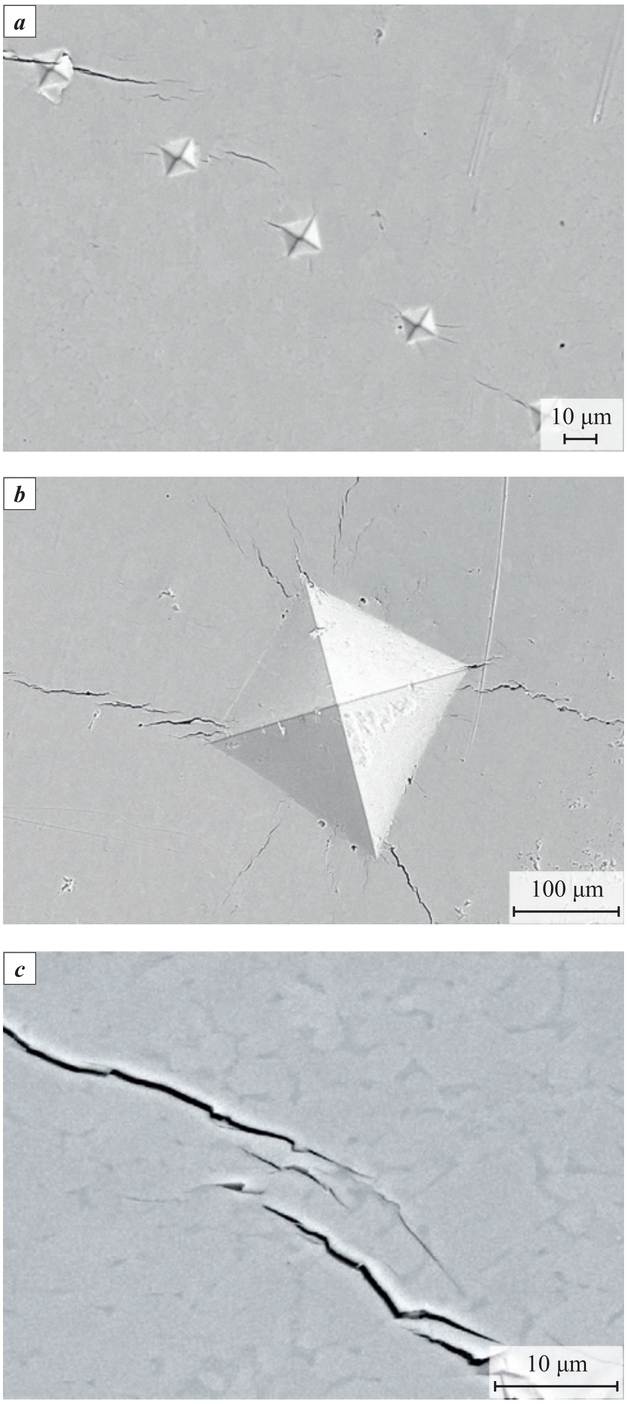

Fig. 5. Micrographics of indentation after measuring microhardness H_{μ} (***a***) and Vickers hardness *HV* (***b***), as well as an enlarged fragment of crack propagation in Ti–Al–Si layer (***c***)

Рис. 5. Микрофотографии отпечатков индентора после измерения микротвердости H_{μ} (***a***) и твердости по Виккерсу *HV* (***b***), а также увеличенный фрагмент распространения трещины в слое на основе Ti–Al–Si (***c***)

branching, as well as the fusion of cracks with micro-heterogeneities and structural defects are observed (Fig. 5, *c*). One of the reasons for this is that the micropores affect the crack propagation process. The rectilinear nature of crack propagation indicates a high fragility of the material. It is noteworthy that the cracks propagate both through and around the grains (Fig. 5, *c*). Calculated by the Palmquist method [20] for a Ti–Al–Si-based layer, the crack resistance coefficient is K_{1c} = 5.1÷5.7 MPa·m$^{1/2}$. The measurements were taken at an indenter load of 100 g using the formula:

$$K_{1c} = 0{,}0028\sqrt{HV}\sqrt{Pc^{-1}},$$

where *P* – indentation load, *c* – total length of the crack from the indenter, mm.

The following results can be given to compare the resulting value of K_{1c}. According to work [21], the crack resistance coefficient of Ti–Al–Si-based alloys can reach values from 0.7 to 1.7 MPa·m$^{1/2}$, while Ti_5Si_3 silicide has K_{1c} = 7 MPa·m$^{1/2}$ [22]. It is noted in work [23] that materials based on Ti–Al_3Ti with a volume fraction of Al_3Ti phase equal to 86, 80, and 65 % are characterized by high crack resistance values at the level of 15, 23, and 29 MPa·m$^{1/2}$, respectively. The measurement results of K_{1c} depend on the size and direction of movement of cracks, pores, interphase transformations, and the magnitude of loads on the material.

Conclusion

A metal-carbide-intermetallic layer material based on (Ti–Al–Si)/(Ti–C)/Ti was synthesized by SHS pressing. The heat released as a result of SHS reactions in the layers and the subsequent pressing of the hot product ensured the required diffusion through the boundaries (Ti–Al–Si)/(Ti–C) and (Ti–C)/Ti and resulted in the formation of a solid permanent joint between the layers with a transition zone thickness between them about 10÷15 μm. Combustion product of Ti–Al–Si layer exhibits two phases: triple phase $Ti_{20}Al_3Si_9$ and Ti_3Al with a content of 87 and 13 wt. %, respectively. The microhardness of the synthesized combustion product of Ti–Al–Si layer was ~10.1 GPa, crack resistance coefficient K_{1c} = 5.1÷5.7 MPa·m$^{1/2}$. The obtained results can be used in the development of methods for applying protective coatings/layers to the surface of titanium products.

References / Список литературы

1. Vecchio K.S. Synthetic multifunctional metallic-intermetallic laminate composites. *JOM*. 2005;57(3):25–31. https://doi.org/10.1007/s11837-005-0229-4
2. Patselov A., Greenberg B., Gladkovskii S., Lavrikov R., Borodin E. Layered metal-intermetallic composites in Ti–Al system: strength under static and dynamic load. *AASRI Procedia*. 2012;3:107–112. https://doi.org/10.1016/j.aasri.2012.11.019

3. Price R.D., Jiang F., Kulin R.M., Vecchio K.S. Effects of ductile phase volume fraction on the mechanical properties of Ti–TiAl$_3$ metal-intermetallic laminate (MIL) composites. *Materials Science and Engineering: A*. 2011; 528(7–8):3134–3146.
https://doi.org/10.1016/j.msea.2010.12.087

4. Lasalmonie A. Intermetallics: Why is it so difficult to introduce them in gas turbine engines? *Intermetallics*. 2006;14(10–11);1123–1129.
https://doi.org/10.1016/j.intermet.2006.01.064

5. Xiong H.-P., Mao W., Xie Y.-H., Cheng Y.-Y., Li X.-H. Formation of silicide coatings on the surface of a TiAl-based alloy and improvement in oxidation resistance. *Materials Science and Engineering A*. 2005;391(1–2):10–18.
https://doi.org/10.1016/j.msea.2004.05.026

6. Teng S., Liang W., Li Z., Ma X.J. Improvement of high-temperature oxidation resistance of TiAl-based alloy by sol-gel method. *Journal of Alloys and Compounds*. 2008;464(1–2): 452–456. https://doi.org/10.1016/j.jallcom.2007.10.017

7. Gao N.F., Miyamoto Y., Zhang D. Dense Ti$_3$SiC$_2$ prepared by reactive HIP. *Journal of Materials Science*. 1999;34(18):4385–4392.
https://doi.org/10.1023/A:1004664500254

8. Konoplyuk S., Abe T., Uchimoto T., Takagi T. Ti$_3$SiC$_2$/TiC composites prepared by PDS. *Journal of Materials Science*. 2005;40(13):3409–3413.
https://doi.org/10.1007/s10853-005-0417-1

9. Feng J.C., Cao J., Li Z.R. Microstructure evolution and reaction mechanism during reactive joining of TiAl intermetallic to TiC cermet using Ti–Al–C–Ni interlayer. *Journal of Alloys and Compounds*. 2007;436(1–2):298–302.
https://doi.org/10.1016/j.jallcom.2006.07.040

10. Sytschev A.E., Vadchenko S.G., Boyarchenko O.D., Vrel D., Sachkova N.V. SHS joining of intermetallics with metallic substrates. *International Journal of Self-Propagating High-Temperature Synthesis*. 2011;20(3):185–190.
https://doi.org/10.3103/S1061386211030149

11. Pascal C., Marin-Ayral R.M., Tédenac J.C., Merlet C. Combustion synthesis: a new route for repair of gas turbine components – principles and metallurgical structure in the NiAl/RBD61/superalloy junction. *Materials Science and Engineering: A*. 2003;341(1–2):144–151.
https://doi.org/10.1016/S0921-5093(02)00205-8

12. Novák P., Kříž J., Průša F., Kubásek J., Marek I., Michalcová A., Voděrová M., Vojtěch D. Structure and properties of Ti–Al–Si–X alloys produced by SHS method. *Intermetallics*. 2013;39:11–19.
https://doi.org/10.1016/j.intermet.2013.03.009

13. Novák P., Michalcová A., Šerák J., Vojtěch D., Fabián T., Randáková S., Průša F., Knotek V., Novák M. Preparation of Ti–Al–Si alloys by reactive sintering. *Journal of Alloys and Compounds*. 2009;470(1–2):123–126.
https://doi.org/10.1016/j.jallcom.2008.02.046

14. Novák P., Popela T., Kubásek J., Šerák J., Vojtěch D., Michalcová A. Effect of reactive sintering conditions on microstructure of *in situ* titanium aluminide and silicide composites. *Powder Metallurgy*. 2011;54(1):50–55.
https://doi.org/10.1179/174329009X409651

15. Lazarev P.A., Sytchev A.E., Boyarchenko O.D., Aborkin A.V. Self-propagating high-temperature synthesis in the Ti–Al–Si system. *Inorganic Materials*. 2021;57(11): 1201–1207. https://doi.org/10.1134/s002016852111008x

Лазарев П.А., Сычев А.Е., Боярченко О.Д., Аборкин А.В. Самораспространяющийся высокотемпературный синтез в системе Ti–Al–Si. *Неорганические материалы*. 2021;57(11):1272–1278.
https://doi.org/10.31857/S0002337X21110087

16. Sytschev A.E., Vrel D., Boyarchenko O.D., Vadchenko S.G., Sachkova N.V. Load-assisted SHS joining of NiAl to Ni. *International Journal of Self-Propagating High-Temperature Synthesis*. 2013;22(1):52–55.
https://doi.org/10.3103/S1061386213010111

17. Sytschev A.E., Bondarchuk Yu.V., Pityulin A.N. SHS compunction of multilayer solid alloy/metal materials. *International Journal of Self-Propagating High-Temperature Synthesis*. 1993;2(1):75–83.

18. Pityulin A.N. Force compacting in SHS processes. In: *Self-propagating high-temperature synthesis: theory and practice*. Ed. A.E. Sytschev. Chernogolovka: Territoriya, 2001. P. 333–353. (In Russ.).

Питюлин А.Н. Силовое компактирование в СВС-процессах. В сб.: *Самораспространяющийся высокотемпературный синтез: теория и практика*. Под ред. А.Е. Сычева. Черноголовка: Территория, 2001. С. 333–353.

19. Shcherbakov V.A., Gryadunov A.N., Alymov M.I. Synthesis and characteristics of the B$_4$C–ZrB$_2$ composites. *Letters on Materials*. 2017;7(4):398–401.
https://doi.org/10.22226/2410-3535-2017-4-398-401

20. Palmqvist S. A method to determine the toughness of brittle materials, especially hard materials. *Jernkontorets Ann*. 1957;141:303–307.

21. Knaislová A., Novák P., Cabibbo M., Průša F., Paoletti C., Jaworska L., Vojtěch D. Combination of reaction synthesis and Spark Plasma Sintering in production of Ti–Al–Si alloys. *Journal of Alloys and Compounds*. 2018; 752:317–326.
https://doi.org/10.1016/j.jallcom.2018.04.187

22. Grigorenko S.G., Grigorenko G.M., Zadorozhnyuk O.M. Intermetallics of titanium. Peculiar features, properties, application (Review). *Electrometallurgy Today (Sovremennaya Elektrometallurgiya)*. 2017;(3):51–58.
https://doi.org/10.15407/sem2017.03.08

23. Rohatgi A., Harach D.J., Vecchio K.S., Harvey K.P. Resistance-curve and fracture behavior of Ti–Al$_3$Ti metallic–intermetallic laminate (MIL) composite. *Acta Materialia*. 2003;51(10):2933–2957.
https://doi.org/10.1016/S1359-6454(03)00108-3

24. Trefilov V.I., Milman Yu.V., Gridneva I.V. Mechanical properties of covalent crystals. *Neorganicheskie materialy*. 1984;20(6):958–966. (In Russ.).

Трефилов В.И., Мильман Ю.В., Гриднева И.В. Механические свойства ковалентных кристаллов. *Неорганические материалы*. 1984;20(6):958–966.

25. Haiyang N., Shiwei N., Oganov A.R. Simple and accurate model of fracture toughness of solids. *Journal of Applied Physics*. 2019;125(6):065105. https://doi.org/10.1063/1.5066311

Information about the Authors

Pavel A. Lazarev – Junior Researcher of the Laboratory of physical materials science of Merzhanov Institute of Structural Macrokinetics and Materials Science of the Russian Academy of Sciences (ISMAN)
ORCID: 0000-0003-0275-8811
E-mail: Lazarev@ism.ac.ru

Maria L. Busurina – Cand. Sci. (Eng.), Junior Researcher of the Laboratory of physical materials science of ISMAN
ORCID: 0000-0002-9564-3310
E-mail: busurina@ism.ac.ru

Aleksander N. Gryadunov – Cand. Sci. (Phys.-Math.), Senior Researcher of the Laboratory of energy stimulation of physico-chemical processes of ISMAN
ORCID: 0000-0002-7857-005X
E-mail: gryadunov@ism.ac.ru

Aleksander E. Sytschev – Cand. Sci. (Eng.), Leading Researcher, Head of the Laboratory of physical materials science of ISMAN
ORCID: 0000-0002-6774-2071
E-mail: sytschev@ism.ac.ru

Alevtina F. Belikova – Senior Researcher of the Laboratory of energy stimulation of physico-chemical processes of ISMAN
ORCID: 0000-0002-6197-4381
E-mail: belikova@ism.ac.ru

Сведения об авторах

Павел Андреевич Лазарев – мл. науч. сотрудник лаборатории физического материаловедения, Институт структурной макрокинетики и проблем материаловедения им. А.Г. Мержанова РАН (ИСМАН)
ORCID: 0000-0003-0275-8811
E-mail: Lazarev@ism.ac.ru

Мария Леонидовна Бусурина – к.т.н., мл. науч. сотрудник лаборатории физического материаловедения, ИСМАН
ORCID: 0000-0002-9564-3310
E-mail: busurina@ism.ac.ru

Александр Николаевич Грядунов – к.ф.-м.н., ст. науч. сотрудник лаборатории энергетического стимулирования физико-химических процессов, ИСМАН
ORCID: 0000-0002-7857-005X
E-mail: gryadunov@ism.ac.ru

Александр Евгеньевич Сычев – к.т.н., вед. науч. сотрудник, заведующий лабораторией физического материаловедения, ИСМАН
ORCID: 0000-0002-6774-2071
E-mail: sytschev@ism.ac.ru

Алевтина Федоровна Беликова – ст. науч. сотрудник лаборатории энергетического стимулирования физико-химических процессов, ИСМАН
ORCID: 0000-0002-6197-4381
E-mail: belikova@ism.ac.ru

Contribution of the Authors

P. A. Lazarev – formation of the main concept, goal and objectives of the study; preparation and management of the experiments, writing the text, formulation of the conclusions.
M. L. Busurina – analysis of the research results, conducting the calculations, writing the text.

A. N. Gryadunov – conducting the experiments on press, analysis of the research results.
A. E. Sytschev – scientific guidance, correction of the text and conclusions.
A. F. Belikova – conducting the microhardness measurements for the synthesized samples, metallographic research.

Вклад авторов

П. А. Лазарев – постановка цели и задачи исследования, подготовка к эксперименту, проведение экспериментов, подготовка текста, формулировка выводов.
М. Л. Бусурина – анализ полученных результатов экспериментов и исследований свойств синтезированных образцов, проведение расчетов, подготовка текста статьи.
А. Н. Грядунов – проведение экспериментов на прессе, анализ результатов исследований.
А. Е. Сычев – формирование основной концепции, научное руководство, корректировка текста, корректировка выводов.
А. Ф. Беликова – измерение микротвердости синтезированных сплавов, металлографические исследования.

Received 30.03.2022
Revised 20.05.2022
Accepted 25.05.2022

Статья поступила 30.03.2022 г.
Доработана 20.05.2022 г.
Принята к публикации 25.05.2022 г.

Self-Propagating High-Temperature Synthesis
Самораспространяющийся высокотемпературный синтез

UDC 621.762

https://doi.org/10.17073/1997-308X-2023-1-28-38

Research article
Научная статья

Formation of products upon ignition, combustion and melting of mixtures of high-entropy alloy FeNiCoCrCu with titanium and carbon

S. G. Vadchenko, **Yu. S. Vergunova, A. S. Rogachev,**
I. D. Kovalev, N. I. Mukhina

Merzhanov Institute of Structural Macrokinetics and Materials Science of the Russian Academy of Sciences
8 Akademican Osip'yan Str., Chernogolovka, Moscow region 142432, Russian Federation

vadchenko@ism.ac.ru

Abstract. The dependence of the ignition temperature, combustion rate and composition of the resulting products on the concentration of Ti + C in mixtures with powder of a high-entropy alloy (HEA) FeNiCoCrCu and the initial mixture of metals forming it (MIX) has been studied. HEA was obtained by mechanical activation (MA) of a mixture of metal powders in argon. At the melting temperature, the high-entropy FeNiCoCrCu alloy decomposes into several phases, but the basis of the HEA alloy, as well as the alloy obtained by melting and crystallizing MIX, is a 5-component phase with an average formula $Cu_{1.2}Fe_{1.4}Ni_{1.4}Co_{1.4}Cr$. In addition, 5, 4, and 3-component phases with averaged formulas $Cu_2Ni_2Co_2Fe_2Cr$, $Cu_3Ni_3Co_{2.9}Fe_{2.5}Cr$, $Cu_{4.8}Ni_{4.5}Co_{4.6}Fe_{4.2}Cr$, $Cu_{40}Fe_2Ni_4Co_2C$, $Cr_{12.5}Fe_{3.2}Co_{2.6}Ni$ and $Co_{3.2}Fe_{3.5}Cr$ are present in small amounts in the binder. Experiments on the ignition and combustion of mixtures of MIX and HEA with Ti + C were carried out in argon at atmospheric pressure. The combustion rate, ignition temperature, and maximum temperature reached in the thermal explosion of MIX and HEA mixtures with Ti + C increase with increasing Ti + C concentration. Due to the low exothermicity of the mixtures, the experiments were carried out at an initial temperature of 500 °C. At this initial temperature, the combustion limit of the samples occurs when the Ti + C concentration in the HEA and MIX mixtures is less than 30 %. Based on the results of scanning electron microscopy, the volume concentration of the number of titanium carbide (TiC) particles in molten samples was calculated. In an alloy with a HEA binder, the number of TiC particles per unit volume is 1.5–3.0 times greater than in an alloy with a MIX binder, and their size is correspondingly smaller. With an increase in the concentration of Ti + C from 30 to 40 % in a mixture with HEA, the number of TiC particles per unit volume decreases. In a mixture with MIX, the number of TiC particles per unit volume passes through a minimum. This is due to two opposite processes: on the one hand, the probability of the generation of TiC particles increases, on the other hand, their coagulation occurs.

Keywords: high-entropy alloys, mechanical activation, cermets, titanium carbide, ignition, combustion, melting, energy-releasing additive Ti + C

Acknowledgements: the work was carried out at the expense of a grant from the Russian Science Foundation (Project No. 20-13-00277).

For citation: Vadchenko S.G., Vergunova Yu.S., Rogachev A.S., Kovalev I.D., Mukhina N.I. Formation of products upon ignition, combustion and melting of mixtures of high-entropy alloy FeNiCoCrCu with titanium and carbon. *Powder Metallurgy and Functional Coatings*. 2023;17(1):28–38. https://doi.org/10.17073/1997-308X-2023-1-28-38

Формирование продуктов при воспламенении, горении и плавлении смесей высокоэнтропийного сплава FeNiCoCrCu с титаном и углеродом

С. Г. Вадченко, **Ю. С. Вергунова, А. С. Рогачев,**
И. Д. Ковалев, Н. И. Мухина

Институт структурной макрокинетики и проблем материаловедения им. А.Г. Мержанова РАН
Россия, 142432, Московская обл., г. Черноголовка, ул. Академика Осипьяна, 8

vadchenko@ism.ac.ru

Аннотация. Исследована зависимость температуры воспламенения, скорости горения и состава формирующихся продуктов от концентрации Ti + C в смесях с порошком высокоэнтропийного сплава (ВЭС) FeNiCoCrCu и исходной смесью образующих его металлов (MIX). ВЭС получали методом механической активации (МА) смеси порошков металлов в среде аргона. При температуре плавления высокоэнтропийный сплав FeNiCoCrCu распадается на несколько фаз, но основу этого ВЭС, а также сплава, полученного при плавлении и кристаллизации MIX, составляет 5-компонентная фаза с усредненной формулой $Cu_{1,2}Fe_{1,4}Ni_{1,4}Co_{1,4}Cr$. Кроме того, в небольших количествах в связке присутствуют 5-, 4- и 3-компонентные фазы с усредненными формулами $Cu_2Ni_2Co_2Fe_2Cr$, $Cu_3Ni_3Co_{2,9}Fe_{2,5}Cr$, $Cu_{4,8}Ni_{4,5}Co_{4,6}Fe_{4,2}Cr$, $Cu_{40}Fe_2Ni_4Co_2C$, $Cr_{12,5}Fe_{3,2}Co_{2,6}Ni$ и $Co_{3,2}Fe_{3,5}Cr$. Эксперименты по воспламенению и горению смесей MIX и ВЭС с Ti + C проводили в аргоне при атмосферном давлении. Скорость горения, температура воспламенения и максимальная температура, достигаемая при тепловом взрыве смесей MIX и ВЭС с Ti + C, растут с увеличением концентрации Ti + C. Из-за малой экзотермичности смесей эксперименты проводили при начальной температуре 500 °C – в этом случае предел горения образцов наступает при концентрации Ti + C в смесях ВЭС и MIX <30 %. По результатам сканирующей электронной микроскопии рассчитана объемная концентрация частиц карбида титана (TiC) в расплавленных образцах. В сплаве со связкой из ВЭС количество частиц TiC в единице объема в 1,5–3,0 раза больше, чем в сплаве со связкой из MIX, а их размер соответственно меньше. С повышением концентрации Ti + C от 30 до 40 % в смеси с ВЭС количество числа частиц TiC в единице объема уменьшается. В смеси с MIX объемная концентрация частиц TiC проходит через минимум. Это связано с двумя противоположными процессами – с одной стороны, увеличивается вероятность зарождения частиц TiC, а с другой – происходит их коагуляция.

Ключевые слова: высокоэнтропийные сплавы, механическая активация, керметы, карбид титана, воспламенение, горение, плавление, энерговыделяющая добавка Ti + C

Благодарности: работа выполнена за счет гранта Российского научного фонда (проект № 20-13-00277).

Для цитирования: Вадченко С.Г., Вергунова Ю.С., Рогачев А.С., Ковалев И.Д., Мухина Н.И. Формирование продуктов при воспламенении, горении и плавлении смесей высокоэнтропийного сплава FeNiCoCrCu с титаном и углеродом. *Известия вузов. Порошковая металлургия и функциональные покрытия*. 2023;17(1):28–38. https://doi.org/10.17073/1997-308X-2023-1-28-38

Introduction

High-entropy alloys (HEAs) are a new class of metallic compounds consisting of at least 5 major elements whose concentration varies between 5 and 35 at.%. HEAs generally demonstrate the formation of a simple solid solution structure – VCC, FCC, HCP, or their combinations – instead of intermetallic phases stabilized due to the high configuration entropy of their mixing [1; 2]. Due to the alloys structure peculiarities, they can be used to create new materials with unique properties [3–9].

Recently, HEAs have been considered as a new metallic binder to improve the HEA-based materials performance properties:

– WC–CoCrFeNiMn [10],
– SiC–CoCrFeMnNi [11],
– TiC–FeCrNiCoAlCu [12; 13],
– TiC–FeMnCrNiCo [14],
– TiCN–AlCoCrFeNi [15],
– TiCN–CoCrFeNiCu [16],
– Ti(C,N)–HEA based on (Co, Fe, Ni) [17],
– TiCN–CrMnFeCoNi [18],
– TiC–CoCrFeNi*Me* (*Me* = Mn, Ti, Al) [19].

The work [13] showed that the FeCoCrAlCu HEA-based coatings reinforced with TiC (50 %) obtained by laser surface doping (LSD) have a maximum microhardness of 10.82 GPa, whereas without the reinforcing additive the microhardness was 6.29 GPa. In addition, the TiC inclusions located along the grain boundaries of the HEA prevented their growth and improved the wear resistance. In particular, for the FeCoCrAlCu + 50 % TiC composite coating, the microhardness, wear volume and specific wear rate were 10.78 GPa, $5.2\cdot10^5$ μm^3 and $9.6\cdot10^{-5}$ mm^3/(N·m), respectively.

The authors [16] investigated the mechanical activation effect (MA) on the resulting CoCrFeNiCu HEA-powder properties used as a binder in the Ti(C,N) cermets manufacturing by vacuum sintering. The CoCrFeNiCu HEA-powders were obtained by mechanical fusion in a planetary ball mill. With increasing grinding time (τ_{MA}), the diffraction peaks gradually broaden and their intensities decrease. The face-centered cubic (FCC) phase (111) formation with lattice parameter $a = 3.537$ Å and the secondary volume-centered cubic (VCC) phase (110) release at $a = 2.905$ Å occurred after $\tau_{MA} = 90$ h, and a diffraction peaks slight broadening was observed when τ_{MA}

was increased to 120 h. In the work [16], MA HEA-powders were mixed with $Ti(C_{0.7}N_{0.3})$ (1.2 μm), WC (2.3 μm), Mo_2C (1.75 μm), TaC (1.25 μm) in a ball mill at $v = 56$ rpm and $\tau_{MA} = 72$ h. Despite this two-stage long MA time, the authors [16] conclude that the CoCrFeNiCu HEA is a good variant to use as a new binder in Ti(C,N) based cermets as it has higher fracture strength (8.8 $MPa \cdot m^{-1/2}$) and hardness (1726 HV) compared to conventional nickel-based cermets.

The other authors [17] also used the same methodology: the formation of a single-phase solid solution with a FCC structure and lattice parameter 0.3601 Å of composition CoCrCuFeNi occurred during $\tau_{MA} = 10$ h.

Despite the MA method frequent use for obtaining alloys, its disadvantages are: the long preparation time (10–120 h) and small amounts of obtained materials. At the same time, in the work [20], a single-phase solid solution with an FCC structure and the lattice parameter 3.597 Å with a uniform distribution of all elements was already obtained at $\tau_{MA} = 120$ min.

Earlier [19] the possibility of obtaining cermet based on a high-entropic binder (CoCrFeNiMn, CoCrFeNiTi and CoCrFeNiAl) and an additive mixture of Ti + C by self-propagating high-temperature synthesis (SHS), which is realized due to heat released during the titanium with carbon exothermic reaction, was investigated. In the combustion wave the melting of 5 elements occurs with the multicomponent melt CoCrFeNi*Me* (*Me* = Mn, Ti, Al) formation, which is crystallized in the HEA as a binding phase. The combustion rate and temperature gradually decrease with increasing amount of binder. According to scanning electron microscopy (SEM) and energy dispersive spectroscopy (EDXA) results, all synthesized materials consist of TiC grains and a two-phase (FCC and VCC) metal binder. The Vickers microhardness of the pressed metal-ceramic materials with 30 % binder is in the range of 10–17 GPa, rising with the VCC to FCC ratio increase.

The present work studies for the first time the possibility of obtaining TiC–FeNiCoCrCu cermets with different contents of high-entropic FeNiCoCrCu binder by SHS. The dependence of the ignition temperature, combustion rate and composition of the products formed on the concentration of Ti + C in mixtures with FeNiCoCrCu HEA powder and the initial mixture of the metals forming them was investigated.

Materials and methodology

Titanium powders (PTS-1, 99.6 %, average particle size $d = 50$ μm, production of JSC "Polema", Tula) and carbon (P803, $d = 0.1$ μm, production of LLC PCC "Ekopolza", Astrakhan) in equiatomic ratio were mixed in a porcelain mortar to get a homogeneous mass. Also prepared the equiatomic mixture of iron (R-10, 99.96 %, $d = 10 \div 20$ μm, JSC "Polema", Tula), nickel (PNE-1, 99.5 %, $d = 45 \div 60$ μm, LLC PME "Ural Atomization", Chelyabinsk), cobalt (PC1-U, 99.7 %, $d = 71$ μm, CCM "Ekotek", Moscow), chromium (PKh1, TU 14-1-1474-75, $d < 125$ μm, MC "Atom", Ekaterinburg) and copper (PMS-1, $d = 45 \div 100$ μm, LLC PME "Ural Atomization", Chelyabinsk). All metals of this MIX mixture (Fe + Ni + + Co + Cr + Cu) retained their individuality.

Part of this mixture MIX was subjected to mechanical activation in a planetary mill Activator 2S (CJSC "Activator", Novosibirsk). The processing was carried out in steel drums in an argon atmosphere at a pressure of 4 bar. The ratio of the mixture mass to the balls mass was 1:20, the drums rotational speed was 694 min^{-1}, the processing time – 120 min. As a result, the MA produced particles consisting of the FeNiCoCrCu HEA, which is a solid solution with a face-centered cubic lattice. The particle size distribution was studied with a laser particle analyzer "Microsizer-201C" (VA Instalt, St. Petersburg). Grinding and polishing samples were carried out according to the standard method on a DP-U4 (Struers, Denmark) grinding and polishing machine. Scanning electron microscopy (SEM) was performed on a LEO 1450 VP microscope (Carl-Zeiss SMT AG, Germany). *X*-ray phase analysis (XRD) was performed on diffractometer DRON-3 (Scientific and Production Enterprise "Burevestnik", St. Petersburg) on FeK_α-radiation. MIX and HEA powders were sintered by the spark plasma sintering (SPI) method in a vacuum in the "Labox 650 facility" installation (Sinter Land, Japan) at a load of 50 MPa for 20 min. Microhardness of samples was measured on installation PMT-3 (LOMO, St. Petersburg).

Previously prepared mixtures in the ratio x(Ti + C) and $(100 - x)$MIX, where x = 10, 20, 30, 40, 50, 60, 70, 80 and 90 %, were again mixed in a porcelain mortar until a homogeneous mass was obtained. To obtain relatively homogeneous samples from mixtures of Ti + C with HEA particles with a ratio of x(Ti + C) to $(100 - x)$ HEA, where x = 30, 40, 50, 60 and 70 %, pellets containing 2 to 5 HEA particles surrounded by Ti + C mixture were made using a 2 % butyral resin solution in alcohol. It is difficult to obtain homogeneous mixtures with more Ti + C mixture due to the large difference in the HEAs and titanium particles sizes (Fig. 1).

To study the obtained mixtures ignition parameters the samples with diameter D = 3 and 5 mm and height up to 1D were pressed. The scheme of the experiments to determine the ignition temperature is shown in Fig. 2, *a* [21]. Cylindrical samples were placed on a flat thermocouple 30 μm thick in a crucible made of boron nitride or graphite. The crucible rested on a graphite

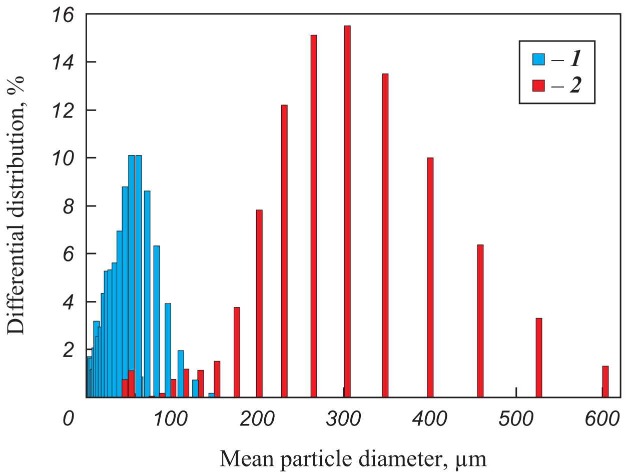

Fig. 1. Titanium (***1***) and HEA (***2***) particle size distribution histogram

Рис. 1. Гистограмма распределения по размерам частиц титана (***1***) и ВЭС (***2***)

strip heated by an electric current to the sample ignition or melting temperature.

To study combustion, the samples were pressed in the form of 6×30 mm plates with a thickness of 2.5–3.0 mm. The relative density of the samples was 0.45–0.5. They were placed between two graphite blocks with heaters inside. Combustion was initiated by a coil heated by an electric current. The samples combustion rate was determined as the ratio of the distance between the thermocouples T1–T2–T3 to the time of the combustion wave passing between them. The experiments were performed in argon at atmospheric pressure.

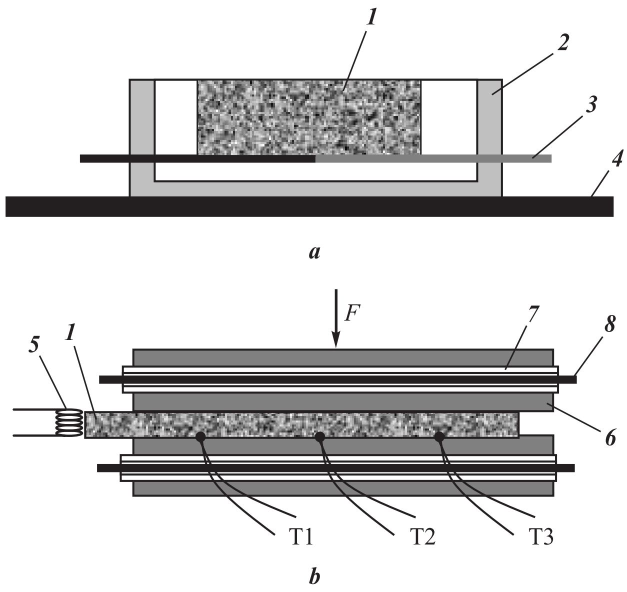

Fig. 2. Samples (***a***) and the combustion rate (***b***) measuring the ignition temperature schemes
1 – sample, ***2*** – crucible, ***3*** – thermocouple, ***4*** – graphite heater strip, ***5*** – initiating coil, ***6*** – graphite plate with heaters, ***7*** – Al_2O_3 tubes, ***8*** – heater, *F* – load, T1–T3 – thermocouples

Рис. 2. Схемы измерения температуры воспламенения образцов (***а***) и скорости горения (***b***)
1 – образец, ***2*** – тигель, ***3*** – термопара, ***4*** – графитовый ленточный нагреватель, ***5*** – инициирующая спираль, ***6*** – графитовая пластина с нагревателями, ***7*** – трубки из Al_2O_3, ***8*** – нагреватель, *F* – нагрузка, T1–T3 – термопары

Results and discussion

Ignition

Figure 3 shows characteristic thermograms of the ignition of samples pressed from the initial powders at different concentrations in the mixture Ti + C. The Ti + C mixture samples ignition temperature is about 1200 °C. When the concentration of Ti + C is reduced to 80 %, the metal mixtures ignition temperature is $t = 1080 \pm 30$ °C. The lowering of the ignition temperature of mixtures containing copper may be due to its melting ($t_m = 1083$ °C). The copper melting increases its volume by 6 vol.% [22], which leads to better contacts between the particles, and also starts the reaction of titanium with copper, which, despite the weak exothermicity (calculated values of formation CuTi enthalpy – 79 kJ/mol [23]), can initiate the titanium with carbon interaction.

The ignition temperatures of samples from mixtures based on HEA-powders at the Ti + C concentration in the mixture equal to 30–70 % are close to the ignition temperature of the initial mixture Ti + C, since due to the large size of HEA-particles they play the role of an inert diluent.

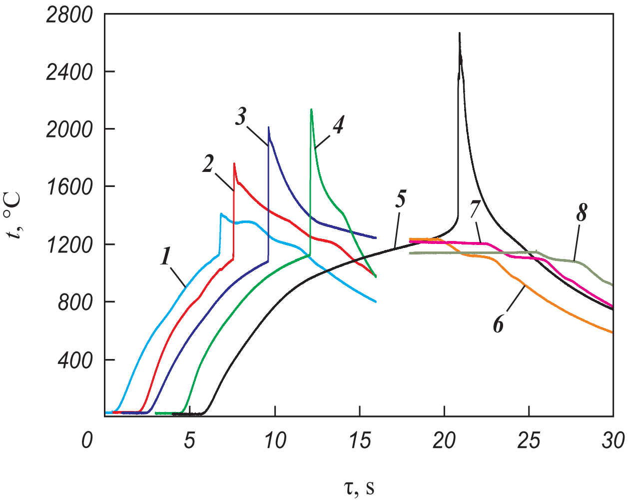

Fig. 3. Initial mixtures (Ti + C) + MIX ignition (***1***–***5***) and cooling (***6***–***8***) thermograms characteristic view
Ti + C, %: 30 (***1***), 40 (***2***), 60 (***3***), 80 (***4***), 100 (***5***), 20 (***6***–***8***)

Рис. 3. Характерный вид термограмм воспламенения (***1***–***5***) и охлаждения (***6***–***8***) исходных смесей (Ti + C) + MIX
Ti + C, %: 30 (***1***), 40 (***2***), 60 (***3***), 80 (***4***), 100 (***5***), 20 (***6***–***8***)

When cooling the compositions ignition products with Ti + C concentration equal to 30–40 %, two inflections (plateaus) around 1360 and 1200 °C are observed in the thermograms associated with crystallization of the melt of polymetallic binder. The temperature of the first plateau is close to the temperature of endothermic peaks observed in differential scanning calorimetry (DSC) Fe + Ni + Co + Cr + Cu (1359 °C) mixture and FeNiCoCrCu (1365 °C) HEA in the work [20], and caused in the first case, apparently, the resulting compound melting. At Ti + C higher contents, the used method does not allow to register this effect. At the Ti + C content of 10–20 % in the mixture, a plateau near 1200 °C (Fig. 3, curves *6*–*8*) and an inflection near 1100 °C are also observed during cooling.

Combustion

During the samples combustion, size and density practically did not change, since they were under load (compression pressure $F = 0.1$ MPa). Figure 4 shows the combustion products surface structure. Large pores up to 0.5 mm in the sample 0.4(Ti + C) + 0.6HEA were formed as a result of HEA-particles melting and TiC framework melt spreading.

The initial samples density, calculated as the measured mass to the geometric volume ratio is shown in Table 1. Since the experiments were carried out under load, the samples size changes after combustion were insignificant.

Combustion thermograms characteristic view is shown in Fig. 5. Since at less than 60 % Ti + C in the mixture at room temperature the samples did not burn or burn unstably, all experiments were conducted at an initial temperature of 500 ± 10 °C. Samples with [Ti + C] concentrations ≤30 % did not burn at this initial temperature.

Figure 6 shows the dependence on the Ti + C concentration of the mixtures with MIX and HEA combustion rate and the mixtures Ti + C and MIX difference $\Delta t = t_{\max} - t_{\text{ig}}$ between the maximum temperature reached at ignition and the ignition temperature. At a small difference Δt, the self-propagating combustion mode is not realized in this system.

The main contribution to heat release during mixtures ignition and combustion is made by the titanium carbide formation reaction. Titanium can also react with the heat emission with all metals included in the HEA-mixture, and chromium can interact with carbon to form carbide Cr_3C_2. The formation enthalpy of all these compounds is much less than for the Ti + C reaction, and these compounds are not detected on the *X*-rays. But the reaction mechanisms of composite formation when using MIX and HEA as a binder are different, which is due to the difference in the Ti + C mixtures structure. In the former case, the contact surface between titanium and carbon particles is much smaller because the unit cell of the mixture consists of metal particles and carbon distributed between them. Assuming that the metal particles are close in size, then per titanium particle in the cell, depending on Ti + C concentration, there are approximately from 1 (when $x = 90$ % Ti + C) to 20

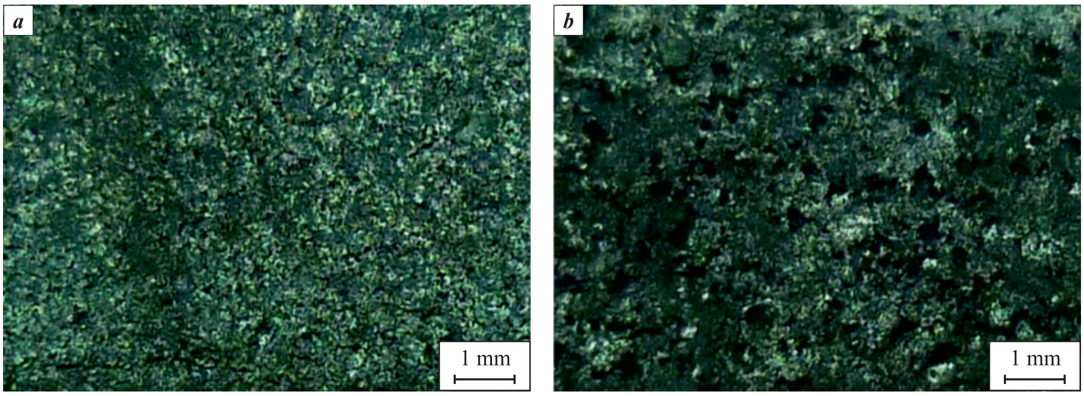

Fig. 4. 0.4(Ti + C) + 0.6MIX (***a***) and 0,4(Ti + C) + 0,6MIX (***b***) mixtures combustion products surface structure

Рис. 4. Структура поверхности продуктов горения смесей 0,4(Ti + C) + 0,6MIX (***a***) и 0,4(Ti + C) + 0,6ВЭС (***b***)

Table 1. **Samples density, g/cm³, from Ti + C with MIX and HEA mixtures**

Таблица 1. **Плотность образцов, г/см³, из смесей Ti + C с MIX и ВЭС**

Binder composition	Ti + C, %							
	30	40	50	60	70	80	90	100
MIX	3.23	3.02	2.51	2.51	2.50	2.04	1.88	1.85
HEA	3.20	3.01	2.79	2.78	2.48	–	–	1.85

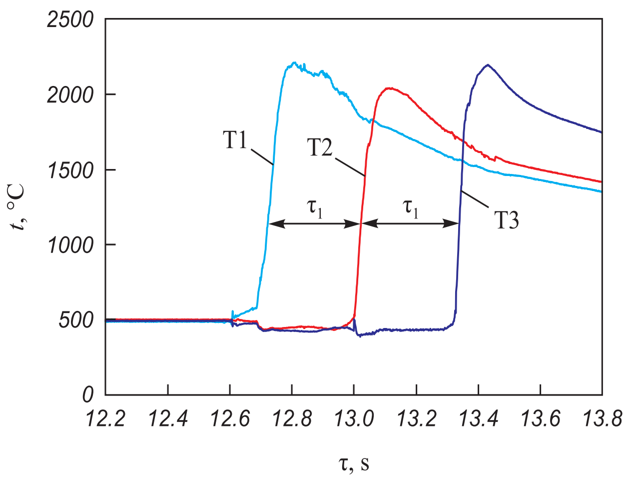

Fig. 5. Mixture 70(Ti + C) + 30MIX sample combustion thermogram

Рис. 5. Термограмма горения образца из смеси 70(Ti + C) + 30MIX

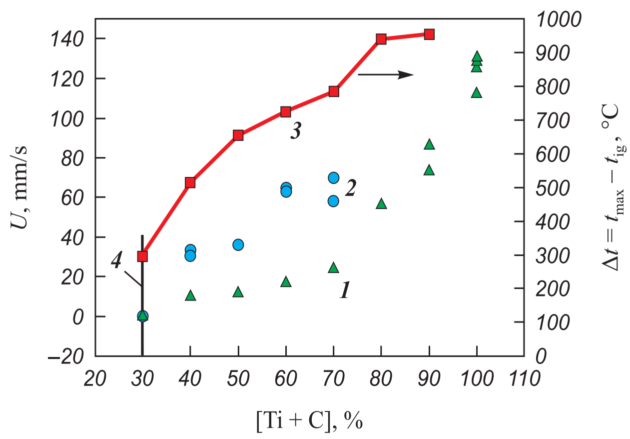

Fig. 6. Dependence of the combustion rate on the concentration of Ti + C in mixtures with MIX (*1*) and with HPS (*2*)
3 – difference between the maximum temperature reached at ignition and the ignition temperature
4 – combustion limit

Рис. 6. Зависимость скорости горения от концентрации Ti + C в смесях с MIX (*1*) и с ВЭС (*2*)
3 – разность между максимальной температурой, достигаемой при воспламенении, и температурой воспламенения
4 – предел горения

(when $x = 10$ % Ti + C) particles of other metals. In the latter case, the titanium particle is surrounded by a small portion of carbon, i.e., the Ti + C mixture appears diluted in both thermal and concentration (Ti/C) terms. As the Ti + C concentration decreases, the mechanism of propagation of the combustion wave changes from frontal to percolation. The HEA-powder particles case whose are several times larger than those of the parent metals, only thermal dilution takes place, and the transition from the frontal to percolation combustion mechanism occurs at lower Ti + C concentrations [24].

Figure 7 shows the combustion products change in the phase composition from FeNiCoCrCu to TiC alloys when the Ti + C concentration in the mixture increases from 0 to 100 %.

Mixtures ignition and melting products

At high concentrations in titanium and carbon mixtures high temperatures developed during the samples ignition and combustion, leading to melting of the high-entropic binder or mixture of metals forming it and carbide grains formation. To compare the changes occurring in the MIX and HEA metal mixture binder structure, the powders were heated to the melting temperature. Figure 8 shows characteristic heating and cooling thermograms.

When a metals Fe + Ni + Co + Cr + Cu and HEA mixture is heated to the melting temperature and subsequently crystallized, several plateaus appear on the thermograms. The plateau at heating near 1100 °C occurs due to copper melting. Endothermic peak at close temperatures was observed at DSC of this mixture (1083 °C) and the alloy (1115 °C) in work [20]. Endothermic peaks associated with the melting of the whole composition – metal mixture (1359 °C) and the alloy (1365 °C) – were also observed there.

When cooling the samples after melting the first plateau appears at about 1200 °C and is associated with the crystallization of a more refractory phase – apparently, the main 5-component high-entropic phase. The second plateau at about 1000 °C is due to copper-enriched phase crystallization.

While melting the samples pressed from MIX and HEA powders, several phases are released from the melt (Fig. 9). The basis of the molten MIX and HEA samples is a 5-component phase with the averaged formula of $Cu_{1.2}Fe_{1.4}Ni_{1.4}Co_{1.4}Cr$. In addition, the 5-component phases $Cu_2Ni_2Co_2Fe_2Cr$, $Cu_3Ni_3Co_{2.9}Fe_{2.5}Cr$, $Cu_{4.8}Ni_{4.5}Co_{4.6}Fe_{4.2}Cr$, $Cu_{40}Fe_2Ni_4Co_2Cr$, $Cu_{40}Fe_2Ni_4Co_2Cr$, 4-component with the averaged formula $Cr_{12.5}Fe_{3.2}Co_{2.6}Ni$, and 3-component with the averaged formula $Co_{3.2}Fe_{3.5}Cr$. During MIX and HEA melting, as well as during ignition and combustion of their mixtures with Ti + C, some of the copper evaporates and precipitates on the sight glass and cold reactor parts.

It is possible that the MIX and HEA melts (Fig. 9) represent the same FCC solid solution but not quite homogeneous in its chemical composition. Part of the chromium is consumed to form ternary and quaternary phases with high chromium concentration, containing no copper and crystallizing in the form of hexagonal tubes filled with the main phase. Concentrations of phases enriched with copper (Fig. 9, 1*a*, 2*a*) or chromium (Fig. 9, 1*b*, 2*b*) are relatively low and do not show up on the *X*-ray diffraction patterns (Fig. 10, diffractograms *1*, *2*). Figure 10 also

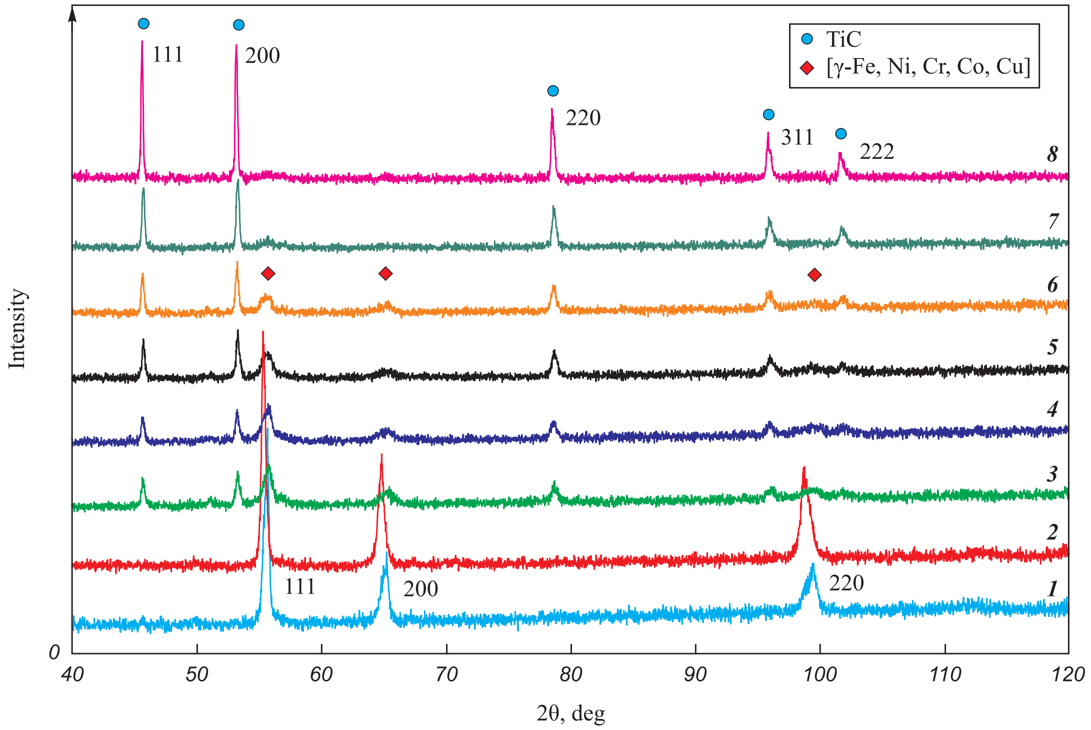

Fig. 7. Mixtures melting products (***1***, ***2***) and combustion products (***3–8***) *X*-ray patterns
1 – MIX, ***2*** – HEA, ***3*** – 40TiC–60MIX, ***4*** – 40TiC–60HEA, ***5*** – 60TiC–40MIX, ***6*** – 60TiC–40HEA, ***7*** – 80TiC–20MIX, ***8*** – TiC

Рис. 7. Рентгенограммы продуктов плавления (***1***, ***2***) и горения (***3–8***) смесей
1 – MIX, ***2*** – ВЭС, ***3*** – 40TiC–60MIX, ***4*** – 40TiC–60ВЭС, ***5*** – 60TiC–40MIX, ***6*** – 60TiC–40ВЭС, ***7*** – 80TiC–20MIX, ***8*** – TiC

shows *X*-ray diffraction patterns of products obtained by sintering using the SPS method [19]. The peaks shift to the left on the samples *X*-ray patterns after the MIX and HEA powders melting, as compared to the sintered samples. The chemical composition heterogeneity is evident during sintering at $t = 800$ and 900 °C. At these temperatures the second phase emerges and the peaks split (Fig. 10, diffractograms *3*, *4*). Both phases formed have a FCC structure. At sintering temperature of 1000 °C composition homogenization occurs.

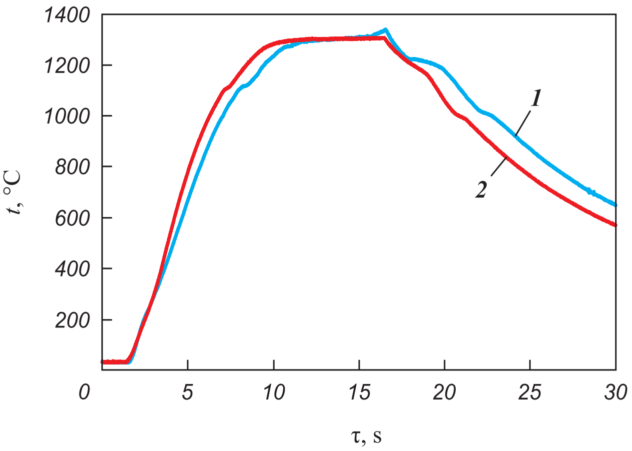

Fig. 8. MIX (*1*) and HEA (*2*) heating thermograms

Рис. 8. Термограммы нагрева MIX (*1*) и ВЭС (*2*)

Figure 11 shows photographs of microstructures formed during melt crystallization as a result of Ti + C mixtures with MIX and HEA reactions. The dark particles are titanium carbide (TiC). The binder is heterogeneous and includes the same constituents that are released during HEA or MIX melting.

The results of counting the TiC particles number (n) in the molten samples were carried out on the area of the polished section $S = 2{,}500 \div 10{,}500$ μm^2 and the volume concentration of particles was calculated by the formula $N = (n/S)^{3/2}$. Table 2 shows the average values from the results of measurements on several polished sections. In the HEA-bonded alloy the number of titanium carbide particles per unit volume was 1.5–3.0 times higher than in the MIX-bonded alloy, and the particle size was correspondingly smaller. As the Ti + C concentration increases from 30 to 40 % in the mixture with HEA, the number of titanium carbide particles per unit volume decreases. In the mixture with MIX the number of particles per unit volume passes through the minimum. This may be due to two processes – on the one hand, the particles nucleation probability increases, and on the other hand, titanium carbide particles coagulation occurs.

Figure 11 also shows that as the concentration of titanium carbide increases, the size of the phases that make up the bond decreases. The basis of the binder, as in the case of the molten MIX and HEA samples,

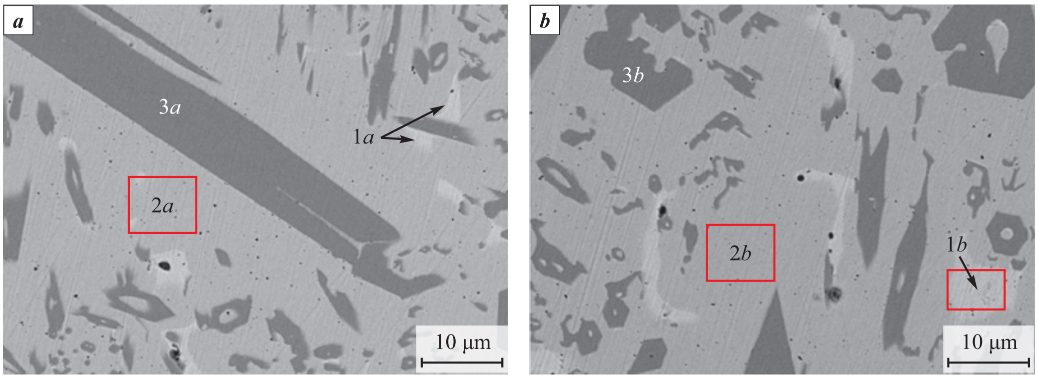

Range	Cr	Fe	Co	Ni	Cu
1*a*	2.4	8.4	7.7	9.9	71.5
2*a*	12.4	23.8	24.9	20.5	18.3
3*a*	80.1	11.3	8.6	–	–
1*b*	1.4	4.1	3.5	6.5	84.6
2*b*	14.8	21.2	22.5	21.5	20.0
3*b*	78.4	11.2	7.8	2.6	–

Fig. 9. MIX (***a***) and HEA (***b***) melts phases structure and composition (at. %)

Рис. 9. Структура и состав (ат. %) фаз расплавов MIX (***a***) и ВЭС (***b***)

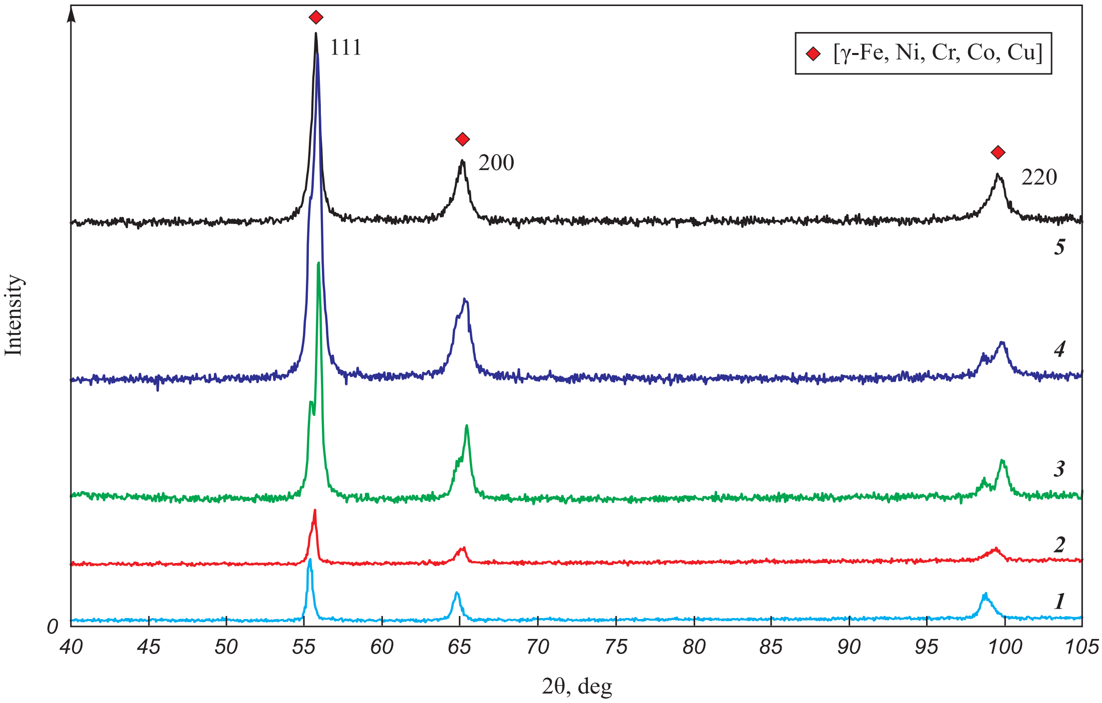

Fig. 10. SPS method melting and sintering products *X*-ray patterns
1 – HEA melt, ***2*** – MIX melt, ***3*** – HEA SPS (800 °C), ***4*** – HEA SPS (900 °C), ***5*** – HEA SPS (1000 °C)

Рис. 10. Рентгенограммы продуктов плавления и спекания методом ИПС
1 – расплав ВЭС, ***2*** – расплав MIX, ***3*** – ВЭС ИПС (800 °C), ***4*** – ВЭС ИПС (900 °C), ***5*** – ВЭС ИПС (1000 °C)

is a 5-component phase with the averaged formula $Cu_{1.2}Fe_{1.4}Ni_{1.4}Co_{1.4}Cr$ with small additions of the above 5-, 4- and 3-component phases.

The microhardness of samples MIX and HEA without carbide grains is in the range of 2.4–6.9 GPa. Its minimum value corresponds to areas with high copper content, maximum – with high chromium concentration. Microhardness of MIX and HEA samples with 30–70 % Ti + C in the initial mixture is 3.6–10.0 GPa and partially depends on copper and chrome concentra-

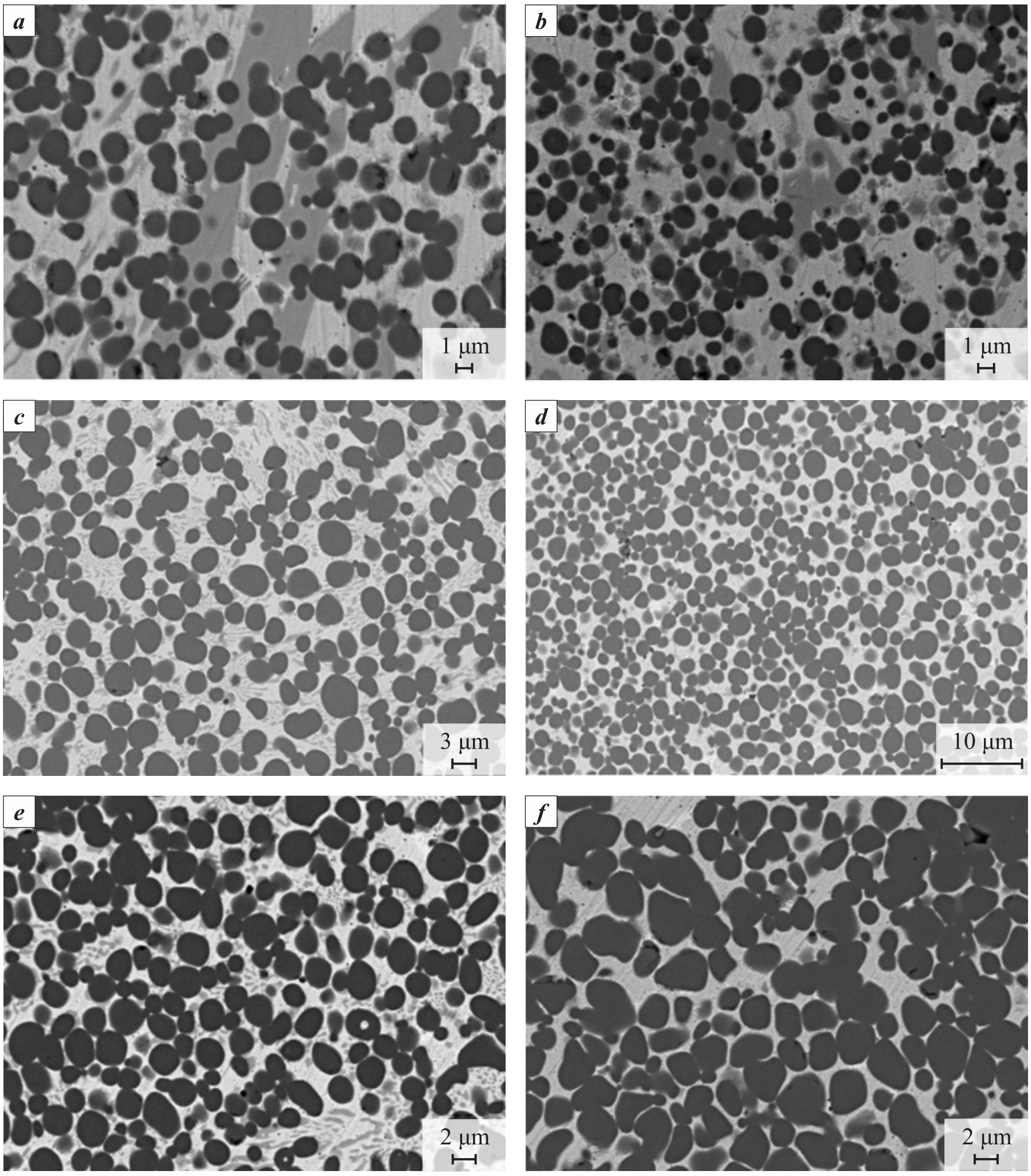

Fig. 11. The alloys microstructure after melt crystallization
a – 30(Ti + C) + 70MIX; ***b*** – 30(Ti + C) + 70HEA; ***c*** – 40(Ti + C) + 60MIX;
d – 40(Ti + C) + 60HEA; ***e*** – 60(Ti + C) + 40MIX; ***f*** – 70(Ti + C) + 30MIX

Рис. 11. Микроструктура сплавов после кристаллизации расплава
a – 30(Ti + C) + 70MIX; ***b*** – 30(Ti + C) + 70ВЭС; ***c*** – 40(Ti + C) + 60MIX;
d – 40(Ti + C) + 60ВЭС; ***e*** – 60(Ti + C) + 40MIX; ***f*** – 70(Ti + C) + 30MIX

tion, but the main contribution to microhardness values is made by the TiC particles closeness to each other and their even distribution throughout the cermet volume. The TiC particles microhardness is 25–35 GPa and corresponds to the known data [25].

Conclusion

The possibility of obtaining cermets with a high-entropic binder by using a mixture of titanium and carbon forming TiC particles as an energy additive was shown. This makes it possible to reduce the cer-

Table 2. **Alloys TiC particles volume concentration**

Таблица 2. **Объемная концентрация частиц TiC в сплавах**

No.	Composition	N, 10^3 mm^{-3}
1	30(Ti + C) + 70HEA	200
2	40(Ti + C) + 60HEA	112
3	30(Ti + C) + 70MIX	117
4	40(Ti + C) + 60MIX	37
5	60(Ti + C) + 40MIX	54
6	70(Ti + C) + 30MIX	105

met production energy costs by carrying out the process in combustion or thermal explosion mode. At the initial temperature of 500 °C, the combustion limit of the samples comes at the Ti + C concentration less than 30 %. During the cermet synthesis the high-entropic alloy FeNiCoCrCu binder splits into several phases, but the basis of the alloy is formed by a 5-component phase with the averaged formula $Cu_{1.2}Fe_{1.4}Ni_{1.4}Co_{1.4}Cr$.

Preliminary HEA production by mechanical alloying is not a necessary stage of initial powders preparation process, since the high-entropic binder is formed from a mixture of initial metals during the high-temperature cermet synthesis. The number of TiC particles in the volume unit in cermet with a binder from a pre-prepared HEA is 1.5–3.0 times higher than in an alloy with a binder from a mixture of metals.

References / Список литературы

1. Yeh J.-W., Chen S.-K., Lin S.-J., Gan J.-Y., Chin T.-S., Shun T.-T., Tsau C.-H., Chang S.-Y. Nanostructured high-entropy alloys with multiple principal elements: novel alloy design concepts and outcomes. *Advanced Engineering Materials*. 2004;6(5):299–303. https://doi.org/10.1002/adem.200300567
2. Cantor B., Chang I.T.H., Knight P., Vincent A.J.B. Microstructural development in equiatomic multicomponent alloys. *Materials Science and Engineering: A*. 2004;375–377: 213–218. https://doi.org/10.1016/j.msea.2003.10.257
3. Gludovatz B., Hohenwarter A., Catoor D., Chang E.H., George E.P., Ritchie R.O. A fracture-resistant high-entropy alloy for cryogenic applications. *Science*. 2014;345(6201): 1153–1158. https://doi.org/10.1126/science.1254581
4. Lee C.P., Chen Y.Y., Hsu C.Y., Yeh J.W., Shih H.C. The effect of boron on the corrosion resistance of the high entropy alloys $Al_{0.5}CoCrCuFeNiB_x$. *Journal of the Electrochemical Society*. 2007;154(8):424–430. https://doi.org/10.1149/1.2744133
5. Shkodich N.F., Kuskov K.V., Sedegov A.S., Kovalev I.D., Panteleeva A.V., Vergunova Yu.S., Scheck Yu.B., Panina E., Stepanov N., Serhiienko I., Moskovskikh D. Refractory TaTiNb, TaTiNbZr, and TaTiNbZrX (X = Mo, W) high entropy alloys by combined use of high energy ball milling and spark plasma sintering: Structural characterization, mechanical properties, electrical resistivity, and thermal conductivity. *Journal of Alloys and Compounds*. 2022;893:162030. https://doi.org/10.1016/j.jallcom.2021.162030
6. Zuo T.T., Gao M.C., Ouyang L.Z., Yang X., Cheng Y.Q., Feng R., Chen S.Y., Liaw P. K., Hawk J.A., Zhang Y. Tailoring magnetic behavior of CoFeMnNiX (X = Al, Cr, Ga, and Sn) high entropy alloys by metal doping. *Acta Materialia*. 2017;130:10–18. https://doi.org/10.1016/j.actamat.2017.03.013
7. Tsai M.-H., Yeh J.-W. High-entropy alloys: A critical review. *Materials Research Letters*. 2014;2(3):107–123. https://doi.org/10.1080/21663831.2014.912690
8. Ye Y.F., Wang Q., Lu J., Liu C.T., Yang Y. High-entropy alloy: challenges and prospects. *Materials Today*. 2016;19(6):349–362. https://doi.org/10.1016/j.mattod.2015.11.026
9. Miracle D.B., Senkov O.N. A critical review of high entropy alloys and related concepts. *Acta Materialia*. 2017;122: 448–511. https://doi.org/10.1016/j.actamat.2016.08.081
10. Velo I.L., Gotor F.J., Alcalá M.D., Real C., Córdoba J.M. Fabrication and characterization of WC-HEA cemented carbide based on the CoCrFeNiMn high entropy alloy. *Journal of Alloys and Compounds*. 2018;746:1–8. https://doi.org/10.1016/j.jallcom.2018.02.292
11. Rogal L., Kalita D., Tarasek A., Bobrowski P., Czerwinski F. Effect of SiC nano-particles on microstructure and mechanical properties of the CoCrFeMnNi high entropy alloy. *Journal of Alloys and Compounds*. 2017;708:344–352. https://doi.org/10.1016/j.jallcom.2017.02.274
12. Fan Q.C., Li B.S., Zhang Y. The microstructure and properties of $(FeCrNiCo)Al_xCu_y$ high-entropy alloys and their TiC-reinforced composites. *Materials Science and Engineering: A*. 2014;598:244–250. https://doi.org/10.1016/j.msea.2014.01.044
13. Jiang P.F., Zhang C.H., Zhang S., Zhang J.B., Chen J., Liu Y. Fabrication and wear behavior of TiC reinforced FeCoCrAlCu-based high entropy alloy coatings by laser surface alloying. *Materials Chemistry and Physics*. 2020;255:123571. https://doi.org/10.1016/j.matchemphys.2020.123571
14. Cai Y., Zhu L., Cui Y., Shan M., Li H., Xin Y., Han J. Fracture and wear mechanisms of FeMnCrNiCo + x(TiC) composite high-entropy alloy cladding layers. *Applied Surface Science*. 2021;543:148794. https://doi.org/10.1016/j.apsusc.2020.148794
15. Zhu G., Liu Y., Ye J. Fabrication and properties of Ti(C,N)-based cermets with multi-component AlCoCrFeNi high-entropy alloys binder. *Materials Letters*. 2013;113:80–82. https://doi.org/10.1016/j.matlet.2013.08.087
16. Wang Z., Xiong J., Guo Z., Yang T., Liu J., Chai B. The microstructure and properties of novel Ti(C,N)-based cermets with multi-component CoCrFeNiCu high-entropy alloy binders. *Materials Science and Engineering: A*. 2019;766:138345. https://doi.org/10.1016/j.msea.2019.138345
17. De la Obra A.G., Sayagués M.J., Chicardi E., Gotor F.J. Development of Ti(C,N)-based cermets with (Co,Fe,Ni)-based high entropy alloys as binder phase. *Journal of Alloys and Compounds*. 2020;814;152218. https://doi.org/10.1016/j.jallcom.2019.152218
18. Yang S., Xiong J., Guo Z., Wu B., Yang T., You Q., Liu J., Deng C., Fang D., Gou S., Yu Z., Chend S. Effects of CrMnFeCoNi additions on microstructure, mechanical properties and wear resistance of Ti(C,N)-based cermets. *Journal of Materials Research and Technology*. 2022;17: 2480–2494. https://doi.org/10.1016/j.jmrt.2022.02.021
19. Rogachev A.S., Vadchenko S.G., Kochetov N.A., Kovalev D.Yu., Kovalev I.D., Shchukin A.S., Gryadunov A.N., Baras F., Politano O. Combustion synthesis of TiC-based ceramic-metal composites with high entropy alloy binder. *Journal of the European Ceramic Society*. 2020;40(7):2527–2532. https://doi.org/10.1016/j.jeurceramsoc.2019.11.059

20. Shkodich N.F., Kovalev I.D., Kuskov K.V., Kovalev D.Yu., Vergunova Yu.S., Scheck Yu.B., Vadchenko S.G., Politano O., Baras F., Rogachev A.S. Fast mechanical synthesis, structure evolution, and thermal stability of nanostructured CoCrFeNiCu high entropy alloy. *Journal of Alloys and Compounds*. 2022;893:161839.
https://doi.org/10.1016/j.jallcom.2021.161839

21. Vadchenko S.G., Boyarchenko O.D., Shkodich N.F., Rogachev A.S. Thermal explosion in various Ni–Al systems: Effect of mechanical activation. *International Journal of Self-Propagating High-Temperature Synthesis*. 2013;22(1):60–64.
https://doi.org/10.3103/S1061386213010123

22. Inyukhin M.V., Korzhavyi A.P., Prasitskii G.V. Parameters and techniques of receiving of heat-absorbent materials for semiconductor device. *Naukoemkie tekhnologii*. 2014;15(2):10–19. (In Russ.).

Инюхин М.В., Коржавый А.П., Прасицкий Г.В. Параметры и техника получения теплоотводящих материалов для полупроводниковых приборов. *Наукоемкие технологии*. 2014;15(2):10–19.

23. Shirasawa N., Takigawa Y., Uesugi T., Higashi K. Calculation of alloying effect on formation enthalpy of TiCu intermetallics from first-principles calculations for designing Ti–Cu-system metallic glasses. *Philosophical Magazine Letters*. 2016;96(1):27–34.
https://doi.org/10.1080/09500839.2015.1134833

24. Grinchuk P.S., Rabinovich O.S. Percolation phase transition in combustion of heterogeneous mixtures. *Combustion, Explosion and Shock Waves*. 2004; 40(4):408–418.
https://doi.org/10.1023/B:CESW.0000033563.66432.1c

Гринчук П.С., Рабинович О.С. Перколяционный фазовый переход при горении гетерогенных смесей. *Физика горения и взрыва*. 2004;40(4):41–53.

25. Carbide, nitride, and boride materials synthesis and processing. Ed. A.W. Weimer. London: Publ. Chapman & Hall, 1997. 671 p.

Information about the Authors

Sergei G. Vadchenko – Cand. Sci. (Phys.-Math.), Leading Researcher, Laboratory of dynamics of microheterogeneous processes, Merzhanov Institute of Structural Macrokinetics and Materials Science of the Russian Academy of Sciences (ISMAN)
ORCID: 0000-0002-2360-2114
E-mail: vadchenko@ism.ac.ru

Yulia S. Vergunova – Postgraduate Student, Laboratory of dynamics of microheterogeneous processes of ISMAN
ORCID: 0000-0002-9805-2575
E-mail: yulya-ser94@yandex.ru

Aleksander S. Rogachev – Dr. Sci. (Phys.-Math.), Prof., Head of the Laboratory of dynamics of microheterogeneous processes of ISMAN
ORCID: 0000-0003-1554-0803
E-mail: rogachev@ism.ac.ru

Ivan D. Kovalev – Cand. Sci. (Phys.-Math.), Senior Researcher, Laboratory of *X*-ray investigation of ISMAN
ORCID: 0000-0003-4710-837X
E-mail: i2212@yandex.ru

Nina I. Mukhina – Technologist, Laboratory of materials science of ISMAN
ORCID: 0000-0002-5089-0908
E-mail: muxinanina2012@yandex.ru

Сведения об авторах

Сергей Георгиевич Вадченко – к.ф.-м.н., вед. науч. сотрудник лаборатории динамики микрогетерогенных процессов, Институт структурной макрокинетики и проблем материаловедения им. А.Г. Мержанова РАН (ИСМАН)
ORCID: 0000-0002-2360-2114
E-mail: vadchenko@ism.ac.ru

Юлия Сергеевна Вергунова – аспирант лаборатории динамики микрогетерогенных процессов, ИСМАН
ORCID: 0000-0002-9805-2575
E-mail: yulya-ser94@yandex.ru

Александр Сергеевич Рогачев – д.ф.-м.н., проф., заведующий лабораторией динамики микрогетерогенных процессов, ИСМАН
ORCID: 0000-0003-1554-0803
E-mail: rogachev@ism.ac.ru

Иван Дмитриевич Ковалев – к.ф.-м.н., ст. науч. сотрудник лаборатории рентгеноструктурных исследований, ИСМАН
ORCID: 0000-0003-4710-837X
E-mail: i2212@yandex.ru

Нина Илларионовна Мухина – технолог лаборатории физического материаловедения, ИСМАН
ORCID: 0000-0002-5089-0908
E-mail: muxinanina2012@yandex.ru

Contribution of the Authors

S. G. Vadchenko – setting the goal and objectives of the study, preparing the text, formulating conclusions.
Yu. S. Vergunova – preparation and conduct of the experiment, management of the experiment.
A. S. Rogachev – scientific guidance, the formation of the main concept, text correction, correction of conclusions.
I. D. Kovalev – *X*-ray phase analysis.
N. I. Mukhina – sample preparation and SEM.

Вклад авторов

С. Г. Вадченко – постановка цели и задачи исследования, подготовка текста, формулировка выводов.
Ю. С. Вергунова – подготовка и проведение эксперимента, руководство проведением эксперимента.
А. С. Рогачев – научное руководство, формирование основной концепции, корректировка текста, корректировка выводов.
И. Д. Ковалев – проведение рентгенофазового анализа.
Н. И. Мухина – подготовка образцов и СЭМ.

Received 19.04.2022
Revised 23.05.2022
Accepted 25.05.2022

Статья поступила 19.04.2022 г.
Доработана 23.05.2022 г.
Принята к публикации 25.05.2022 г.

Self-Propagating High-Temperature Synthesis
Самораспространяющийся высокотемпературный синтез

UDC 546.05

https://doi.org/10.17073/1997-308X-2023-1-39-48

Research article
Научная статья

SHS of cast materials in the Mo–Al–C system

V. A. Gorshkov, P. A. Miloserdov, D. Yu. Kovalev,
O. D. Boyarchenko

Merzhanov Institute of Structural Macrokinetics and Materials Science of the Russian Academy of Sciences
8 Akademican Osip'yan Str., Chernogolovka, Moscow region 142432, Russian Federation

gorsh@ism.ac.ru

Abstract. Materials based on molybdenum-aluminium-carbon compounds have a considerable potential for use under intense wear conditions at elevated temperatures. This paper presents the experimental results of self-propagating high-temperature synthesis of compounds within the Mo–Al–C system. By combining two processes: SHS of the elements and SHS-metallurgy, cast materials containing the Mo_3Al_2C, Mo_2C, Mo_3Al, and Mo_3Al_8 phases were obtained. The experiments used mixtures with compositions calculated according to the ratio $(1 - \alpha)(3MoO_3–8Al–C)/\alpha(3Mo–2Al–C)$, where α varied in the range from 0 to 1. The synthesis was carried out in a laboratory reactor of 3 L volume at an initial argon pressure of 5 MPa. The mass of the initial mixtures in all experiments was 20 g. The process of combustion was initiated by a 0.5 mm diameter molybdenum wire spiral by applying 28 V voltage to it. The resulting end products were studied by *X*-ray diffraction and local microstructural analysis. A significant influence of the ratio of the initial reagents on the synthesis parameters, phase composition, and microstructure of the target products was established. Introduction into the high-exothermic mixture $3MoO_3–8Al–C$ inert "cold" mixture 3Mo–2Al–C leads to an increase in the content of carbide phases in the ingots. The possibility of obtaining cast materials based on the triple phase Mo_3Al_2C, the maximum content of which is 87 wt. % at the content of the "cold" mixture in the charge $\alpha = 0.4$ is shown. The presence of secondary phases of molybdenum carbide (Mo_2C) and molybdenum aluminides (Mo_3Al_8, Mo_3Al) in the final products is due to a change in the composition of the initial mixture caused by the ejection of components during combustion and insufficient existence time of the melt formed in the combustion wave.

Keywords: self-propagating high-temperature synthesis, Mo–Al–C system, microstructure, phase composition

For citation: Gorshkov V.A., Miloserdov P.A., Kovalev D.Yu., Boyarchenko O.D. SHS of cast materials in the Mo–Al–C system. *Powder Metallurgy and Functional Coatings*. 2023;17(1):39–48. https://doi.org/10.17073/1997-308X-2023-1-39-48

СВС литых материалов в системе Mo–Al–C

В. А. Горшков, П. А. Милосердов, Д. Ю. Ковалев,
О. Д. Боярченко

Институт структурной макрокинетики и проблем материаловедения им. А.Г. Мержанова РАН
Россия, 142432, Московская обл., г. Черноголовка, ул. Академика Осипьяна, 8

gorsh@ism.ac.ru

Аннотация. Материалы на основе соединений молибдена с алюминием и углеродом обладают большим потенциалом для использования в условиях интенсивного износа при повышенных температурах. В настоящей работе представлены экспериментальные результаты самораспространяющегося высокотемпературного синтеза (СВС) соединений в системе Mo–Al–C. При совмещении двух процессов – СВС из элементов и СВС-металлургии – получены литые материалы, содержащие фазы Mo_3Al_2C, Mo_2C, Mo_3Al и Mo_3Al_8. В экспериментах использовали смеси с составами, рассчитанными согласно соотношению $(1 - \alpha)(3MoO_3–8Al–C)/\alpha(3Mo–2Al–C)$, где значение α меняли в интервале от 0 до 1. Синтез проводили в лабораторном реакторе объемом 3 л при начальном давлении аргона 5 МПа. Масса исходных смесей во всех экспериментах составляла 20 г. Процесс горения инициировали спиралью из молибденовой проволоки диаметром 0,5 мм путем подачи на нее напряжения 28 В. Полученные конечные продукты исследованы методами рентгенофазового и локального микроструктурного анализов. Установлено существенное влияние соотношения исходных реагентов на параметры синтеза, фазовый состав и микроструктуру целевых продуктов. Введение в высокоэкзотермическую смесь $3MoO_3$–8Al–C инертной «холодной» смеси 3Mo–2Al–C приводит к увеличению содержания карбидных фаз в слитках. Показана возможность получения литых материалов на основе тройной фазы Mo_3Al_2C, максимальное содержание которой составляет 87 мас. %, при количестве «холодной» смеси в шихте, соответствующей $\alpha = 0{,}4$. Присутствие в конечных продуктах вторичных фаз карбида молибдена (Mo_2C) и алюминидов молибдена (Mo_3Al_8, Mo_3Al) обусловлено изменением состава исходной смеси вследствие выброса компонентов при горении и недостаточным временем существования расплава, формирующегося в волне горения.

Ключевые слова: самораспространяющийся высокотемпературный синтез, система Mo–Al–C, микроструктура, фазовый состав

Для цитирования: Горшков В.А., Милосердов П.А., Ковалев Д.Ю., Боярченко О.Д. СВС литых материалов в системе Mo–Al–C. *Известия вузов. Порошковая металлургия и функциональные покрытия*. 2023;17(1):40–48. https://doi.org/10.17073/1997-308X-2023-1-39-48

Introduction

There are several binary compounds in Mo–Al system – $MoAl_3$, Mo_3Al_8, MoAl, and Mo_3Al [1]. These compounds, given their high melting points and mechanical properties, are promising materials for use under high temperature and intense wear conditions [2–4]. In Al–C system, the aluminum carbide phase Al_4C_3 is stable. Al_4C_3 particles finely dispersed in the aluminum matrix reduce the creep tendency of the material, especially in combination with silicon carbide particles. Aluminum carbide can be used as an abrasive material in high-speed cutting tools [5; 6]. In the Mo–C system, molybdenum and carbon form carbides Mo_2C and MoC_{1-x}. Among these, molybdenum carbide Mo_2C has the most widespread use in practice. It is used as a catalyst in hydrodesulfurization reactions, in dry reforming of methane, for the decomposition of hydrazine, and in regulators of small rocket engines [7–9]. Various methods are used for the synthesis of molybdenum carbide: carbothermal reduction of molybdenum (VI) oxide with graphite in an inert medium, electrochemical synthesis, melting with graphite, reduction of oxide using a methane–hydrogen mixture or other carbon sources [10–12].

Among the ternary molybdenum aluminum carbon compounds, the Mo_3Al_2C compound, a superconductor with a transition temperature of ~9 K, is of greatest interest. In the studies [13–16], this compound was obtained by the arc and high-frequency melting at high pressures (up to 10 GPa). Its transport, magnetic, and thermodynamic properties were investigated. The bulk modulus of elasticity is estimated at 221 GPa. Known methods for obtaining Mo_3Al_2C are inefficient and energy-intensive. A one-stage method – self-propagating high-temperature synthesis (SHS) – is a promising method for obtaining such compounds. It requires practically no electricity, exhibits high capacity and is environmentally friendly [17; 18].

The SHS method allowed to obtain a large number of binary and ternary element compounds [19–22]. One of the technological trends of application of self-propagating high-temperature synthesis is SHS-metallurgy, which allows to obtain “cast” materials by the complete melting of components in a combustion wave. A specific feature of the process is the use of mixtures consisting of metal oxides, a reducing metal (Al), and carbon. At a certain ratio of reagents, the combustion temperature exceeds the melting point of the initial reagents and final products. As a result, the product during synthesis is formed in the liquid state. Under the action of gravity, the heavy metal-like and light oxide phases of the formed products are separated. Cast materials based on binary and ternary compounds (MAX phases) in the systems: Cr–Al–C [23–25], Nb–Al–C [26; 27], and V–Al–C [28] obtained by SHS-metallurgy are of great interest. The mentioned studies demonstrate that the main synthesis parameter that determines the composition of the final products is the existence time of the melt, which depends on the combustion temperature of the initial mixture. To date, the authors of this paper have not identified any studies on the production of cast materials in the Mo–Al–C system by the SHS method.

The purpose of this paper was to study the possibility of obtaining cast products within the Mo–Al–C system by combining the methods of SHS from elements and SHS-metallurgy.

Materials and methods

Powders of MoO_3 (“Ch”, purity 99.9 %), Al (ASD-1, purity 99.2 %, particle size $d < 30$ μm), Mo (PM-M, 99.9 %, $d < 10$ μm), and graphite (PG, 99.2 %, $d < 400$ μm) were used as initial reagents. In the experiments, stoichiometric mixtures were used as base mixtures; their composition was calculated from a combination of two chemical reactions:

$$3MoO_3 + 8Al + C = Mo_3Al_2C + 3Al_2O_3, \qquad (I)$$

$$3Mo + 2Al + C = Mo_3Al_2C. \qquad (II)$$

The mass ratio of the mixtures $\alpha = \frac{M_{II}}{M_I}$ varied in the range from 0 to 1, where M_I and M_{II} are the masses of the mixtures calculated from reactions (I) and (II), respectively.

The experiments revealed that the combustion of the mixture, the composition of which was calculated according to reaction (I), is characterized by a high rate and a strong ejection of reagents and synthesis products from the reaction vessel. The mixture, the composition of which was calculated according to reaction (II), does not burn and, when added to the first mixture, behaves as a “reactive” inert component. The ratios of the initial compounds in reactions (I) and (II) remained constant in all experiments.

Before mixing, the powders were dried for 3 h at a temperature of 60 °C. The charge was prepared by manually stirring it in a porcelain mortar. The bulk density reaction mixture was placed in a 20 mm in diameter and 50 mm high quartz mold (Fig. 1, *a*). The weight of the initial mixtures in all experiments was 20 g. The syntheses were carried out in a 3 L reactor (Fig. 1, *b*) in an argon atmosphere at an initial pressure of 5 MPa according to the procedure described in work [23]. The reaction was initiated with a 0.5 mm diameter molybdenum wire coil. The combustion process was recorded using a video recorder. The combustion rate was calculated from the process video by measuring the time of passage of the combustion wave along the height of the sample. The parameters of synthesis were determined from the following values:

$\eta_1 = \frac{M_{ing}}{M_0}$ – the ratio of the product yield in the ingot and the weight of the mixture;

$\eta_2 = \frac{M_{ing}}{M_{ing}^{calc}}$ – the completeness of the reaction, the ration of the product yield in the ingot relative and its calculated value;

$\eta_3 = \frac{M_0 - M_k}{M_0}$ – mass loss during combustion due to the ejection of components from the reaction vessel,

where M_{ing} – the weight of the target product (ingot), M_{ing}^{calc} – the calculated weight of the ingot, M_0 – the mass of the initial mixture, M_k – the total mass of products after burning.

The end products of the synthesis were studied using *X*-ray diffraction (XRD) and microstructural analysis. The methods for studying the obtained products are described in more detail in the authors' previous works [25].

Results and Discussion

The samples after synthesis consist of two ingots that are easily separated mechanically. The material in the upper part of the sample, according to the XRD results, is mainly an α-Al_2O_3 phase. At the bottom, an ingot (target product) with a characteristic metallic sheen is formed (Fig. 1, *c*). The formation of an ingot

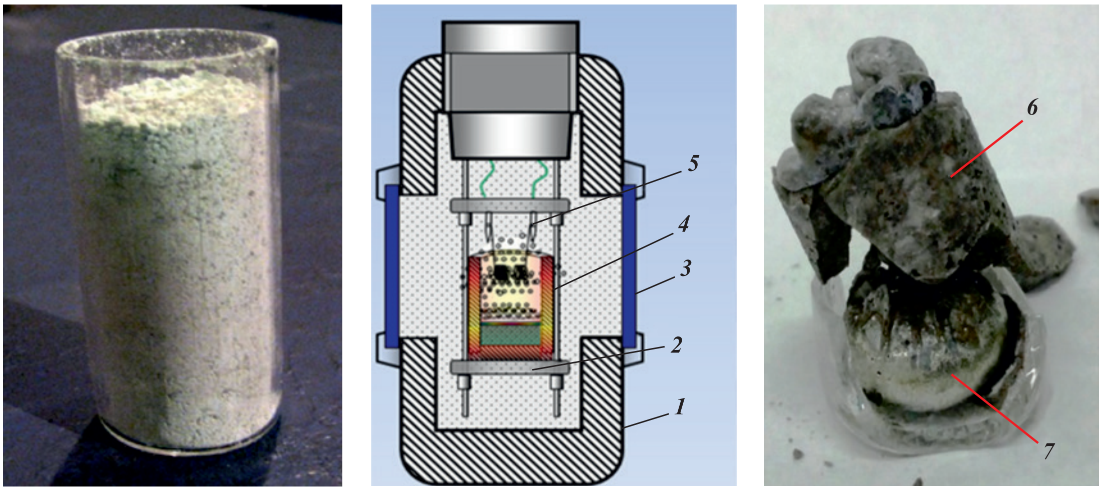

a *b* *c*

Fig. 1. Quartz crucible with a charge (***a***), reactor diagram (***b***), and final products (***c***)
1 – body, ***2*** – substrate, ***3*** – inspection window, ***4*** – charge, ***5*** – initiating coil, ***6*** – oxide layer, ***7*** – “metal” ingot

Рис. 1. Кварцевый тигель с шихтой (***a***), схема реактора (***b***) и конечные продукты (***c***)
1 – корпус, ***2*** – подложка, ***3*** – смотровое окно, ***4*** – шихта, ***5*** – инициирующая спираль, ***6*** – оксидный слой, ***7*** – «металлический» слиток

indicates that in the combustion wave a liquid phase was formed, i.e. the synthesis temperature is higher than the melting temperature of the initial components and the resulting products. Different specific masses of the final products lead to their separation due to gravity – the heavy "metal" phase settles at the bottom of the crucible, whereas the light oxide phase forms at the top.

The values of the combustion rate of the initial mixtures and the pressure increase in the reactor depending on the value of α are shown in Fig. 2, *a*. As α increases, these parameters decrease. When a "cold" mixture, the composition of which is determined from reaction (II), is added to a highly exothermic mixture, the composition of which is determined from reaction (I), part of the heat released as a result of a reaction (I) is spent on its melting, which leads to a decrease in the combustion rate and pressure increase in the reactor. Figure 2, *b* shows the dependences of the reaction completeness (η_2), product yield (η_1), and spread of combustion products (η_3) on α. The parameters η_1 and η_2 increase in the range of α from 0 to 0.4, then there is a gradual decrease. The values of η_3 decrease monotonically over the entire range of α.

The maximum product yield (η_1 = 67 %, η_2 = 93 %) is observed at α = 0.4 (Fig. 2, *b*). Yield is affected by two competing factors: reagent spread and combustion temperature. An increase in the amount of the "cold" mixture, on the one hand, reduces the ejection of reagents from the vessel and, accordingly, increases η_1, and, on the other hand, it reduces the combustion temperature, which leads to a decrease in η_2 due to a reduction in the time spent by the product in the liquid state, where oxide and "metal" phases spatially separate. *X*-ray phase analysis of the products (Figs. 3–5) obtained by combustion of mixtures with different α showed that as a result of synthesis, a multiphase material is formed, which includes Mo_3Al_2C, Mo_2C, Mo_3Al, and Mo_3Al_8. The quantitative ratio of the phases depends on the composition of the initial charge (see Table).

The combustion of mixtures of compositions *1* and *2* is non-stationary with a non-linear front and a considerable ejection of material from the crucible. *X*-ray phase analysis of the obtained products (see Fig. 3) revealed that as a result of synthesis, materials with a high content of molybdenum aluminides (Mo_3Al and Mo_3Al_8), more than 65 %, are formed, while the total content of carbide phases (Mo_3Al_2C and Mo_2) does not exceed 35 %. The low content of the latter is apparently associated with a deficit of carbon due to its ejection from the crucible in the form of particles or gaseous oxides. In the combustion wave, the mixture of initial reagents undergoes a number of physical and chemical

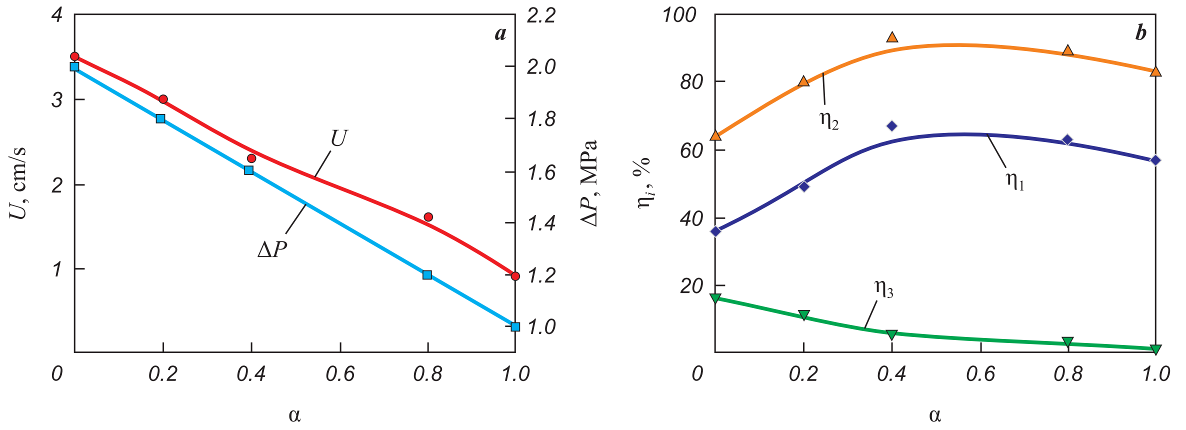

Fig. 2. Influence of α on the combustion rate and pressure increase in the reactor (***a***) and on the synthesis parameters (***b***)

Рис. 2. Влияние показателя α на скорость горения и прирост давления в реакторе (***a***), а также на параметры синтеза (***b***)

Phase composition of final products (wt. %)

Фазовый состав конечных продуктов (мас. %)

Composition No.	The proportion of mixture II, wt. %	α	Mo_3Al_2C ($P4_132$)	Mo_3Al ($Pm3n$)	Mo_3Al_8 ($C2/m$)	Mo_2C ($Pbnc$)
1	0	0	24.3	57.3	9.3	9.1
2	16.7	0.2	32.0	39.5	6.1	22.0
3	28.6	0.4	87.0	5.1	2.3	5.4
4	44.4	0.8	69.0	0.9	13.6	16.9
5	50.0	1.0	77.7	1.9	3.1	19.0

transformations. In the heating zone, aluminum and molybdenum oxide melt, forming a liquid-phase medium with distributed carbon particles. In the zone of chemical transformation, aluminum and carbon interact with molybdenum oxide:

$$MoO_3 + 2Al \rightarrow Mo + Al_2O_3, \qquad \text{(III)}$$

$$MoO_3 + xC \rightarrow MoC_x + CO(CO_2)\uparrow. \qquad \text{(IV)}$$

As a result, part of the carbon escapes from the reaction zone in the form of a gas, causing its deficiency in the system. The higher the combustion temperature of the mixture, the greater the likelihood of carbon participation in the redox reaction (IV). The material obtained as a result of the combustion of mixture *1* contains phases of Mo_3Al–Mo_3Al_8 intermetallic compounds forming an eutectoid, as well as Mo_3Al_2C and Mo_2C (see Fig. 3).

The introduction of a "cold" mixture into the charge leads to an increase of the content of carbide phases in the product while the proportion of molybdenum aluminides decreases (see table). The maximum content (87 %) of the ternary compound Mo_3Al_2C in the material was obtained at α = 0.4 (see Fig. 4).

The phase composition of the combustion products of mixture *3* is practically equilibrium and is in the three-phase region Mo_3Al_2C–Mo_2C–Mo_3Al. An increase

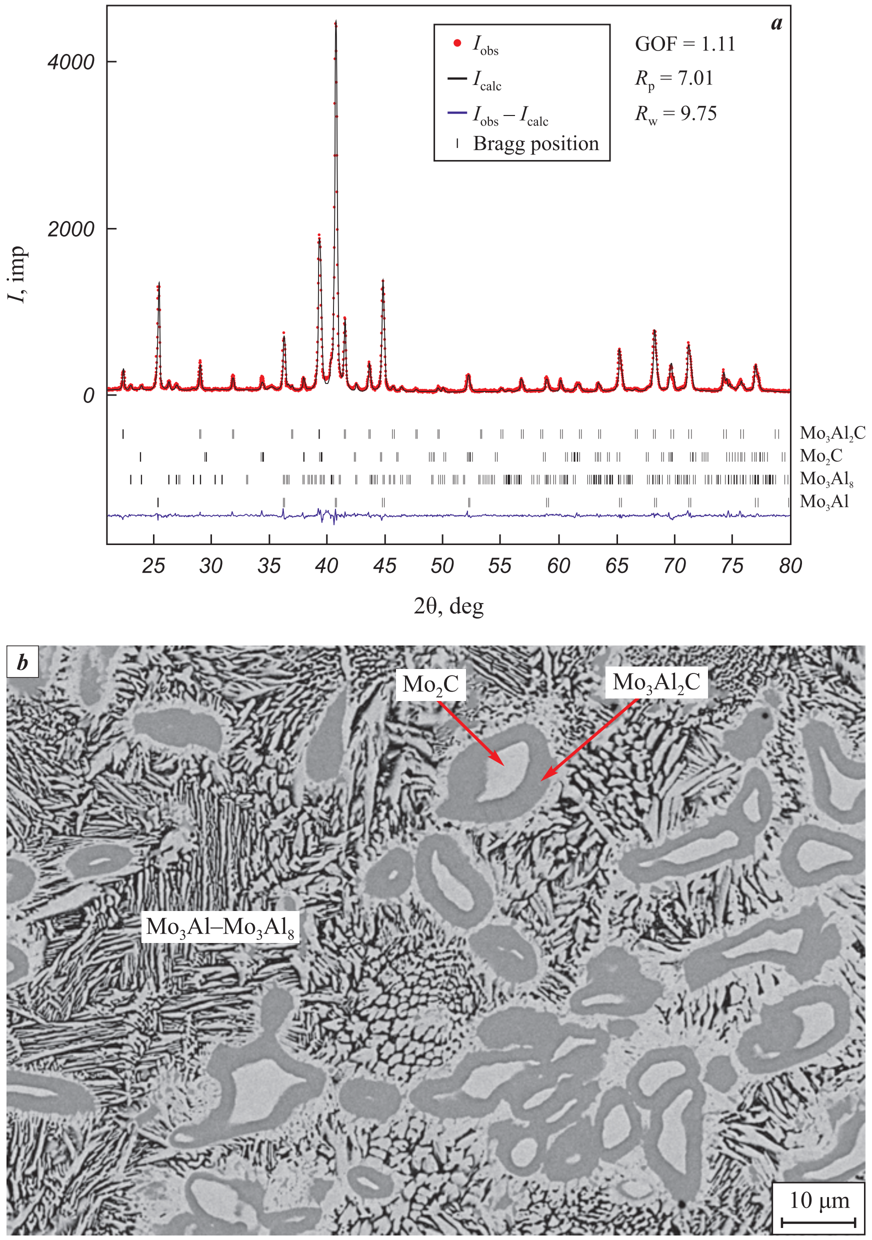

Fig. 3. Diffraction pattern (***a***) and microstructure (***b***) of the combustion product of mixture *1*

Рис. 3. Дифрактограмма (***a***) и микроструктура (***b***) продукта горения смеси *1* of the "cold" mixture content in the charge over the variation range $\alpha = 0.8{\div}1.0$ leads to an increase in the content of Mo_2C in the product while reducing the content of Mo_3Al_2C and molybdenum aluminides (see Table and Fig. 5).

The studies show that when a "cold" mixture is added to the charge, the combustion rate, pressure increase, and mass loss (η_3) decrease over the entire range of α (from 0 to 1.0). At the same time, in the range of $\alpha = 0{\div}0.4$, there is an increase in the target product yield into an ingot, whereas at $\alpha > 0.4$, there is a decrease. The target product yield into the ingot is affected by two competing factors: the content in the charge of the mixture (II), consisting of the target elements (Mo, Al, C) passing into the ingot as compounds, and the combustion temperature. With an increase in the amount of the "cold" mixture, on the one hand, the proportion of elements of the target phase in the charge increases and, accordingly, η_1 and η_2 increase, and, on the other hand, the combustion temperature decreases, which leads to a decrease in η_1 and η_2 due to a decrease in the residence time of the product in a liquid state, when there is a spatial separation of the oxide and "metal" phases. The influence of the first factor prevails at $\alpha = 0{\div}0.4$, whereas at $\alpha > 0.4$, prevails the influence of the second factor.

A single-phase product containing only Mo_3Al_2C in accordance with reactions (I) and (II) was not obtained due to several reasons. Obviously, the above scheme of reactions, used for the calculation of the equilibrium

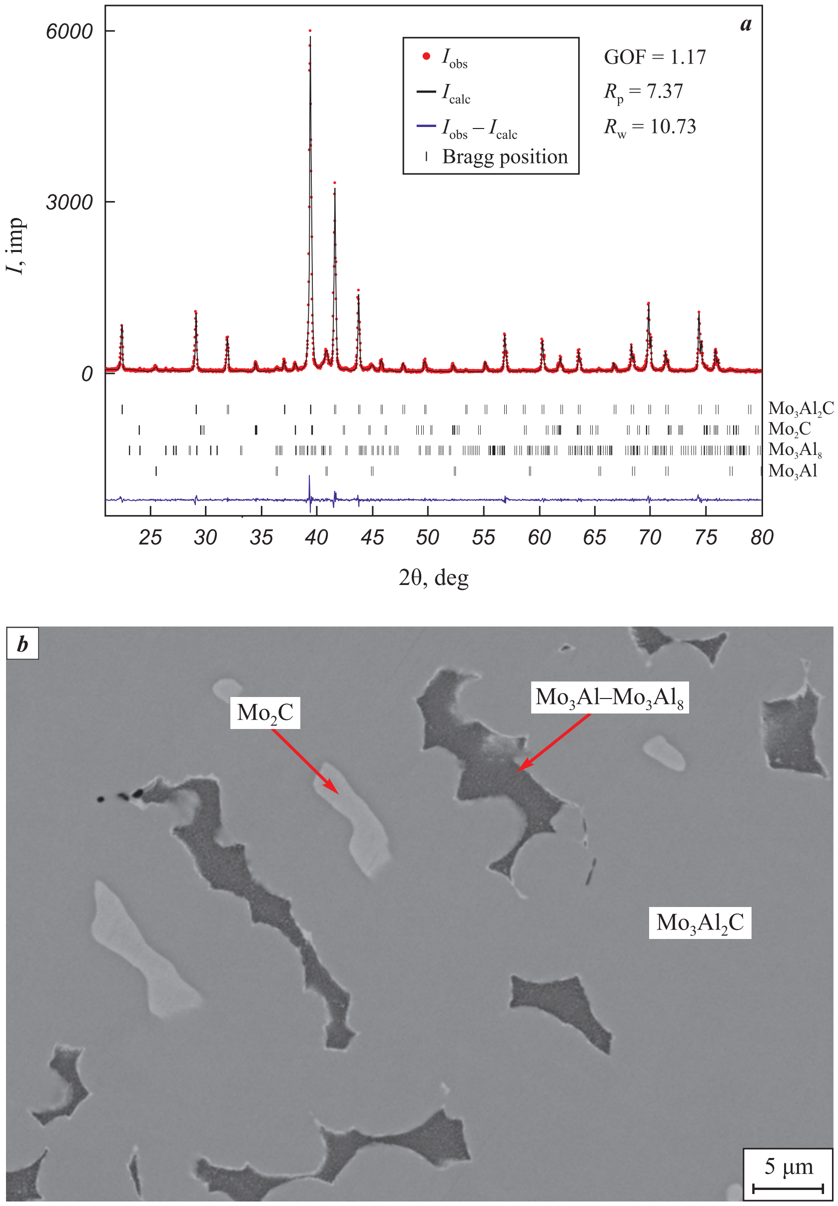

Fig. 4. Diffraction pattern (***a***) and microstructure (***b***) of the combustion product of a mixture *3*

Рис. 4. Дифрактограмма (***a***) и микроструктура (***b***) продукта горения смеси *3*

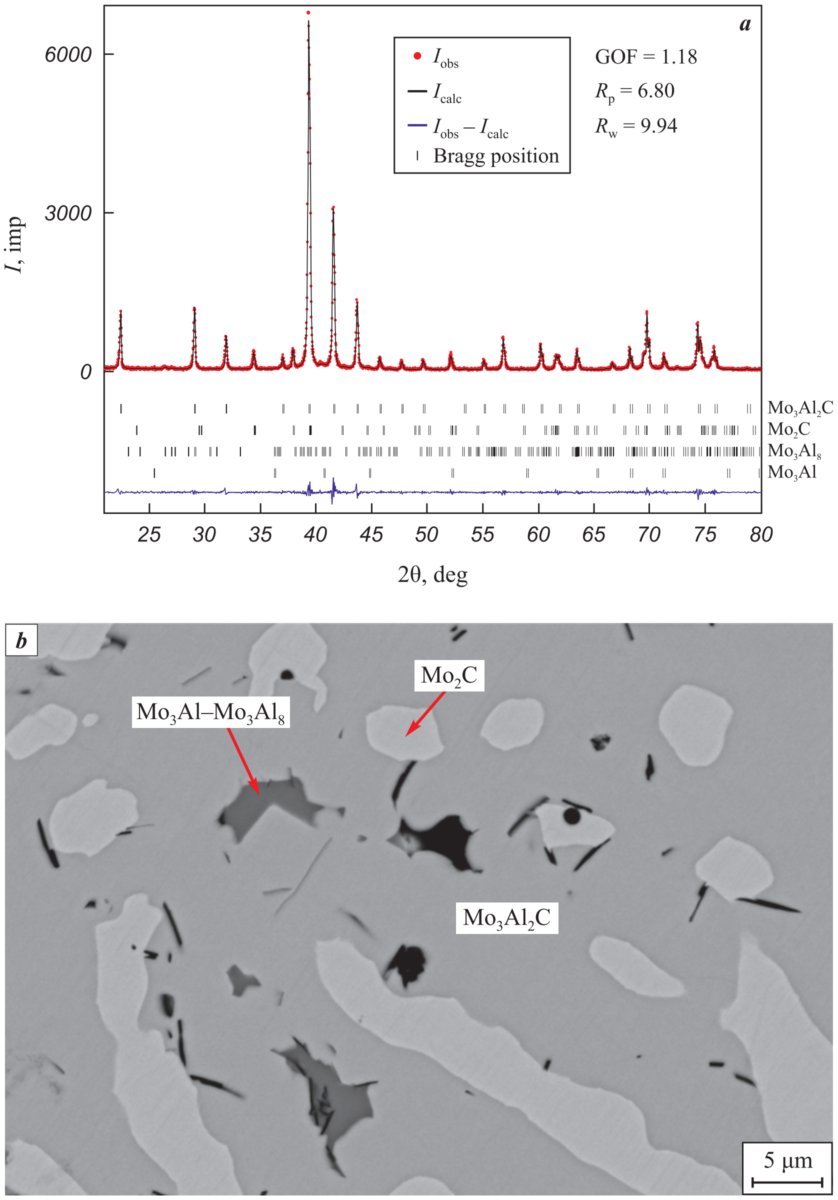

Fig. 5. Diffraction pattern (***a***) and microstructure (***b***) of the combustion product of mixture *5*

Рис. 5. Дифрактограмма (***a***) и микроструктура (***b***) продукта горения смеси *5*

composition of the target ternary phase Mo_3Al_2C, does not reflect all the interactions actually occurring in the multiphase system during SHS. *X*-ray diffraction phase analysis of the synthesized material showed that its phase composition differs from the calculated one. This indicates that the processes occurring in the liquid phase formed in the combustion wave and during its rapid crystallization lead to the formation of a nonequilibrium composition of the product. In addition, the combustion process is accompanied by the ejection of components as a result of the reaction (IV). It is quite likely that the resulting material is depleted in both carbon and aluminium. This is indirectly confirmed by the phase composition of mixture *5*, which is practically in the two-phase region $Mo_3Al_2C–Mo_2C$.

The analysis of microstructural analysis data suggests the following mechanism of phase formation of the final product. The phase composition of the ingot is formed as a result of a series of phase transformations. First, refractory Mo_2C carbide grains crystallize at a temperature of about 2500 °C. As a result, a Mo–Al melt is formed, which surrounds the Mo_2C grains. Then, during cooling in the temperature range of 2500–1720 °C, Al from the melt and Mo_2C interact, which leads to the formation of a carbide grain of the Mo_3Al_2C phase on their surface in a ring pattern (see Fig. 3). The growth of the layer is caused by the diffusion of Al from the Mo–Al melt through the Mo_3Al_2C layer into the Mo_2C grain. At temperatures below 1720 °C, the intergranular melt crystallizes with the formation of

Mo_3Al and MoAl. Then, at a temperature of 1467 °C, the MoAl phase undergoes the eutectoid transformation MoAl → Mo_3Al_8 + Mo_3Al [1]. Thus, the formation of a multiphase cast material is explained by the multistage nature of its formation and the rapid cooling of the melt.

Conclusion

Cast materials containing the phases Mo_3Al_2C, Mo_2C, Mo_3Al, and Mo_3Al_8 were obtained by the method of self-propagating high-temperature synthesis, combining two modes of the process – SHS from elemental powders and SHS-metallurgy. A significant effect of the ratio of reagents in the initial mixtures on the parameters of the combustion process, microstructure, and phase composition of the products was found. Introduction into the high-exothermic mixture $3MoO_3$–8Al–C inert “cold” mixture 3Mo–2Al–C leads to an increase in the content of carbide phases in the ingots. The maximum content (~87 wt. %) of the ternary phase Mo_3Al_2C was obtained at $\alpha = 0.4$. The presence of carbide Mo_2C and molybdenum aluminides Mo_3Al_8, and Mo_3Al in the final products is due to a change in the stoichiometric composition of the initial charge caused by the ejection of components during the combustion and insufficient existence time of the melt, which leads to the formation of a non-equilibrium composition of the product.

References / Список литературы

1. State diagrams of binary metallic systems: Handbook. Vol. 1. Ed. N.P. Lyakishev. Moscow: Mashinostroenie, 1996. 992 p. (In Russ.).

   Диаграммы состояния двойных металлических систем: Справочник. Т. 1. Под ред. Н.П. Лякишева. М.: Машиностроение, 1996. 992 с.
2. Saunders N., Thermotech Ltd. The Al–Mo system (aluminum–molybdenum). *Journal of Phase Equilibria*. 1997;18(4):370–378.
   https://doi.org/10.1007/s11669-997-0063-1
3. Cupid D.M., Fabrichnaya O., Ebrahimi F., Seifert H.J. Thermodynamic assessment of the Al–Mo system and of the Ti–Al–Mo system from 0 to 20 at.% Ti. *Intermetallics*. 2010;18(6):1185–1196.
   https://doi.org/10.1016/j.intermet.2010.03.010
4. Kriegel M.J., Walnsch A., Fabrichnaya O., Pavlyuchkov D., Klemm V., Freudenberger J., Rafaja D., Leineweber A. High-temperature phase equilibria with the bcc-type β (AlMo) phase in the binary Al–Mo system. *Intermetallics*. 2017;83:29–37.
   https://doi.org/10.1016/j.intermet.2016.12.004
5. Zhu S.J., Peng L.M., Zhou Q., Ma Z.Y., Kuchařová K., Čadek J. Creep behaviour of aluminum strengthened by fine aluminum carbide particles and reinforced by silicon carbide particulates DS Al–SiC/Al_4C_3 composites. *Materials Science and Engineering: A*. 1999;268(1–2):236–245.
   https://doi.org/10.1016/S0921-5093(98)01119-8
6. Gmelins Handbuch Der Anorganischen Chemie. 8th ed. Ed. by the German Chemical Society. System-Nummer 35: Aluminium. Teil A-Lieferung 1. Pp. iv + 284. Berlin: Verlag Chemie, 1934.
   https://doi.org/10.1002/jctb.5000541621
7. Wang X.-H., Hao H.-L., Zhang M.-H., Li W., Tao K.-Y. Synthesis and characterization of molybdenum carbides using propane as carbon source. *Journal of Solid State Chemistry*. 2006;179(2):538–543.
   https://doi.org/doi:10.1016/j.jssc.2005.11.009
8. Manoli J.-M., Da Costa P., Brun M., Vrinat M., Maugé F., Potvin C. Hydrodesulfurization of 4,6-dimethyldibenzothiophene over promoted (Ni,P) alumina-supported molybdenum carbide catalysts: activity and characterization of active sites. *Journal of Catalysis*. 2004;221(2):365–377.
   https://doi.org/10.1016/j.jcat.2003.08.011
9. Zeng L., Zhang L., Li W., Zhao S., Lei J., Zhou Z. Molybdenum carbide as anodic catalyst for microbial fuel cell based on Klebsiella pneumoniae. *Biosensors and Bioelectronics*. 2010;25(12):2696–2700.
   https://doi.org/10.1016/j.bios.2010.05.002
10. Cho S.J., Lee J., Lee Y.S., Kim D.P. Characterization of iridium catalyst for decomposition of hydrazine hydrate for hydrogen generation. *Catalysis Letters*. 2006;109(3):181–186.
    https://doi.org/10.1007/s10562-006-0081-3
11. Anselmi-Tamburini U., Maglia F., Spinolo G., Munir Z.A. Combustion synthesis: An effective tool for the synthesis of advanced materials. *Chimica & Industria*. 2000;82(10):1–10.
12. Nguyen T.H., Nguyen T.V., Lee Y.J., Safinski T., Adesina A.A. Structural evolution of alumina supported Mo–W carbide nanoparticles synthesized by precipitation from homogeneous solution. *Materials Research Bulletin*. 2005;40(1):149–157.
    https://doi.org/10.1016/j.materresbull.2004.09.007
13. Zhu Q., Chen Q., Yang X., Ke D. A new method for the synthesis of molybdenum carbide. *Materials Letters*. 2007;61(29):5173–5174.
    https://doi.org/10.1016/j.matlet.2007.04.056
14. Karki A.B., Xiong Y.M., Vekhter I., Browne D., Adams P.W., Young D.P., Thomas K.R., Chan J.Y., Kim H., Prozorov R. Structure and physical properties of the noncentrosymmetric superconductor Mo_3Al_2C. *Physical Review B*. 2010;82(6):064512.
    https://doi.org/10.1103/PhysRevB.82.064512
15. Bonalde I., Kim H., Prozorov R., Rojas C., Rogl P., Bauer E. Evidence for conventional superconducting behavior in noncentrosymmetric Mo_3Al_2C. *Physical Review B*. 2011;84(13):134506.
    https://doi.org/10.1103/PhysRevB.84.134506
16. Sekine C., Sai U., Hayashi J., Kawamura Y., Bauer E. High-pressure synthesis and bulk modulus of non-centrosymmetric superconductor Mo_3Al_2C. *Journal of Physics: Conference Series*. 2017;950(4):042028.
    https://doi.org/10.1088/1742-6596/950/4/042028
17. Merzhanov A.G. SHS on the pathway to industrialization. *International Journal of Self-Propagating High-Temperature Synthesis*. 2001;10(2):237–256.
18. Merzhanov A.G. The chemistry of self-propagating high-temperature synthesis. *Journal of Materials Chemistry*.

2004;14(12):1779–1786.
https://doi.org/10.1039/B401358C

19. Levashov E.A., Mukasyan A.S., Rogachev A.S., Shtansky D.V. Self-propagating high-temperature synthesis of advanced materials and coatings. *International Materials Reviews*. 2017;62(4):203–239.
https://doi.org/10.1080/09506608.2016.1243291

20. Łopacinski M., Puszynski J., Lis J. Synthesis of ternary titanium aluminum carbides using self-propagating high-temperature synthesis technique. *Journal of the American Ceramic Society*. 2004;84(12):3051–3053.
https://doi.org/10.1111/j.1151-2916.2001.tb01138.x

21. Zhu C.-C., Zhu J., Wu H., Lin H. Synthesis of Ti_3AlC_2 by SHS and thermodynamic calculation based on first principles. *Rare Metals*. 2015;34(2):107–110.
https://doi.org/10.1007/s12598-013-0174-2

22. Konovalikhin S.V., Kovalev D.Yu., Sytschev A.E., Vadchenko S.G., Shchukin A.S. Formation of nanolaminate structures in the Ti–Si–C system: A crystallochemical study. *International Journal of Self-Propagating High-Temperature Synthesis*. 2014;23(4):217–221.
https://doi.org/10.3103/S1061386214040049

23. Gorshkov V.A., Miloserdov P.A., Luginina M.A., Sachkova N.V., Belikova A.F. High-temperature synthesis of a cast material with a maximum content of the MAX phase Cr_2AlC. *Inorganic Materials*. 2017;53(3):271–277.
https://doi.org/10.1134/S0020168517030062

Горшков В.А., Милосердов П.А., Лугинина М.А., Сачкова Н.В., Беликова А.Ф. Высокотемпературный синтез литого материала с максимальным содержанием МАХ-фазы Cr_2AlC. *Неорганические материалы*. 2017;53(3):260–266.
https://doi.org/10.7868/S0002337X1703006X

24. Gorshkov V.A., Miloserdov P.A., Sachkova N.V., Luginina M.A., Yukhvid V.I. SHS metallurgy of Cr_2AlC MAX phase-based cast materials. *Russian Journal of Non-Ferrous Metals*. 2018;59(5):570–575.
https://doi.org/0.3103/S106782121805005X

Горшков В.А., Милосердов П.А., Сачкова Н.В., Лугинина М.А., Юхвид В.И. СВС-металлургия литых материалов на основе МАХ-фазы Cr_2AlC. *Известия вузов. Порошковая металлургия и функциональные покрытия*. 2017;(2):47–54.
https://doi.org/10.17073/1997-308X-2017-2-47-54

25. Gorshkov V.A., Miloserdov P.A., Khomenko N.Yu., Sachkova N.V. Production of cast materials based on the Cr_2AlC MAX phase by SHS metallurgy using coupled chemical reactions. *Russian Journal of Non-Ferrous Metals*. 2020;61(3):362–367.
https://doi.org/10.3103/S1067821220030086

Горшков В.А., Милосердов П.А., Хоменко Н.Ю., Сачкова Н.В. Получение литых материалов на основе МАХ-фазы Cr_2AlC методом СВС-металлургии с использованием химически сопряженных реакций. *Известия вузов. Порошковая металлургия и функциональные покрытия*. 2019;(4):14–20.
https://doi.org/10.17073/1997-308X-2019-4-14-20

26. Miloserdov P.A., Gorshkov V.A., Kovalev I.D., Kovalev D.Yu. High-temperature synthesis of cast materials based on Nb_2AlC MAX phase. *Ceramics International*. 2019;45(2, Part A):2689–2691.
https://doi.org/10.1016/j.ceramint.2018.10.198

27. Kovalev I.D., Miloserdov P.A., Gorshkov V.A., Kovalev D.Yu. Synthesis of Nb_2AlC MAX phase by SHS metallurgy. *Russian Journal of Non-Ferrous Metals*. 2020;61(1):126–131.
https://doi.org/10.3103/S1067821220010083

Ковалев И.Д., Милосердов П.А., Горшков В.А., Ковалев Д.Ю. Синтез МАХ-фазы Nb_2AlC методом СВС-металлургии. *Известия вузов. Порошковая металлургия и функциональные покрытия*. 2019;(2):42–48.
https://doi.org/10.17073/1997-308X-2019-2-42-48

28. Gorshkov V.A., Karpov A.V., Kovalev D.Yu., Sychev A.E. Synthesis, structure and properties of material based on V_2AlC MAX phase. *Physics of Metals and Metallography*. 2020;121(8)765–771.
https://doi.org/10.1134/s0031918x20080037

Горшков В.А., Карпов А.В., Ковалев Д.Ю., Сычев А.Е. Синтез, структура и свойства материала на основе МАХ-фазы V_2AlC. *Физика металлов и металловедение*. 2020;121(8):842–848.
https://doi.org/10.31857/S0015323020080033

Information about the Authors

Vladimir A. Gorshkov – Dr. Sci. (Eng.), Leading Researcher of the Laboratory of SHS melts and cast materials of Merzhanov Institute of Structural Macrokinetics and Materials Science of the Russian Academy of Sciences (ISMAN)
ORCID: 0000-0001-8845-4717
E-mail: gorsh@ism.ac.ru

Pavel A. Miloserdov – Cand. Sci. (Eng.), Senior Researcher of the Laboratory of SHS melts and cast materials of ISMAN
ORCID: 0000-0002-2587-0067
E-mail: yu_group@ism.ac.ru

Dmitrii Yu. Kovalev – D.Yu. – Dr. Sci. (Phys.-Math.), Head of the Laboratory of *X*-ray investigation of ISMAN
ORCID: 0000-0002-8285-5656
E-mail: kovalev@ism.ac.ru

Сведения об авторах

Владимир Алексеевич Горшков – д.т.н., вед. науч. сотрудник лаборатории «Жидкофазные СВС-процессы и литые материалы», Институт структурной макрокинетики и проблем материаловедения им. А.Г. Мержанова РАН (ИСМАН)
ORCID: 0000-0001-8845-4717
E-mail: gorsh@ism.ac.ru

Павел Александрович Милосердов – к.т.н., ст. науч. сотрудник лаборатории «Жидкофазные СВС-процессы и литые материалы», ИСМАН
ORCID: 0000-0002-2587-0067
E-mail: yu_group@ism.ac.ru

Дмитрий Юрьевич Ковалев – д.ф.-м.н., заведующий лабораторией рентгеноструктурных исследований, ИСМАН
ORCID: 0000-0002-8285-5656
E-mail: kovalev@ism.ac.ru

Ol'ga D. Boyarchenko – Cand. Sci. (Phys.-Math.), Researcher of the Laboratory of materials science of ISMAN
ORCID: 0000-0002-7543-7608
E-mail: olgaboyarchenko@gmail.com

Ольга Дмитриевна Боярченко – к.ф.-м.н., науч. сотрудник лаборатории физического материаловедения, ИСМАН
ORCID: 0000-0002-7543-7608
E-mail: olgaboyarchenko@gmail.com

Contribution of the Authors

V. A. Gorshkov – formation of the main concept, setting the goal and objectives of the study, conducting experiments, preparing the text, formulating conclusions.
P. A. Miloserdov – conducting the calculations, conducting experiments, processing research results, preparing the text of the article.

D. Yu. Kovalev – *X*-ray phase analysis, processing of research results.
O. D. Boyarchenko – microstructural analysis, processing of research results.

Вклад авторов

В. А. Горшков – формирование основной концепции, постановка цели и задачи исследования, проведение экспериментов, подготовка текста, формулировка выводов.
П. А. Милосердов – проведение расчетов, проведение экспериментов, обработка результатов исследований, подготовка текста статьи.
Д. Ю. Ковалев – проведение рентгенофазового анализа, обработка результатов исследований.
О.Д Боярченко – проведение микроструктурного анализа, обработка результатов исследований.

Received 03.08.2022
Revised 03.10.2022
Accepted 05.10.2022

Статья поступила 03.08.2022 г.
Доработана 03.10.2022 г.
Принята к публикации 05.10.2022 г.

Nanostructured Materials and Functional Coatings
Наноструктурированные материалы и функциональные покрытия

UDC 621.762

https://doi.org/10.17073/1997-308X-2023-1-49-62

Research article
Научная статья

Microstructure and phase composition of hard alloys produced from nanocrystalline powder mixture WC–6wt.%Co with C, Al and ZrC additives

S. V. Briakunov[1, 2], **A. S. Kurlov**[1]

[1] **Institute of Solid State Chemistry of the Ural Branch of the Russian Academy of Sciences**
91 Pervomaiskaya Str., Ekaterinburg 620990, Russian Federation
[2] **Ural Federal University named after the first President of Russia B. N. Yeltsin**
19 Mira Str., Ekaterinburg 620002, Russian Federation

kurlov@ihim.uran.ru

Abstract. A large specific surface area of WC nanopowder determines its high chemical activity and makes it very sensitive to various impurities, among which oxygen is most harmful and unavoidable. During heating, oxygen interacts with carbon of WC being removed in the form of CO/CO_2, which finally leads to the appearance of embrittling η-phases in the hard alloy, abnormal growth of WC grains, and formation of a porous microstructure. To prevent heavy decarburization of WC during vacuum sintering of hard alloy from a nanocrystalline powder mixture WC–6wt.%Co, in this work we compared three methods: addition of extra carbon to compensate for carbon loss as a result of decarburization; addition of Al to bind impurity oxygen into Al_2O_3 before it interacts with carbon of WC; and addition of ZrC to compensate for carbon loss and bind impurity oxygen into ZrO_2. Nanocrystalline powder mixtures based on WC–6 wt.%Co with and without additions of C, Al, and ZrC were prepared from microcrystalline powders of WC, Co, Al, ZrC, and carbon black by high-energy milling, then they were compacted in a cylindrical mold by uniaxial pressing at a pressure of ~460 MPa and sintered in graphite crucibles for 15 min at 1380 °C in vacuum of $\sim 10^{-2}$ Pa. The heating rate to the temperature of sintering was 10 °C/min. The initial powders, powder mixtures prepared therefrom, and sintered hard alloys were certified using *X*-ray diffraction, chemical analysis, scanning electron microscopy, BET adsorption method, helium pycnometry, and Vickers method. The studies performed showed that the average particle size in all the prepared powder mixtures does not exceed 100 nm, and the content of impurity oxygen in them varies from 3.3 to 4.3 wt.% depending on the additives. It was established that only a part of oxygen contained in the powder mixtures is in the chemisorbed state and takes part in the decarburization of WC during vacuum sintering. The Al additive is completely oxidized during milling of the powder mixture and transforms into nanocrystalline Al_2O_3, which only aggravates carbon loss during sintering and results in the formation of a multiphase and relatively porous microstructure of the hard alloy. On the contrary, using carbon and ZrC additives we managed to prevent the decarburization of WC during sintering of the hard alloy and to form a less porous microstructure in it. It was shown that the presence of ZrO_2 inclusions does not impede intensive growth of WC grains during sintering, but rather promotes it. Carbon deficit slightly suppresses intensive WC grain growth during sintering of hard alloy leading to the formation of η-phases and to an increase in the density and microhardness, but the presence of oxide inclusions Al_2O_3 and ZrO_2 in the microstructure reduces the values of these properties.

Keywords: tungsten carbide, aluminum, zirconium carbide, high-energy milling, nanocrystalline powder, vacuum sintering, decarburization, hard alloy, microstructure, microhardness

Acknowledgements: the study was carried out within the framework of the state assignment of the Institute of Solid State Chemistry of the Ural Branch of the Russian Academy of Sciences No. AAAA-A19-119031890029-7.
The authors kindly acknowledge the assistance of O.V. Makarova in the density measurements and of L.Yu. Buldakova and D.A.Danilov in the determination of carbon and oxygen content in powders.

For citation: Briakunov S.V., Kurlov A.S. Microstructure and phase composition of hard alloys produced from nanocrystalline powder mixture WC–6 wt.% Co with C, Al, and ZrC additives. *Powder Metallurgy and Functional Coatings*. 2023;17(1): 49–62. https://doi.org/10.17073/1997-308X-2023-1-49-62

Микроструктура и фазовый состав твердых сплавов, изготовленных из нанокристаллической порошковой смеси WC–6мас.%Co с добавками C, Al и ZrC

С. В. Брякунов[1, 2], **А. С. Курлов**[1]

[1] **Институт химии твердого тела Уральского отделения РАН**
Россия, 620990, г. Екатеринбург, ул. Первомайская, 91
[2] **Уральский федеральный университет им. первого Президента России Б.Н. Ельцина**
Россия, 620002, г. Екатеринбург, ул. Мира, 19

kurlov@ihim.uran.ru

Аннотация. Большая удельная поверхность нанопорошка WC обусловливает его высокую химическую активность и делает его очень чувствительным к различным примесям, среди которых кислород является наиболее вредной и неизбежной. При нагреве кислород взаимодействует с углеродом WC, удаляясь в виде CO/CO_2, что в конечном итоге приводит к образованию в твердом сплаве охрупчивающих η-фаз, аномальному росту зерен WC и формированию пористой микроструктуры. Для предотвращения сильного обезуглероживания WC при вакуумном спекании твердого сплава из нанокристаллической порошковой смеси WC–6мас.%Co в данной работе сравнивались три способа: добавление избыточного углерода для компенсации потерь в результате обезуглероживания; введение в порошковую смесь алюминия для связывания примесного кислорода в Al_2O_3 до взаимодействия его с углеродом WC; использование добавки ZrC для компенсации потери углерода и связывания примесного кислорода в ZrO_2. Нанокристаллические порошковые смеси на основе WC–6мас.%Co с добавками C, Al, ZrC и без них готовились из микрокристаллических порошков WC, Co, Al, ZrC и сажи с помощью высокоэнергетического размола, затем компактировались в цилиндрической пресс-форме путем одноосного прессования при давлении ~460 МПа и спекались в графитовых тиглях в течение 15 мин при температуре 1380 °C в вакууме $\sim 10^{-2}$ Па. Скорость нагрева до температуры спекания составляла 10 °C/мин. Аттестация исходных порошков, приготовленных из них порошковых смесей, а также спеченных твердых сплавов осуществлялась с помощью рентгеновской дифракции, химического анализа, сканирующей электронной микроскопии, адсорбционного метода БЭТ, гелиевой пикнометрии и метода Виккерса. Исследования показали, что средний размер частиц во всех приготовленных порошковых смесях не превышает 100 нм, а содержание примесного кислорода в них варьируется от 3,3 до 4,3 мас. % в зависимости от добавок. Установлено, что лишь часть содержащегося в порошковых смесях кислорода находится в хемосорбированном состоянии и принимает участие в обезуглероживании WC при вакуумном спекании. Добавка Al при размоле порошковой смеси полностью окисляется и превращается в нанокристаллический оксид Al_2O_3, что только усугубляет потерю углерода при спекании и приводит к формированию многофазной и относительно пористой микроструктуры твердого сплава. Наоборот, с помощью добавок углерода и ZrC удается предотвратить обезуглероживание WC при спекании твердого сплава и сформировать в нем наименее пористую микроструктуру. Показано, что наличие оксидных включений ZrO_2 не препятствует интенсивному росту зерен WC при спекании, а скорее, наоборот, способствует этому. Дефицит углерода немного сдерживает интенсивный рост зерен WC при спекании твердого сплава, приводя к образованию η-фаз и повышению плотности и микротвердости, но присутствие оксидных включений Al_2O_3 и ZrO_2 в микроструктуре снижает величины этих свойств.

Ключевые слова: карбид вольфрама, алюминий, карбид циркония, высокоэнергетический размол, нанокристаллический порошок, вакуумное спекание, обезуглероживание, твердый сплав, микроструктура, микротвердость

Благодарности: исследование выполнено в рамках государственного задания ИХТТ Уральского отделения РАН № АААА-А19-119031890029-7.

Авторы благодарны О.В. Макаровой за помощь в измерении плотности, а также Л.Ю. Булдаковой и Д.А. Данилову за помощь в определении содержания углерода и кислорода в порошках.

Для цитирования: Брякунов С.В., Курлов А.С. Микроструктура и фазовый состав твердых сплавов, изготовленных из нанокристаллической порошковой смеси WC–6мас.%Co с добавками C, Al и ZrC. *Известия вузов. Порошковая металлургия и функциональные покрытия*. 2023;17(1):49–62. https://doi.org/10.17073/1997-308X-2023-1-49-62

Introduction

Thanks to an outstanding combination of high hardness values and impact toughness, hard alloys, compared to other cutting materials (such as diamond or high speed steels), have a wide range of applications in many industries, e.g. as cutting tools (turning, milling, drilling tools) for metalworking, as part of the components of drill bits for well drilling, tunneling, and road pavement removal, as wear-resistant parts in drawing and stamping tools, etc. [1–3].

In the vast variety of available hard alloys, WC–Co system alloys are among the most common and required. The combination of the high hardness and strength of WC, which is maintained even at relatively high temperatures, with the ductility and high impact toughness of Co results in WC–Co alloys with high hardness, strength and wear resistance [4; 5]. Research into the physical, mechanical and performance properties of these alloys continues to this day. In the last three decades, the main efforts were aimed at developing various methods of obtaining nanocrystalline WC powders and mixtures based on them [6–10], as well as methods of their consolidation [11–20] for the production of hard alloys with a submicro- and nanocrystalline structure, which would enable significant improvement of their mechanical properties [21–23].

However, the transition from the use of microcrystalline to nanocrystalline carbide powders also exacerbates their contamination problem. The extremely large specific surface area of nanopowders determines their high chemical activity and makes them very sensitive to various impurities. The surface of carbide nanoparticles may contain adsorbed water and other impurities. Oxygen is the most harmful and unavoidable of these contaminants, its content usually greatly exceeding the total amount of all other impurities and determining the overall purity of the carbide nanopowder [24]. It was shown in [25; 26] that vacuum heating of nanocrystalline WC powders, regardless of their production method, is accompanied by decarburization of WC and leads to a change in their phase composition. When carbon is added to WC nanopowder, the latter retains its single-phase nature, but the strong growth of carbide particles is provoked, transforming the powder into a microcrystalline one. In the case of WC–Co hard alloys produced from nanopowders, decarburization during sintering caused by oxygen adsorbed on the surface of nanoparticles ultimately leads to the formation of embrittling η-phases in the alloy and abnormal growth of carbide grains [27–29].

The study of micro- and nanocrystalline TaC powders has shown that the content of adsorbed oxygen in them increases linearly with the specific surface area of the powder and that most of the oxygen in the powders is predominantly in the chemisorbed state, forming several monolayers of the Ta_2O_5 oxide phase on the particle surface [30]. An assessment of the possible loss of carbide carbon due to the desorption of chemisorbed oxygen in the form of CO showed that high-temperature sintering of nanocrystalline TaC powders, in contrast to microcrystalline ones, can be accompanied by their significant decarburization, which ultimately leads not only to a change in the composition (y) of TaC_y carbide, but also to a change in the phase composition of the entire powder, which was later confirmed experimentally [31]. Besides, the desorption of chemisorbed oxygen in the form of CO and CO_2 during sintering of dense compacts of carbide nanopowders results in the formation of a porous structure [32]. To avoid this, the impurity oxygen must be bound during sintering into strong, hard and refractory oxides that take the place of possible pores before the oxygen begins to interact with the carbon of the carbide. Candidates for this role may be Al or Zr, which have a higher affinity for oxygen compared to W and form the oxides Al_2O_3 and ZrO_2 that are well known as the basis of modern ceramic materials with high mechanical strength, hardness, wear resistance, refractoriness, chemical and corrosion resistance [33; 34].

As evidenced by numerous publications [35–38], the practice of modifying WC–Co hard alloys with Al_2O_3 or ZrO_2 nanoparticles to improve their physical and mechanical characteristics and performance has been in place for a long time. However, to form these particles during sintering, oxide nanoparticles, rather than pure metals, are added to WC-based nanocrystalline powder mixtures, as a rule. There are studies on the effect of Al additives in WC–Co powder mixtures, but they are usually microcrystalline powders with a low content of impurity oxygen; therefore, no Al_2O_3 is formed after sintering and only the presence of intermetallic Al–Co phases is detected [39].

The aim of this study is to find out whether it is possible to prevent strong decarburization of WC in a compacted WC–Co nanocrystalline powder mixture with the help of Al, ZrC, and carbon additives during conventional vacuum sintering and how these additives affect the microstructure and microhardness of the hard alloy.

Materials and Methods

To compensate for the loss of carbon and prevent strong decarburization of WC during vacuum sintering of a hard alloy, the results of using three additives were compared: carbon – to compensate for losses due to decarburization; aluminum – for binding impurity oxygen into solid and refractory oxide Al_2O_3 before its interaction with the carbon of WC; ZrC – to compensate for the loss of carbon and binding of impurity oxygen into refractory oxide ZrO_2.

The selected additives were introduced into the powder mixture in different amounts, due to the sequence of the experiments and the results obtained. The addition of Al was calculated based on the loss of carbon, which was determined from the change in the phase composition during the sintering of the WC nanopowder (without Co). The sample sintered from the WC nanopowder contained, along with WC, about 7.5 wt. %[1] W_2C, which corresponds to ~0.2 % carbon deficiency (loss) for the formation of single-phase WC. Assuming that the loss of carbon occurred only as a result of interaction with adsorbed oxygen with the formation of CO, at least 0.3 % of oxygen would be required to remove 0.2 % of carbon. To bind 0.3 % oxygen into Al_2O_3 oxide, a minimum of 0.4 % Al is required, taking into account that there is always an oxide film on the surface of Al particles the thickness of which in nanopowders obtained by milling is ~5 nm [40].

The carbon addition was calculated in a similar way, but by the change in the phase composition of the hard alloy made from the WC–6%Co nanocrystalline powder mixture. According to the phase composition of the sintered hard alloy (wt. %: 83.7 WC, 8.2 Co_3W_3C, 4.7 Co_6W_6C, 3.4 Co_3W), its carbon content does not exceed 5.3 %, while it should be at least 5.8 %. Thus, the addition of carbon to the WC–6%Co powder mixture to compensate for its loss was 0.5 %.

Likewise, the addition of ZrC was also calculated from the change in the phase composition of the hard alloy, but in this case, the possible presence of oxygen on the surface of ZrC nanoparticles after milling was taken into account. Therefore, the case of a sufficient amount of oxygen on the surface of carbide particles to be removed after interaction with the carbide carbon mainly in the form of CO_2 was considered, rather than in the form of CO, as was considered in the case with Al. A minimum of 1.3 % oxygen is required to bind 0.5 % carbon in CO_2. But to avoid the loss of carbon and completely bind this oxygen in ZrO_2, at least 4.2 % ZrC is required. Assuming that the interaction of impurity oxygen with carbide carbon can form not only CO_2, but also CO, 4.0 % of ZrC carbide was added to the WC–6%Co powder mixture before milling.

Nanocrystalline powder mixtures of WC–6%Co with and without additives were prepared using high-energy milling of microcrystalline WC powders ($D_{av} \approx 6$ μm, $C_{tot} = 6.15$ %, $C_{free} = 0.07$ %, $O_{tot} = 0.09$ %, Kirovgrad hard alloys plant (KZTS), JSC, Kirovgrad), Co ($D_{av} \approx 3$ μm, KZTS, JSC), Al ($D_{av} \approx 25$ μm, RUSAL, Krasnoyarsk), ZrC ($D_{av} \approx 4$ μm, $C_{tot} = 10.26$ %, $C_{free} = 1.72$ %, $O_{tot} = 1.40$ %, Donetsk Plant of Chemical Reagents, JSC (DZKhR), Donetsk) and carbon black (soot) grade T-900 ($D_{av} \approx 0.4$ μm, Russia).

Milling of microcrystalline powders taken in a given ratio was carried out using a "Pulverisette 7" planetary ball mill (Fritsch, Germany) using grinding balls and grinding jar lining made of WC–6%Co hard alloy. The same grinding mode was used to prepare all powder mixtures: the rotation speed of the grinding jar support disk was 600 rpm; the weight of the powder taken for grinding was 10 g; the weight of the grinding balls with a diameter of 3 mm ~100 g; grinding jar volume – 45 mL; the volume of isopropyl alcohol C_3H_8O (high purity, 99.9 %, Component-Reaktiv, Ltd, Moscow) added during milling was 10 mL. After milling, the powder mixtures were dried in the vacuum drying cabinet VDL 23 (Binder, Germany) at a pressure of $\sim 10^3$ Pa and a temperature of 85 °C.

The compaction of powder mixtures was carried out at room temperature in a steel cylindrical mold with a punch diameter of 7.45 mm using uniaxial pressing at a pressure of ~460 MPa. Sintering of compact samples placed in graphite crucibles was carried out in a high-temperature vacuum furnace LF-22-2000 (Centorr/Vacuum Industries, USA) for 15 min at $t = 1380$ °C in a vacuum of $\sim 10^{-2}$ Pa. The heating rate to the temperature of sintering was 10 °C/min.

After sintering, the samples were cut in half along the cross section, the surface of which was then ground and polished on a "Buehler" machine (Germany) using grinding discs and diamond suspensions with a dispersion of 30 to 1 μm.

The crystal structure, phase composition, and lattice parameters of the powders were studied using X-ray diffraction on an XRD-7000 diffractometer (Shimadzu, Japan) with a Bragg–Brentano flat sample arrangement in the angle range 2θ from 10 to 140° with stepwise scanning $\Delta(2\theta) = 0.03°$ and an exposure time of 2 s at a point and $CuK_{\alpha_{1,2}}$ radiation. The X-ray phase analysis (XPA) of hard alloys was carried out on a STADI-P diffractometer (Stoe, Germany) with a Bragg–Brentano flat sample arrangement in the angle range 2θ from 5 to 120° with stepwise scanning $\Delta(2\theta) = 0.03°$ and $CuK_{\alpha_{1,2}}$ radiation. The X-ray patterns were analyzed by the Rietveld method using the X'Pert HighScore Plus Version 2.2e software package and the X-ray diffraction data library built into it. The broadening of diffraction reflections of WC was used to determine the average size of coherent scattering regions (DCSR) of X-rays and the magnitude of microstrains (ε).

Chemical analysis of powders for the content of total (C_{tot}) and free (C_{free}) carbon was carried out using a "Metavak CS-30" analyzer (NPO Eksan, Izhevsk). The total oxygen content (O_{tot}) in these powders was determined by reductive melting in a carrier gas flow on an EMGA-620W/C gas analyzer (Horiba, Japan).

---

[1] Here and elsewhere - wt. %, unless otherwise stated.

The morphology and particle size of powders, as well as the microstructure of hard alloys, were studied using a JSM 6390 LA scanning electron microscope (SEM) (Jeol, Japan) equipped with a JED 2300 analyzer (Jeol, Japan) for Energy Dispersive *X*-ray (EDX) analysis of the studied area.

The specific surface area (S_{sp}) of the powders was measured by the Brunauer–Emmett–Teller (BET) adsorption method using a "Gemini VII" surface area and porosity analyzer (Micromeritics, USA) after degassing the powders in a vacuum of ~10 Pa at a temperature of 350 °C for 1 h. Assuming the approximation of the same size and spherical shape of particles, the average particle size $D_{BET} = \frac{6}{\rho_{calc} S_{sp}}$, was determined from the measured value S_{sp}, where ρcalc is the density calculated by the mixture rule according to the *X*-ray phase composition.

The density of hard alloys (ρ_{meas}) was determined using an "AccuPyc II 1340" helium pycnometer (Micromeritics, USA) and a measuring chamber with a volume of 1 cm^3. The porosity of hard alloys was calculated according to the formula: $p = \frac{\rho_{calc} - \rho_{meas}}{\rho_{calc}} \cdot 100\ \%$.

The microhardness of hard alloys was measured according to the Vickers method on a MICROMET-1 microhardness tester (Buehler, Germany) with an automatic indentation of a diamond pyramid at a load of 200 g and a the duaration of loading of 10 s. At least 10 measurements (diamond pyramid indentations) were carried out on each sample, after which both diagonals were measured on each indentation, and the average microhardness value and the measurement error were determined from the data obtained.

Results and discussion

The *X*-ray diffraction patterns of all the initial powders (Fig. 1) used in this work for the preparation of

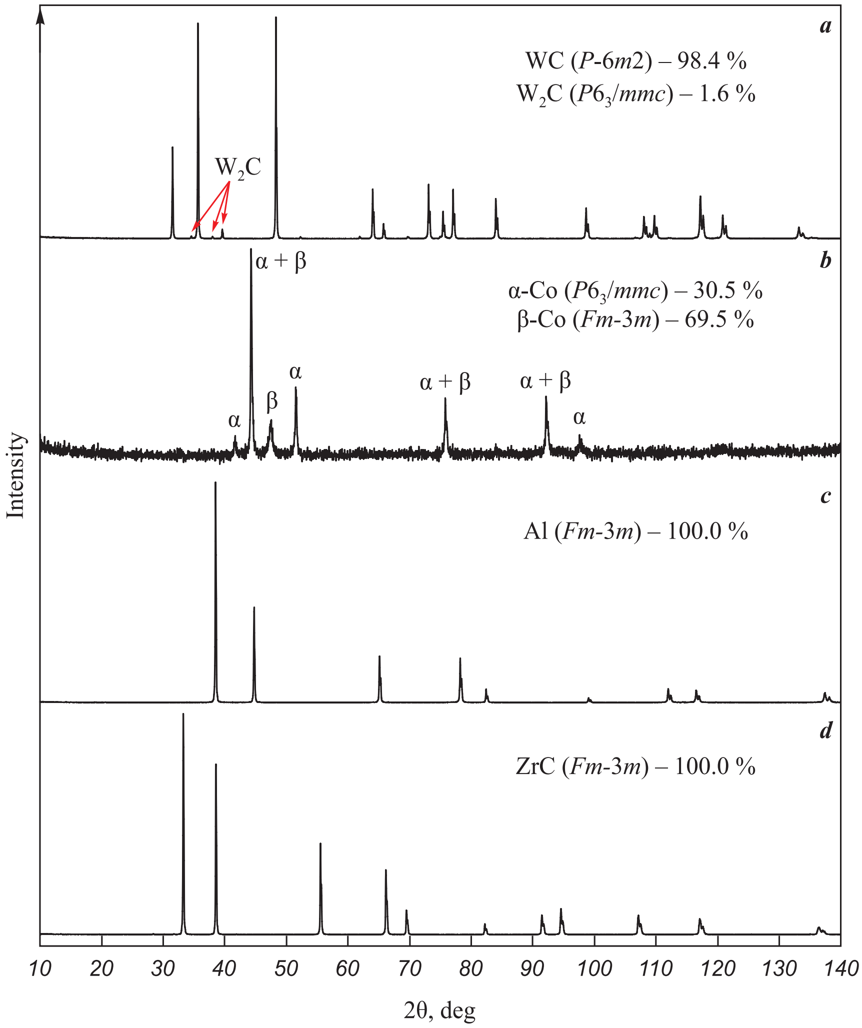

Fig. 1. *X*-ray diffraction patterns of the initial WC (***a***), Co (***b***), Al (***c***) and ZrC (***d***) powders

Рис. 1. Рентгенограммы исходных порошков WC (***a***), Co (***b***), Al (***c***) и ZrC (***d***) nanocrystalline powder mixtures show rather narrow diffraction reflections, which confirms their coarseness. The WC powder is two-phase (Fig. 1, *a*) and, along with the main phase of hexagonal WC (sp. gr. $P\text{-}6m2$), contains a small amount of lower tungsten carbide W_2C with a hexagonal structure (sp. gr. $P6_3/mmc$), which indicates insufficient content of bound carbon in the W–C system. According to chemical analysis, the content of bound carbon (6.08 %) in WC powder is, indeed, lower than the stoichiometric value (6.13 %), however, there is present free carbon (0.07 %), therefore, the total carbon content in the powder (6.15 %) is sufficient to achieve single-phase WC during sintering. Cobalt Co powder (Fig. 1, *b*) is also two-phase and contains both crystalline modifications: low-temperature (up to 427 °C) α-Co with a hexagonal structure (sp. gr. $P6_3/mmc$) and high-temperature (from 427 to 1495 °C) β-Co with a cubic structure (sp. gr. $Fm\text{-}3m$). Al (Fig. 1, *c*) and ZrC (Fig. 1, *d*) powders are single-phase and contain only cubic phases (sp. gr. $Fm\text{-}3m$) of Al and ZrC, respectively.

According to SEM images (Fig. 2), the Al powder (Fig. 2, *c*) contains the largest particles (up to 30–40 μm), which are several times larger than the particles of other powders. Co and ZrC powders, on the contrary, appear to be the most dispersed, showing very small rounded particles <1 μm in size, however, most of them are tightly bound together and form large agglomerates with a highly developed surface, ranging in size from hundreds of nanometers to several micrometers (Fig. 2, *b*, *d*). The WC powder (Fig. 2, *a*) is similar in particle morphology to Al powder (Fig. 2, *c*), but is closer to Co and ZrC powders in particle size and their agglomerates (Fig. 2, *b*, *d*).

Table 1 shows the average, maximum, and minimum particle sizes of the initial powders, determined from their SEM images, as well as their specific surface and the average particle size calculated from it.

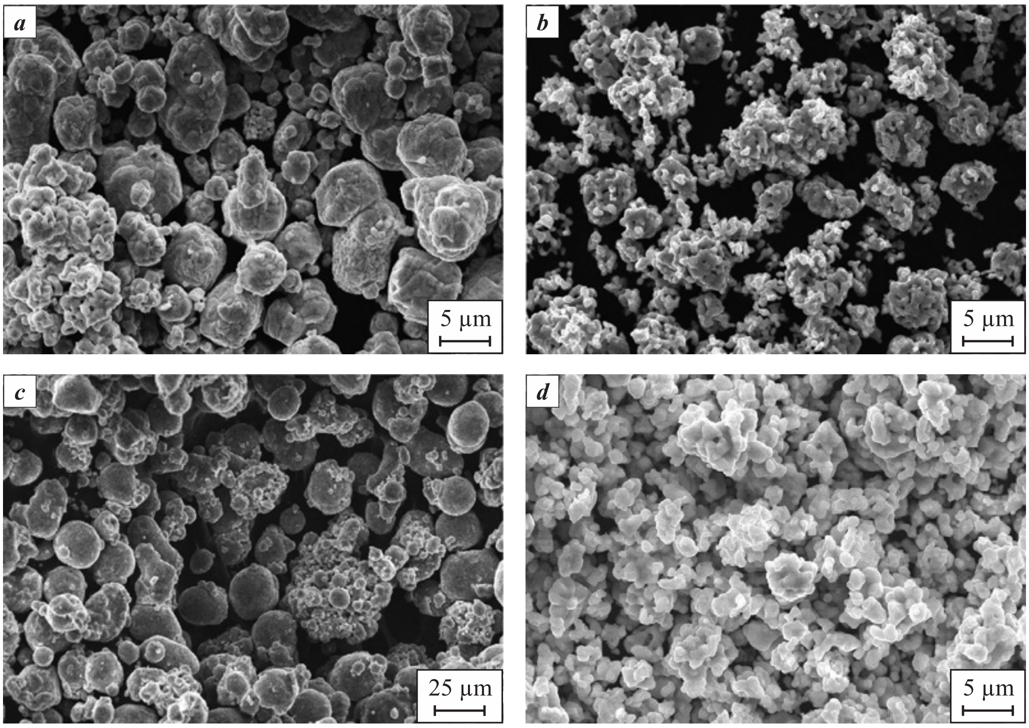

Fig. 2. SEM images of the initial WC (***a***), Co (***b***), Al (***c***) and ZrC (***d***) powders

Рис. 2. СЭМ-изображения исходных порошков WC (***a***), Co (***b***), Al (***c***) и ZrC (***d***)

Table 1. **Characteristics of initial powders**

Таблица 1. **Характеристики исходных порошков**

Powder	D_{av}, μm	D_{min}, μm	D_{max}, μm	S_{sp}, m^2/g	ρ_{calc}, g/cm^3	D_{BET}, μm
WC	3.03	0.52	12.08	0.19 ± 0.01	15.70	1.97
Co	1.37	0.30	4.48	0.98 ± 0.01	8.80	0.69
Al	7.91	0.70	36.36	0.37 ± 0.02	2.70	6.02
ZrC	1.83	0.39	5.98	0.68 ± 0.01	6.63	1.32

After preparation, all powder mixtures, according to *X*-ray diffraction (Fig. 3) and SEM (Fig. 4), look the same. The *X*-ray diffraction patterns of the mixtures (Fig. 3) show the same reflections as for the initial WC powder (see Fig. 1, *a*), which belong to the WC and W_2C phases. However, due to the small size of the CSR and the presence of microdeformations, the diffraction reflections in the *X*-ray diffraction patterns of powder mixtures are noticeably broadened, due to which weak reflections of Co and Al or ZrC, are not visible. A quantitative analysis of the broadening of WC reflections showed that the average CSR sizes and microstrains for WC particles in all powder mixtures have close values (Table 2). The same is observed on the SEM images (Fig. 4), where powder mixtures have very little differences both in terms of particle size and morphology, although the initial powders were considerably different, especially Al powder (see Fig. 2).

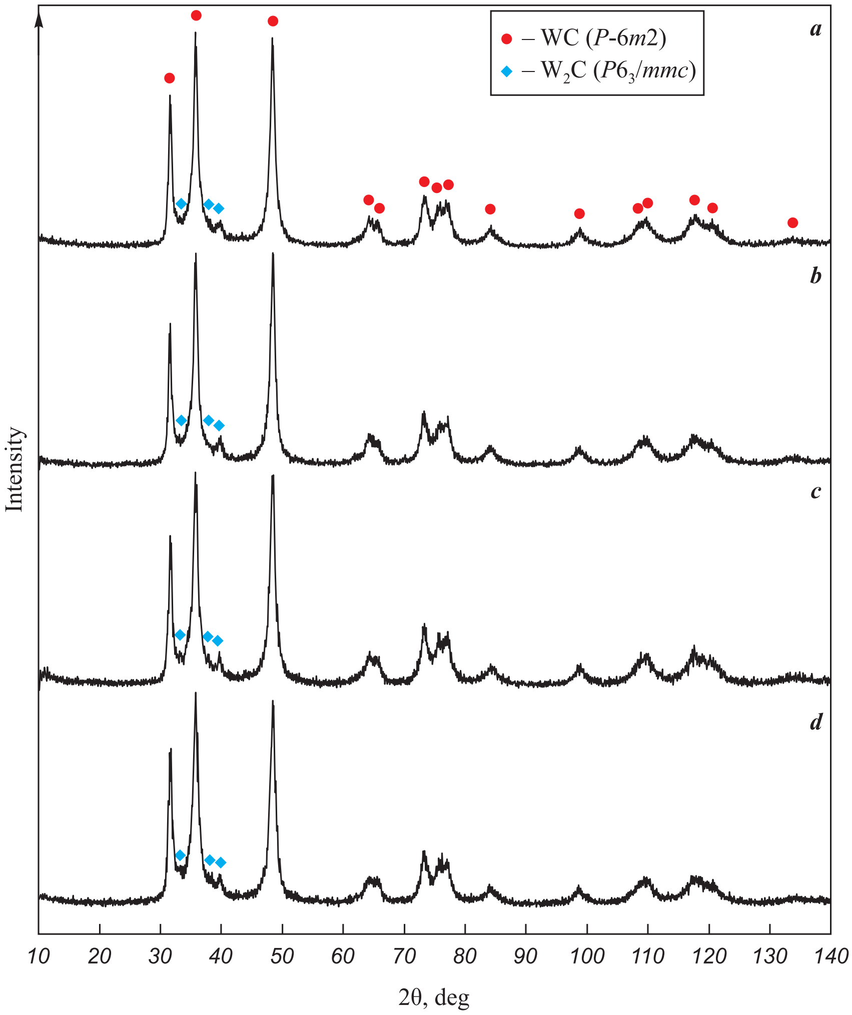

Fig. 3. *X*-ray diffraction patterns of nanocrystalline powder mixtures WC–6Co (***a***), WC–6Co–0.5C (***b***), WC–6Co–0.4Al (***c***) and WC–6Co–4ZrC (***d***)

Рис. 3. Рентгенограммы нанокристаллических порошковых смесей WC–6Co (***a***), WC–6Co–0,5C (***b***), WC–6Co–0,4Al (***c***) и WC–6Co–4ZrC (***d***)

Table 2. **Characteristics of nanocrystalline powder mixtures**

Таблица 2. **Характеристики нанокристаллических порошковых смесей**

Powder	O_{tot}, wt. %	S_{sp}, m^2/g	ρ_{calc}, g/cm^3	D_{BET}, nm	D_{CSR}, nm	ε, %
WC–6Co	3.3 ± 0.1	5.81 ± 0.05	14.99	69	47	0.81
WC–6Co–0.5C	3.4 ± 0.1	5.03 ± 0.04	14.49	82	34	0.70
WC–6Co–0.4Al	4.2 ± 0.1	8.12 ± 0.06	14.74	50	33	0.75
WC–6Co–4ZrC	4.3 ± 0.1	9.64 ± 0.06	14.25	44	39	0.88

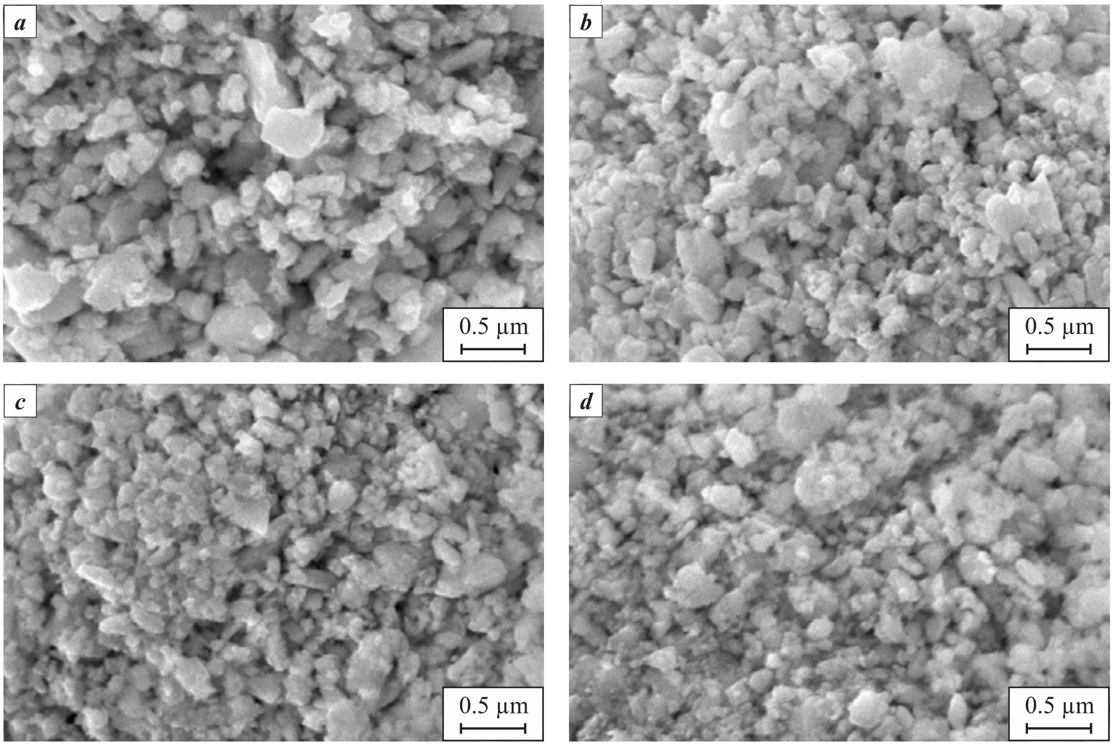

Fig. 4. SEM images of powder mixtures
WC–6Co (***a***), WC–6Co–0.5C (***b***), WC–6Co–0.4Al (***c***) and WC–6Co–4ZrC (***d***)

Рис. 4. СЭМ-изображения порошковых смесей
WC–6Co (***a***), WC–6Co–0,5C (***b***), WC–6Co–0,4Al (***c***) и WC–6Co–4ZrC (***d***)

Thus, all the additives used in this work not only did not affect the grinding of WC, but themselves turned out to be grinded and subjected to grinding and uniform distribution throughout the volume of the powder mixture, including Al. This is also confirmed by the values of the specific surface area of powder mixtures (Table 2), which are an order of magnitude higher than the values for the initial powders (Table 1), whereas the average particle sizes in the mixtures calculated from the specific surface turned out to be close in magnitude to the average CSR sizes and do not exceed 100 nm (Table 2). It should be noted, however, that the additives introduced into the powder mixture, as expected, also introduced additional oxygen; its measured total content in nanocrystalline powder mixtures significantly exceeds the amount estimated based on the change in the phase composition (Table 2).

Despite the similarity of the obtained powder mixtures, hard alloys sintered from them significantly differ from each other both in phase composition (Fig. 5) and in microstructure (Fig. 6). On the *X*-ray diffraction pattern of the WC–6Co hard alloy (Fig. 5, *a*), which was sintered from the WC–6%Co powder mixture without any additives, diffraction reflections of three other phases are clearly visible in addition to the main phase WC, which indicate a carbon deficiency and are extremely undesirable in a hard alloy [41]. The addition of carbon to the powder mixture almost completely made up for its deficiency in the sintered hard alloy, its *X*-ray diffraction pattern of the main WC and Co phases are observed, however, weak lines of the Co_3W_3C η-phase are still present (Fig. 5, *b*). The addition of aluminum, on the contrary, only exacerbated the consequences of carbide decarburization, as a result of which the qualitative phase composition of the alloy became similar to the composition of the hard alloy from a powder mixture without additives (Fig. 5, *a*), while the content of undesirable phases increased (Fig. 5, *c*). Probably, during the preparation of the WC–6Co–0.4Al powder mixture, all the aluminium introduced was completely oxidized to Al_2O_3 during intensive grinding, and while sintering, instead of binding the oxygen adsorbed on the carbide particles, it, on the contrary, brought additional oxygen to its surface, resulting in an even greater loss of carbon. The addition of ZrC to the powder mixture allowed to preserve fully the WC and Co phases in the hard alloy sintered from the mixture, binding most of the adsorbed oxygen into the monoclinic ZrO_2 oxide, as evidenced by the *X*-ray phase composition of the sintered alloy (Fig. 5, *d*).

According to the XRD results of hard alloys, the assessment of carbon loss (~0.5 %) and the amount of oxygen involved (~1.3 %) based on the change in

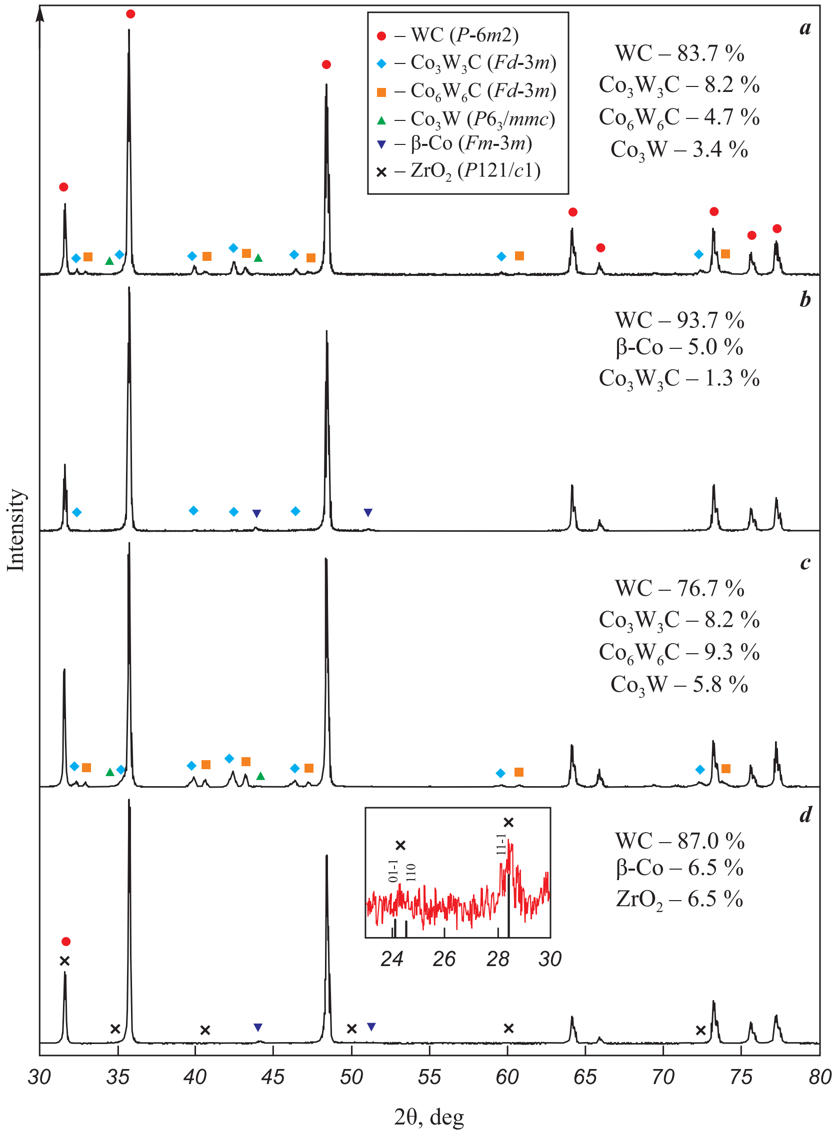

Fig. 5. *X*-ray diffraction patterns of hard alloys
WC–6Co (***a***), WC–6Co–0.5C (***b***), WC–6Co–0.4Al (***c***), and WC–6Co–4ZrC (***d***)
The inset shows an enlarged fragment of the *X*-ray diffraction pattern with the most intense (11-1) line of the ZrO_2 phase

Рис. 5. Рентгенограммы твердых сплавов
WC–6Co (***a***), WC–6Co–0,5C (***b***), WC–6Co–0,4Al (***c***) и WC–6Co–4ZrC (***d***)
На вставке – увеличенный фрагмент рентгенограммы с наиболее интенсивной линией (11-1) фазы ZrO_2

the phase composition allowed for fairly accurate calculation of the amount of carbon and ZrC additives required to prevent WC decarburization. However, the measured total oxygen content in nanocrystalline powder mixtures (see Table 2) turned out to be several-fold higher than the estimated one. This means that only a part of the oxygen contained in the powder mixture is in the chemisorbed state, while the rest is present in other forms, including in the form of physically adsorbed water, which is removed upon heating without taking part in the decarburization of WC.

The microstructure of the WC–6Co alloy sintered from a powder mixture without additives (Fig. 6, *a*) looks rather dense and includes WC grains (light-colored), the space between which is filled with cobalt-containing phases (dark-colored) detected by *X*-ray diffraction (Fig. 5, *a*), and a few pores (black) no larger than 1 μm in size. Only WC grains and their intergrowths separated by a cobalt binder are observed in the microstructure of the WC–6Co–0.5C hard alloy sintered from a powder mixture with the addition of carbon (Fig. 6, *b*). As can be seen from XRD-analysis, the addition of Al to the powder mixture filled the microstructure of the hard alloy sintered from it (Fig. 6, *c*) with a large number of rounded inclusions (black-colored), resembling pores, among the grains of WC (light-colored) and cobalt-containing phases (dark-colored), (Fig. 5, *c*). The EDX analysis

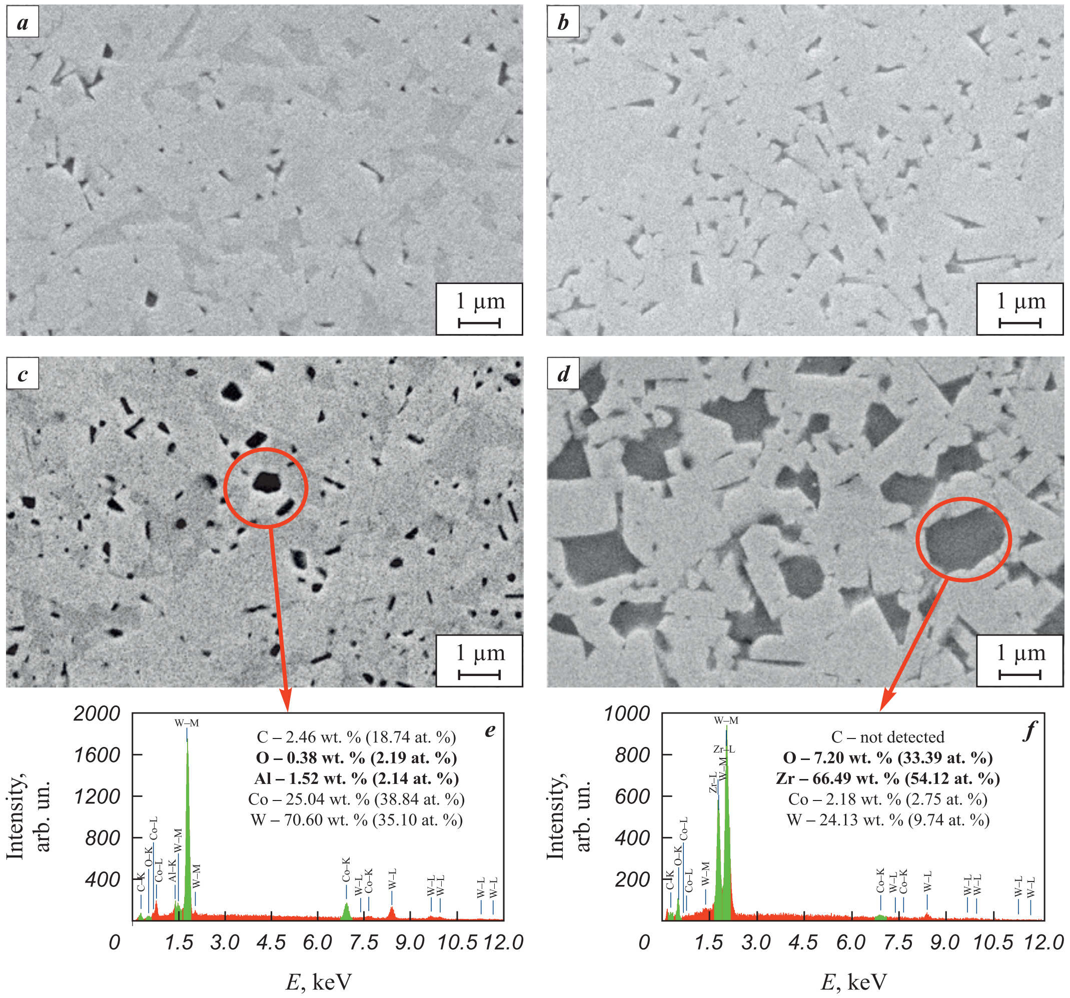

Fig. 6. SEM images of hard alloys
WC–6Co (***a***), WC–6Co–0.5C (***b***), WC–6Co–0.4Al (***c***) and WC–6Co–4ZrC (***d***)
and the results of EDX analysis of the selected areas (***e***, ***f***)

Рис. 6. СЭМ-изображения твердых сплавов
WC–6Co (***a***), WC–6Co–0,5C (***b***), WC–6Co–0,4Al (***c***) и WC–6Co–4ZrC (***d***)
и результаты EDX-анализа выделенных областей (***e***, ***f***)

Table 3. **Characteristics of sintered hard alloys**

Таблица 3. **Характеристики спеченных твердых сплавов**

Sample	D_{av}, µm	D_{min}, µm	D_{max}, µm	*HV*, GPa	ρ_{meas}, g/cm^3	ρ_{calc}, g/cm^3	*p*, %
WC–6Co	0.80	0.14	2.57	19.3 ± 0.8	15.14 ± 0.01	15.41	1.8
WC–6Co–0.5C	0.84	0.21	3.23	18.4 ± 0.5	15.03 ± 0.01	15.07	0.3
WC–6Co–0.4Al	0.78	0.25	1.63	18.0 ± 1.0	14.76 ± 0.01	14.99*	1.5
WC–6Co–4ZrC	1.08	0.28	4.43	17.2 ± 0.9	13.79 ± 0.01	13.86*	0.5

* Taking into account that Al and ZrC transformed completely into Al_2O_3 and ZrO_2.

showed that the rounded dark areas observed in the microstructure of the WC–6Co–0.4Al hard alloy contain aluminum and oxygen (Fig. 6, *c*, *e*) and are Al_2O_3 particles and not pores. The authors of [36] reported similar inclusions in the WC–3Co–3Al_2O_3 alloy, detected using field emission scanning microscopy (FESEM) and EDX mapping (MAP), which showed that these are Al_2O_3. The microstructure of the hard alloy (Fig. 6, *d*) made from a powder mixture with the addition of ZrC is a dense composition of carbide WC (light-colored) and oxide ZrO_2 (dark-colored) grains surrounded by a cobalt layer, as confirmed by the EDX (Fig. 6, *f*) and XFA (Fig. 5, *d*) analysis. Though in the WC–6Co–4ZrC powder mixture WC and ZrC nanoparticles are distributed uniformly over the entire volume, as it can be seen from the SEM images (Fig. 4, *d*), individual microcrystalline ZrO_2 and WC grains formed in the microstructure of the hard alloy sintered from the powder, i.e. the growth of grains of various phases was not limited, as expected, on the contrary, it was supported.

Table 3 shows the average, minimum, and maximum WC grain sizes determined from several SEM images for each hard alloy. According to these data, the carbon deficiency in the alloy inhibits the growth of WC grains, especially in the presence of Al_2O_3 particles, while the addition of carbon or ZrC, quite the contrary, promotes the growth of carbide grains, as confirmed by the average and maximum grain sizes in the hard alloy (Table 3). It is known that the presence of free carbon promotes the growth of WC grains during sintering, especially in the case of liquid-phase sintering [42]. According to [43; 44], during the oxidation of ZrC, there is a dissolution of oxygen in the carbide lattice; it is first accompanied by the formation of oxycarbide with the release of free carbon and zirconium from the carbide lattice; as oxygen further dissolves, the oxycarbide transforms into the cubic ZrO_2 phase containing a certain amount of carbon, and then upon complete oxidation, it transforms into the ZrO_2 monoclinic phase, which is seen in the *X*-ray diffraction pattern of the hard alloy (Fig. 5, *d*). Unlike ZrC, during the oxidation of WC, carbon leaves the carbide lattice in the form of CO/CO_2, leading to its decarburization [43; 45]. Thus, heating of the WC–6Co–4ZrC powder mixture, ZrC carbide not only binds the adsorbed oxygen into ZrO_2 oxide, but also compensates for the loss of carbon in WC, as is the case with the addition of carbon in the WC–6Co–0.5C mixture.

The additives used not only affected the microstructure of the hard alloy, but also led to a decrease in its density and microhardness (Table 3). The calculated density of the hard alloy with the WC–6Co phase composition is 14.97 g/cm^3. However, due to the loss of carbon during sintering and the resulting formation of undesirable phases (Fig. 5, *a*), the density of the WC–6Co hard alloy (both calculated and measured) exceeded the expected one. The hard alloy WC–6Co–0.5C turned out to be closest to the WC–6Co hard alloy both in terms of phase composition and density. As *X*-ray diffraction patterns of hard alloys produced from powder mixtures WC–6Co–0.4Al and WC–6Co–4ZrC did not show reflections of the initial phases (Al or ZrC), while inclusions close in composition to Al_2O_3 and ZrO_2 were found in the microstructure, the density of the samples ρcalc was calculated from the *X*-ray phase composition, taking into account the amount of oxide, into which the entire additive could turn. Calculations and measured density values of hard alloys showed that additions of carbon and ZrC, making up for the loss of carbon during sintering, contribute to the formation of a microstructure with the lowest porosity compared to carbon-deficient hard alloys (Table 3).

Besides, the deviation of the phase composition of the hard alloy from the perfect WC–6Co is accompanied by an increase in the inhomogeneity (scatter of values) of its microhardness, as confirmed by the measured value's error (Table 3). Overall, the measurements have shown that carbon deficiency leads to an increase in microhardness, while the presence of Al_2O_3 and ZrO_2 oxide inclusions in the hard alloy microstructure, on the contrary, reduces it.

Conclusion

Homogeneous nanocrystalline powder mixtures with the average particle size not exceeding 100 nm based on WC–6Co with and without additives of C, Al, ZrC were prepared by high-energy milling from crystalline powders differing in their composition, properties, quantity, and average particle size. In the obtained mixtures, a high oxygen content was found; the amount of oxygen increases with the introduction of additives, especially Al. Though the original aluminum powder contained very large particles, it was completely oxidized during milling and turned into nanocrystalline oxide Al_2O_3; this fact only increased the loss of carbon during sintering and led to the formation of a multiphase and relatively porous microstructure of the hard alloy.

It was shown that only a part of oxygen contained in the powder mixtures is in the chemisorbed state and takes part in the decarburization of WC during vacuum sintering. The use of carbon and ZrC additives allowed to prevent the decarburization of WC during sintering of the hard alloy and to form a less porous microstructure in it. However, even the presence of ZrO_2 inclusions could not impede the intensive growth of WC grains during sintering, on the contrary, it rather promoted it. Besides, the microhardness measurements have shown that carbon deficiency leads to an increase in microhardness, while the presence of Al_2O_3 and ZrO_2 oxide inclusions in the hard alloy microstructure, on the contrary, reduces it.

References / Список литературы

1. Samoilov V.S., Eikhmans E.F., Fal'kovskii V.A., Loktev A.D., Shkurin Yu.P. Metalworking carbide tools: Handbook. Moscow: Mashinostroenie, 1988. 368 p. (In Russ.).

Самойлов В.С., Эйхманс Э.Ф., Фальковский В.А., Локтев А.Д., Шкурин Ю.П. Металлообрабатывающий твердосплавный инструмент: Справочник. М.: Машиностроение, 1988. 368 с.

2. Falkovskii V.A., Klyachko L.I. Hard alloys. Moscow: Publ. Ruda i metally, 2005, 413 p. (In Russ.).

   Фальковский В.А., Клячко Л.И. Твердые сплавы. М.: Изд. дом «Руда и металлы», 2005. 413 с.

3. Panov V.S., Chuvilin A.M. Technology and properties of sintered hard alloys and products from them. Moscow: MISIS, 2001, 432 p. (In Russ.).

   Панов В.С., Чувилин А.М. Технология и свойства спеченных твердых сплавов и изделий из них. Учеб. пос. для вузов. М.: МИСИС, 2001. 432 с.

4. Lassner E., Schubert W.D. Tungsten compounds and their application. In: *Tungsten: Properties, chemistry, technology of the element, alloys, and chemical compounds*. Boston: Springer, MA, 1999. P. 133–177.
   https://doi.org/10.1007/978-1-4615-4907-9_4

5. Sarin V.K. Comprehensive hard materials. Oxford: Elsevier, 2014. 1806 p.

6. Gusev A.I., Kurlov A.S. Mechanical milling process modeling and making WC nanocrystalline powder. *Inorganic Materials*. 2009;45:35–42.
   https://doi.org/10.1134/S0020168509010063

   Гусев А.И., Курлов А.С. Моделирование процесса механического размола и получение нанокристаллического порошка WC. *Неорганические материалы*. 2009;45(1):38–45.

7. El-Eskandarany M.S., Mahday A.A., Ahmed H.A., Amer A.H. Synthesis and characterizations of ball-milled nanocrystalline WC and nanocomposite WC–Co powders and subsequent consolidations. *Journal of Alloys and Compounds*. 2000;312(1–2):315–325.
   https://doi.org/10.1016/S0925-8388(00)01155-5

8. Isaeva N.V., Blagoveshchenskii Yu.V., Blagoveshchenskaya N.V., Mel'nik Yu.I., Samokhin A.V., Alekseev N.V., Astashov A.G. Preparation of nanopowders of carbides and hard-alloy mixtures applying low-temperature plasma. *Russian Journal of Non-Ferrous Metals*. 2014;55(6):585–591.
   https://doi.org/10.3103/S1067821214060108

   Исаева Н.В., Благовещенский Ю.В., Благовещенская Н.В., Мельник Ю.И., Самохин А.В., Алексеев Н.В., Асташов А.Г. Получение нанопорошков карбидов и твердосплавных смесей с применением низкотемпературной плазмы. *Известия вузов. Порошковая металлургия и функциональные покрытия*. 2013;(3):7–14.
   https://doi.org/10.17073/1997-308X-2013-3-7-14

9. McChandlish L.E., Seegopaul P. Development and applications of nanostructured tungsten carbide/cobalt powders. In: *Proceedings of the European Conference on Advances in Hard Materials*, Stockholm, 1996. P. 93–100.

10. Gao L., Kear B.H. Low temperature carburization of high surface area tungsten powders. *Nanostructured Materials*. 1995;5(5):555–569.
    https://doi.org/10.1016/0965-9773(95)00265-G

11. Fabijanić T.A., Alar Z., Ćorić D. Influence of consolidation process and sintering temperature on microstructure and mechanical properties of near nano- and nano-structured WC–Co cemented carbides. *International Journal of Refractory Metals and Hard Materials*. 2016;54:82–89.
    https://doi.org/10.1016/j.ijrmhm.2015.07.017

12. Breval E., Cheng J.P., Agrawal D.K., Gigl P., Dennis M., Roy R., Papworth A.J. Comparison between microwave and conventional sintering of WC/Co composites. *Materials Science and Engineering: A*. 2005;391(1–2): 285–295.
    https://doi.org/10.1016/j.msea.2004.08.085

13. Chuvil'deev V.N., Moskvicheva A.V., Boldin M.S., Sakharov N.V., Blagoveshchenskii Yu.V., Isaeva N.V., Mel'nik Yu.I., Shotin S.V., Nokhrin A.V. Spark plasma sintering of nanostructured tungsten carbide and carbide alloys. *Vestnik of Lobachevsky University of Nizhni Novgorod*. 2013;2(2):115–119. (In Russ.).

    Чувильдеев В.Н., Москвичева А.В., Болдин М.С., Сахаров Н.В., Благовещенский Ю.В., Исаева Н.В., Мельник Ю.И., Шотин С.В., Нохрин А.В. Электроимпульсное плазменное спекание наноструктурированного карбида вольфрама и твердых сплавов на его основе. *Вестник Нижегородского университета им. Н.И. Лобачевского*. 2013;2(2):115–119.

14. Kim H.C., Shon I.J., Jeong I.K., Ko I.Y., Yoon J.K., Doh J.M. Rapid sintering of ultra fine WC and WC–Co hard materials by high-frequency induction heated sintering and their mechanical properties. *Metals and Materials International*. 2007;13(1):39–45.
    https://doi.org/10.1007/BF03027821

15. Kelto C.A., Timm E.E., Pyzik A.J. Rapid omnidirectional compaction (ROC) of powder. *Annual Review of Materials Science*. 1989;19:527–550.
    https://doi.org/10.1146/annurev.ms.19.080189.002523

16. Raihanuzzaman R.M., Rosinski M., Xie Z., Ghomashchi R. Microstructure and mechanical properties and of pulse plasma compacted WC–Co. *International Journal of Refractory Metals and Hard Materials*. 2016;60:58–67.
    https://doi.org/10.1016/j.ijrmhm.2016.07.002

17. Wang X., Fang Z., Sohn H.Y. Nanocrystalline cemented tungsten carbide sintered by an ultra-high-pressure rapid hot consolidation process. In: *Proceedings of the 2007 International Conference on Powder Metallurgy & Particulate Materials*. Ed. J. Engquist. Denver, US, 2007;2:08–01.

18. Krokhalev A.V., Kharlamov V.O., Tupitsin M.A., Kuzmin S.V., Lysak V.I. Revisiting the possibility of formation of hard alloys from powder mixtures of carbides with metals by explosive compacting without sintering. *Russian Journal of Non-Ferrous Metals*. 2018;59(5):550–556.
    https://doi.org/10.3103/S1067821218050073

    Крохалев А.В., Харламов В.О., Тупицин М.А., Кузьмин С.В., Лысак В.И. О возможности получения твердых сплавов из смесей порошков карбидов с металлами взрывным прессованием без спекания. *Известия вузов. Порошковая металлургия и функциональные покрытия*. 2017;(2):22–30.

    https://doi.org/10.17073/1997-308X-2017-2-22-30

19. Raihanuzzaman R.M., Xie Z., Hong S.J., Ghomashchi R. Powder refinement, consolidation and mechanical properties of cemented carbides: An overview. *Powder Technology*. 2014;261:1–13.
    https://doi.org/10.1016/j.powtec.2014.04.024

20. Blagoveshchenskiy Y.V., Isayeva N.V., Blagoveshchenskaya N.V., Melnik Yu.I., Chuvildeyev V.N., Nokhrin A.V., Sakharov N.V., Boldin M.S., Smirnov Ye.S., Shotin S.V., Levinsky Yu.V., Voldman G.M. Methods of compacting

nanostructured tungsten-cobalt alloys from nanopowders obtained by plasma chemical synthesis. *Inorganic Materials: Applied Research*. 2015;6(5):415–426. https://doi.org/10.1134/S2075113315050032

Благовещенский Ю.В., Исаева Н.В., Благовещенская Н.В., Мельник Ю.И., Чувильдеев В.Н., Нохрин А.В., Сахаров Н.В., Болдин М.С., Смирнова Е.С., Шотин С.В., Левинский Ю.В., Вольдман Г.М. Методы компактирования наноструктурных вольфрам-кобальтовых сплавов из нанопорошков, полученных методом плазмохимического синтеза. *Перспективные материалы*. 2015;(1):5–21.

21. Norgren S., García J., Blomqvist A., Yin L. Trends in the P/M hard metal industry. *International Journal of Refractory Metals and Hard Materials*. 2015;48:31–45. https://doi.org/10.1016/j.ijrmhm.2014.07.007

22. García J., Ciprés V.C., Blomqvist A., Kaplan B. Cemented carbide microstructures: A review. *International Journal of Refractory Metals and Hard Materials*. 2019;80:40–68. https://doi.org/10.1016/j.ijrmhm.2018.12.004

23. Fang Z.Z., Wang X., Ryu T., Hwang K.S., Sohn H.Y. Synthesis, sintering, and mechanical properties of nanocrystalline cemented tungsten carbide: A review. *International Journal of Refractory Metals and Hard Materials*. 2009;27: 288–299. https://doi.org/10.1016/j.ijrmhm.2008.07.011

24. Krasovskii P.V., Blagoveshchenskii Y.V., Grigorovich K.V. Determination of oxygen in W–C–Co nanopowders. *Inorganic Materials*. 2008;44(9):954–959. https://doi.org/10.1134/S0020168508090100

Красовский П.В., Благовещенский Ю.В., Григорович К.В. Определение содержания кислорода в нанопорошках системы W–C–Co. *Неорганические материалы*. 2008;44(9):1074–1079.

25. Kurlov A.S. Effects of vacuum annealing on the particle size and phase composition of nanocrystalline tungsten carbide powders. *Russian Journal of Physical Chemistry A*. 2013;87(4):654–661. https://doi.org/10.1134/S0036024413040158

Курлов А.С. Влияние вакуумного отжига на размер частиц и фазовый состав нанокристаллических порошков WC. *Журнал физической химии*. 2013;87(4): 664–671. https://doi.org/10.7868/S0044453713040158

26. Lantsev E.A., Malekhonova N.V., Tsvetkov Yu.V., Blagoveshchensky Yu.V., Chuvildeev V.N., Nokhrin A.V., Boldin M.S., Andreev P.V., Smetanina K.E., Isaeva N.V. Investigation of aspects of high-speed sintering of plasma-chemical nanopowders of tungsten carbide with higher content of oxygen. *Inorganic Materials: Applied Research*. 2021;12(3):650–663. https://doi.org/10.1134/S2075113321030242

Ланцев Е.А., Малехонова Н.В., Цветков Ю.В., Благовещенский Ю.В., Чувильдеев В.Н., Нохрин А.В., Болдин М.С., Андреев П.В., Сметанина К.Е., Исаева Н.В. Исследование особенностей высокоскоростного спекания плазмохимических нанопорошков карбида вольфрама с повышенным содержанием кислорода. *Физика и химия обработки материалов*. 2020;(6):23–39.

https://doi.org/10.30791/0015-3214-2020-6-23-39

27. Kurlov A.S., Gusev A.I., Rempel’ A.A. Vacuum sintering of WC–8wt.%Co hardmetals from WC powders with different dispersity. *International Journal of Refractory Metals and Hard Materials*. 2011;29(2):221–231. https://doi.org/10.1016/j.ijrmhm.2010.10.010

28. Kurlov A.S., Rempel’ A.A., Blagoveshenskii Y.V., Samokhin A.V., Tsvetkov Yu.V. Hard alloys WC–Co (6 wt %) and WC–Co (10 wt %) based on nanocrystalline powders. *Doklady Chemistry.* 2011;439(1):213–218. https://doi.org/10.1134/S0012500811070068

Курлов А.С., Ремпель А.А., Благовещенский Ю.В., Самохин А.В., Цветков Ю.В. Твердые сплавы WC–6 мас.%Co и WC–10 мас.%Co на основе нанокристаллических порошков. *Доклады Академии наук*. 2011;439(2):215–220.

29. Lantsev E.A., Malekhonova N.V., Nokhrin A.V., Chuvil’deev V.N., Boldin M.S., Andreev P.V., Smetanina K.E., Blagoveshchenskiy Yu.V., Isaeva N.V., Murashov A.A. Spark plasma sintering of fine-grained WC hard alloys with ultra-low cobalt content. *Journal of Alloys and Compounds*. 2021;857:157535. https://doi.org/10.1016/j.jallcom.2020.157535

30. Kurlov A.S., Yumasheva N.D., Danilov D.A. Concentration of oxygen and forms of it in TaC nanopowders. *Russian Journal of Physical Chemistry A*. 2019;93(3):501–508. https://doi.org/10.1134/S0036024419030117

Курлов А.С., Юмашева Н.Д., Данилов Д.А. Содержание кислорода и формы его существования в нанопорошках TaC. *Журнал физической химии*. 2019;93(3):405–413. https://doi.org/10.1134/S0044453719030117

31. Kurlov A.S., Yumasheva N.D., Danilov D.A. Vacuum annealing of TaC nanopowders. *Russian Journal of Physical Chemistry A*. 2020;94(7):1447–1455. https://doi.org/10.1134/S0036024420070183

Курлов А.С., Юмашева Н.Д., Данилов Д.А. Вакуумный отжиг нанопорошков TaC. *Журнал физической химии*. 2020;94(7):1083–1092. https://doi.org/10.31857/S0044453720070183

32. Bokov A., Shelyug A., Kurlov A. Interplay between decarburization, oxide segregation, and densification during sintering of nanocrystalline TaC and NbC. *Journal of the European Ceramic Society*. 2021;41(12):5801–5812. https://doi.org/10.1016/j.jeurceramsoc.2021.05.007

33. Abyzov A.M. Aluminum oxide and alumina ceramics (Review). Pt. 1. Properties of Al_2O_3 and commercial production of dispersed Al_2O_3. *Refractories and Industrial Ceramics*. 2019;60(1):24–32. https://doi.org/10.1007/s11148-019-00304-2

Абызов А.М. Оксид алюминия и алюмооксидная керамика (Обзор). Ч. 1. Свойства Al_2O_3 и промышленное производство дисперсного Al_2O_3. *Новые огнеупоры*. 2019;(1): 16–23. https://doi.org/10.17073/1683-4518-2019-1-16-23

34. Zhigachev A.O., Golovin Yu.I., Umrikhin A.V., Korenkov V.V., Tyurin A.I., Rodaev V.V., Dyachek T.A. Ceramic materials based on zirconium dioxide. Moscow: Tekhnosfera. 2018, 358 p. (In Russ.).

Жигачев А.О., Головин Ю.И., Умрихин А.В., Кореньков В.В., Тюрин А.И., Родаев В.В., Дьячек Т.А. Керамические материалы на основе диоксида циркония. М.: Техносфера, 2018. 358 с.

35. Gordeev Yu.I., Abkaryan A.K., Zeer G.M. Design and investigation of hard metals and ceramics composites modified by nanoparticles. *Perspektivnye materialy*. 2012;(5):76–88. (In Russ.).

Гордеев Ю.И., Абкарян А.К., Зеер Г.М. Конструирование и исследование твердосплавных и керамических композитов, модифицированных наночастицами. *Перспективные материалы*. 2012;(5):76–88.

36. Fazili A., Nikzad L., RahimiPour M.R., Razavi M., Salahi E. Effect of Al_2O_3 ceramic binder on mechanical and microstructure properties of spark plasma sintered WC–Co cermets. *International Journal of Refractory Metals and Hard Materials*. 2017;69:189–195. https://doi.org/10.1016/j.ijrmhm.2017.08.010

37. Mukhopadhyay A., Chakravarty D., Basu B. Spark plasma-sintered WC–ZrO_2–Co nanocomposites with high fracture toughness and strength. *Journal of the American Ceramic Society*. 2010;93(6):1754–1763. https://doi.org/10.1111/j.1551-2916.2010.03685.x

38. Xia X., Li X., Li J., Zheng D. Microstructure and characterization of WC–2.8wt% Al_2O_3–6.8wt% ZrO_2 composites produced by spark plasma sintering. *Ceramics International*. 2016;42(12):14182–14188. https://doi.org/10.1016/j.ceramint.2016.06.044

39. Arenas F.J., Matos A., Cabezas M., Rauso C.D., Grigorescu C. Densification, mechanical properties and wear behavior of WC–VC–Co–Al hardmetals. *International Journal of Refractory Metals and Hard Materials*. 2001;19(4–6):381–387. https://doi.org/10.1016/S0263-4368(01)00014-2

40. André B., Coulet M.-V., Esposito P.-H., Rufino B., Denoyel R. High-energy ball milling to enhance the reactivity of aluminum nanopowders. *Materials Letters*. 2013;110:108–110. https://doi.org/10.1016/j.matlet.2013.07.101

41. Kurlov A.S., Gusev A.I. Tungsten carbides: Structure, properties and application in hardmetals. In: In: *Tungsten carbides.* (Springer series in materials science). Vol. 184. Springer, Cham., 2013. 242 p. https://doi.org/10.1007/978-3-319-00524-9

42. Konyashin I., Hlawatschek S., Ries B., Lachmann F., Dorn F., Sologubenko A., Weirich T. On the mechanism of WC coarsening in WC–Co hardmetals with various carbon contents. *International Journal of Refractory Metals and Hard Materials*. 2009;27(2):234–243. https://doi.org/10.1016/j.ijrmhm.2008.09.001

43. Voitovich R.F. Oxidation of carbides and nitrides. Kiev: Naukova dumka. 1981, 192 p. (In Russ.).

Войтович Р.Ф. Окисление карбидов и нитридов. Киев: Наук. думка, 1981. 192 с.

44. Gasparrini C., Chater R.J., Horlait D., Vandeperre L., Lee W.E. Zirconium carbide oxidation: Kinetics and oxygen diffusion through the intermediate layer. *Journal of the American Ceramic Society*. 2018;101(6):2638–2652. https://doi.org/10.1111/jace.15479

45. Kurlov A.S., Gusev A.I. Peculiarities of vacuum annealing of nanocrystalline WC powders. *International Journal of Refractory Metals and Hard Materials*. 2012;32:51–60. https://doi.org/10.1016/j.ijrmhm.2012.01.009

Information about the Authors

Sergey V. Briakunov – Engineer of the Laboratory of nonstoichiometric compounds of Institute of Solid State Chemistry of Ural Branch of the Russian Academy of Sciences; Senior Lecturer of Electronic Engineering Department of Ural Federal University
ORCID: 0000-0002-6430-0710
E-mail: s.v.briakunov@urfu.ru

Aleksey S. Kurlov – Cand. Sci. (Phys.-Math.), Head of Laboratory of nonstoichiometric compounds of Institute of Solid State Chemistry of Ural Branch of the Russian Academy of Sciences
ORCID: 0000-0002-6223-4465
E-mail: kurlov@ihim.uran.ru

Сведения об авторах

Сергей Владимирович Брякунов – инженер лаборатории нестехиометрических соединений, Институт химии твердого тела УрО РАН; старший преподаватель кафедры электронного машиностроения, Уральский федеральный университет
ORCID: 0000-0002-6430-0710
E-mail: s.v.briakunov@urfu.ru

Алексей Семенович Курлов – к.ф.-м.н., зав. лабораторией нестехиометрических соединений, Институт химии твердого тела УрО РАН
ORCID: 0000-0002-6223-4465
E-mail: kurlov@ihim.uran.ru

Contribution of the Authors

S. V. Briakunov – conducting the experiments, processing of the research results.
A. S. Kurlov – formation of the main concept, goal and objectives of the study, analysis of the research results, writing the text, formulation of the conclusions.

Вклад авторов

С. В. Брякунов – проведение экспериментов, обработка результатов исследований.
А. С. Курлов – формирование основной концепции, постановка цели и задачи исследования, анализ результатов исследований, подготовка текста, формулировка выводов.

Received 19.04.2022
Revised 02.06.2022
Accepted 06.06.2022

Статья поступила 19.04.2022 г.
Доработана 02.06.2022 г.
Принята к публикации 06.06.2022 г.

Nanostructured Materials and Functional Coatings
Наноструктурированные материалы и функциональные покрытия

UDC 621.45.038.7

https://doi.org/10.17073/1997-308X-2023-1-63-74

Research article
Научная статья

The influence of Ni on the composition, structure and properties of Ti–Cr–N coatings

A. V. Chernogor, I. V. Blinkov, D. S. Belov,
V. S. Sergevnin, A. P. Demirov

National University of Science and Technology "MISIS",
4 Leninskiy Prosp., Moscow 119049, Russian Federation

biv@misis.ru

Abstract. The influence of nickel on the structure and properties of Ti–Cr–N ion-plasma coatings obtained by arc-PVD method has been studied. With a nickel content of up to 11.9 at. %, the coating consists of Cr_2N, $Ti_{1-x}Cr_xN$, and metallic Ni. Upon further increase in Ni concentration in the coating, intermetallic compound Ni_3Ti is formed. The structure of the coatings was studied using the transmission electron microscopy. The coatings of Ti–Cr–N system are characterized by a columnar structure, in the columns of which $Ti_{1-x}Cr_xN$ and $Ti_{1-y}Cr_yN$ ($x > y$) sublayers, being several nanometers thick and containing variable concentration of titanium and chromium, as well as Cr_2N sublayers of about 25 nm are formed due to the complete solubility of TiN and Cr_2N and the planetary rotation of the substrates, resulting in layer-by-layer stacking of the components of the evaporated cathodes. This structure remains intact in coatings of Ti–Cr–N–Ni system with a low nickel concentration (on the order of tenths of at. %). However, upon that, the column size refinement and an increase in biaxial compressive stresses from 6.7 to 9.7 GPa are observed, which results in an increase in hardness from 30 to 42 GPa. The coatings with a high nickel content are characterized by a multilayer architecture with an equiaxed polycrystalline structure of nanograins in layers. As Ni concentration increases, the hardness of the coating decreases to 16.7 GPa, which is associated with an increase in the fraction of relatively soft nickel in the coating and a decrease in macrostresses to –0.6 GPa. Upon that, the wear intensity increases from $3\cdot10^{-15}$ to $5\cdot10^{-15}$ $m^3/(N\cdot m)$. The studied coatings of Ti–Cr–N and Ti–Cr–N–Ni systems are resistant to adhesive and cohesive destruction. With an increase in the nickel content upon measuring scratching, the destruction of the coatings occurs exclusively due to the plastic deformation.

Keywords: ceramic coatings, ceramic and metal coatings, wear resistance, tribology, nitrides, hardness

Acknowledgements: the study was supported by the Russian Science Foundation grant No. 19-19-00555, https://rscf.ru/project/19-19-00555/
The authors express their gratitude to the Doctor of engineering sciences F. V. Kiryukhantsev-Korneev for his help in conducting research on the heat resistance of coatings.

For citation: Chernogor A.V., Blinkov I.V., Belov D.S., Sergevnin V.S., Demirov A.P. The influence of Ni on the composition, structure and properties of Ti–Cr–N coatings. *Powder Metallurgy and Functional Coatings*. 2023;17(1):63–74. https://doi.org/10.17073/1997-308X-2023-1-63-74

Влияние никеля на состав, структуру и свойства покрытий Ti–Cr–N

А. В. Черногор, И. В. Блинков, Д. С. Белов,
В. С. Сергевнин, А. П. Демиров

Национальный исследовательский технологический университет «МИСИС»
Россия, 119049, г. Москва, Ленинский пр-т, 4

✉ biv@misis.ru

Аннотация. Исследовано влияние никеля на структуру и свойства ионно-плазменных покрытий Ti–Cr–N, полученных методом arc-PVD. При содержании никеля до 11,9 ат. % покрытие состоит из Cr_2N, $Ti_{1-x}Cr_xN$ и металлического Ni. При дальнейшем увеличении концентрации Ni в покрытии образуется интерметаллид Ni_3Ti. Методом просвечивающей электронной микроскопии изучена структура покрытий. Для покрытий системы Ti–Cr–N характерно столбчатое строение структуры, в столбцах которой, вследствие полной растворимости TiN и Cr_2N и планетарного вращения подложек, приводящего к послойной укладке компонентов испаряемых катодов, образуются субслои $Ti_{1-x}Cr_xN$ и $Ti_{1-y}Cr_yN$ ($x > y$) толщиной несколько нанометров с переменной концентрацией титана и хрома и субслои Cr_2N порядка 25 нм. Данная структура сохраняется и для покрытий системы Ti–Cr–N–Ni с малой концентрацией никеля (порядка десятых долей ат. %). Однако при этом наблюдаются измельчение размера столбцов и рост двуосных сжимающих напряжений с 6,7 до 9,7 ГПа, что приводит к повышению твердости от 30 до 42 ГПа. Для покрытий с высоким содержанием никеля характерна многослойная архитектура с равноосной поликристаллической структурой нанозерен в слоях. По мере увеличения концентрации Ni твердость покрытия снижается до 16,7 ГПа, что связано с возрастанием доли относительно мягкого никеля в покрытии и уменьшением величины макронапряжений до –0,6 ГПа. При этом интенсивность изнашивания увеличивается с $3\cdot10^{-15}$ до $5\cdot10^{-15}$ $м^3/(Н\cdot м)$. Исследуемые покрытия систем Ti–Cr–N и Ti–Cr–N–Ni обладают стойкостью к адгезионному и когезионному разрушению. С ростом содержания никеля при измерительном царапании разрушение покрытий происходит исключительно вследствие пластического деформирования.

Ключевые слова: керамические покрытия, керамикометаллические покрытия, износостойкость, трибология, нитриды, твердость

Благодарности: Исследование выполнено за счет гранта Российского научного фонда № 19-19-00555, https://rscf.ru/project/19-19-00555/

Авторы выражают благодарности доктору технических наук Ф.В. Кирюханцеву-Корнееву (НИТУ МИСИС) за помощь в проведении исследований по жаростойкости покрытий.

Для цитирования: Черногор А.В., Блинков И.В., Белов Д.С., Сергевнин В.С., Демиров А.П. Влияние никеля на состав, структуру и свойства покрытий Ti–Cr–N. *Известия вузов. Порошковая металлургия и функциональные покрытия*. 2023;17(1):64–74. https://doi.org/10.17073/1997-308X-2023-1-63-74

Introduction

At present, the studies of strengthening and friction-adjustable coatings are focused on their development based on multiphase systems, in which the presence of various elements and phases significantly changes the properties compared to two-component coatings [1–5]. Systems based on transition metal nitrides are characterized by enhanced mechanical properties. Thus, three-component systems Ti–Cr–N, Cr–Mo–N, and Ti–Mo–N are significantly superior to two-component systems *Me*–N in their hardness, tribological properties, and heat resistance [3; 5–9]. Ti–Cr–N–Ni based coatings, in which chromium and titanium based nitride phases provide a combination of heat resistance [10] and high hardness [5; 7], are of interest. Due to the refinement of the nitride phase and the formation of a dispersion-hardened structure with a plastic nickel frame, the introduction of metals with low affinity for nitrogen and limited solubility in them, for instance, nickel, into nitride coatings contributes to the formation of a material with high viscosity combined with hardness [11]. The improved performance properties of these coatings will be largely determined by the capability of controlling the composition and structure of the deposited material.

An analysis of the literary sources reveals the absence of studies in this field for coatings of Ti–Cr–N–Ni systems. In this regard, the goal was set to study the influence of nickel on the processes of structure formation, phase formation and the properties of these coatings.

Research Methods

The coatings were deposited on VK6 alloy substrates by arc-PVD method using a three-cathode vacuum-arc ion-plasma unit equipped with two magnetic drop fraction separators. The planetary rotation of the substrate holders ensures the formation of a coating with a two-level structure, including the layers obtained by rotating the substrate holders around the table axis, and the sublayers several nanometers thick with a well-defined interface, which are formed due to the rotation of the substrate holders around their axis [12]. The current strength of the arc evaporating the cathodes was determined on the basis of its value ensuring stable arc burning and the absence of a considerable amount of the droplet phase in the formed plasma flow. The current strength during the evaporation of TiNi, Cr, and Ti cathodes was 120, 120 and 130 A, respectively. All coatings were deposited for 90 min at a negative bias potential $U_b = 120$ V applied to the substrate and partial pressures of nitrogen and argon of 0.8 and 0.6 Pa, respectively.

X-ray phase analysis (XPA) was conducted using “D8 Discover” unit (Bruker AXS, Germany) with copper radiation. The survey was performed by sliding beam method at 2θ = 3° and a step of 0.01°. The macrostressed state of the coatings was studied by $\sin^2\psi$ method. The binding energy and composition of the coatings were investigated by *X*-ray photoelectron spectroscopy (XPS) using "VersaProbeII" unit (ULVAC-PHI Inc., the USA). Photoemission was excited in monochrome radiation AlK_α with a power of 25 W and a beam diameter of 100 μm. The spectral data were collected at an analyzer transmission energy of 11.75 eV and a data collection density of 0.1 eV per step. Furthermore, the concentration profiles of the coatings obtained by sequential ion (Ar) etching at a rate of 9.4 nm/min at an ion energy of 2 keV and a raster of 2×2 mm were also examined.

The elemental composition, surface morphology of the coatings prior to and after the oxidation, and the wear track after tribological researches were studied using a JSM-7600F scanning electron microscope with JED-2300F attachment for energy-dispersive spectrometry (JEOL, Japan). The heat resistance of the coatings was evaluated by the depth of oxygen penetration into the samples of coated hard alloys. The concentration profiles of the elements along the thickness of the samples after oxidative annealing were determined bythe method of glow discharge optical emission spectroscopy (GDOES). The studies were performed using "Profiler 2" device (Horiba Jobin Yvon, France). The resolution for the concentration of chemical elements contained in the coating was 0.01 at. %.

The structure of the coatings was studied using the high-resolution transmission electron microscope (TEM) JEM 2100 (JEOL, Japan). Thin coating lamellae obtained by ion etching were used as samples. Mechanical properties (hardness, Young's modulus, elastic and plastic deformation energy ratio) were measured during indentation using "CSM Micro-Hardner Tester" (CSM Instruments SA, Switzerland). The scratching of coated samples was measured using the Revetest scratch tester as per the "Methodology for Measuring Adhesion and Cohesion Strength with the Revetest Scratch Tester, available from CSM (Switzerland) MVI AKP/09" (FR.1.28.2010.07503). The friction coefficient and wear were measured using "Tribometer T50" unit (Nanovea, the USA) using the *pin-on-disk* method with Al_2O_3 counterbody, a load of 5 N, a speed of 0.1 m/s, and a track radius of 6 mm. The friction track profile was determined using the WYKO NT1100 optical profilometer (Veeco, the USA).

Results and Discussion

The elemental composition of the obtained coatings is shown in the Table. The change in the composition was achieved by different arrangement of the used cathodes (TiNi, Cr and Ti) in the corresponding evaporation blocks of the unit, taking into account the fact that up to 80 % of the evaporated material vanishes in them, in the presence of magnetic separators [12].

In the paper, the resulting coatings were designated as $Ti_xCr_{1-x}N_y$–zNi, where x is the relative concentration of chromium obtained from the ratio of the concentration of chromium to the sum of the concentrations of chromium and titanium, rel. units; y is the relative nitrogen concentration obtained from the ratio of nitrogen concentration to the sum of chromium and titanium concentrations, rel. units; z is absolute nickel concentration, at. %.

No nickel-containing phases were detected by the XPA for coatings of Ti–Cr–N–Ni systems with a nickel concentration up to 11.3 at. %. Upon that, according to XPS data, the binding energy of nickel photoelectrons in these coatings is approximately 852.4 eV, which shows the presence of the Ni metal phase only [13]. This is due to the fact that nickel is characterized by a low thermodynamic affinity for nitrogen and does not form a nitride phase in contrast to other elements of the coating [14–17]. Taking into account the low solubility of nickel in nitrides as well as the absence of its diffraction lines in the diffraction patterns, it can be

The elemental and phase composition of the coatings

Элементный и фазовый состав покрытий

Coating	Elemental composition, at. %				Phase composition
	Ti	Cr	Ni	N	
$Ti_{0.43}Cr_{0.57}N_{0.89}$	22.9	30.1	–	47	$Ti_xCr_{1-x}N$
$Ti_{0.34}Cr_{0.66}N_{0.75}$–0.1Ni	19.4	37.5	0.1	43	$Ti_xCr_{1-x}N$
$Ti_{0.15}Cr_{0.85}N_{0.51}$–8.7Ni	9.2	51.1	8.7	31	Ni, $Ti_xCr_{1-x}N$, Cr_2N
$Ti_{0.26}Cr_{0.74}N_{0.83}$–10.9Ni	12.4	36.3	10.3	41	$Ti_xCr_{1-x}N$, Ni
$Ti_{0.25}Cr_{0.75}N_{0.76}$–11.3Ni	12.5	37.2	11.3	39	$Ti_xCr_{1-x}N$, Ni
$Ti_{0.72}Cr_{0.28}N_{1.84}$–13.8Ni	21.7	8.6	13.7	56	Ni, Ni_3Ti, $Ti_xCr_{1-x}N$
$Ti_{0.94}Cr_{0.06}N_{0.70}$–36.8Ni	33.4	1.9	36.7	28	Ni, Ni_3Ti, $Ti_xCr_{1-x}N$

assumed that the coating contains nickel in *X*-ray amorphous state that corresponds to the results presented in the paper [11].

XPS spectra obtained using layer-by-layer etching method exhibit the formation of a solid solution of a complex nitride for Ti–Cr–N coating (Fig. 1). The binding energies of N1*s* and Ti2*p*3/2 are within the range of values characteristic of titanium nitride (396.6 and 455.5 eV, respectively [18]). The binding energy of Cr2*p*3/2 decreases from 575.5 to 574.5 eV as the concentration of Ti increases (the binding energy of Cr2*p*3/2 for CrN compound is 575.8 eV, it is 576.1 eV for Cr_2N, and 574.0 eV for metallic Cr [19]). The change in the binding energy of photoelectrons of chromium depending on its concentration and the concentration of titanium in solid solution is caused by an increase in metallic bond fraction in the complex nitride (Cr, Ti)N [20]. Its formation is possible as a result of the close crystallographic parameters of titanium and chromium nitrides as well as their high mutual solubility [21; 22].

For Ti–Cr–N–Ni coatings with a concentration of no more than 11.3 at. % Ni, the binding energies of Cr2*p*3/2 and Ti2*p*3/2 in layers enriched with chromium (line *1* in Fig. 2) are 574.4 and 455.5 eV. Since the diffraction lines of Cr_2N and metallic Cr were not detected in the diffraction patterns of coatings of these compositions, the shift of Cr2*p*3/2 spectrum towards lower energy is caused by a phenomenon similar to coatings of Ti–Cr–N system, i.e. the formation of a complex nitride. Upon that, according to the XPS spectra of nitrogen, the binding energy of N1*s* (397.2 eV) is higher than that in nitrides of stoichiometric composition TiN and CrN (396.6 eV [19]) that exhibits the nonstoichiometric nature of Ti and Cr nitrides and is confirmed by N/(Ti + Cr) ratio, lying within the range from 0.75 to 0.83.

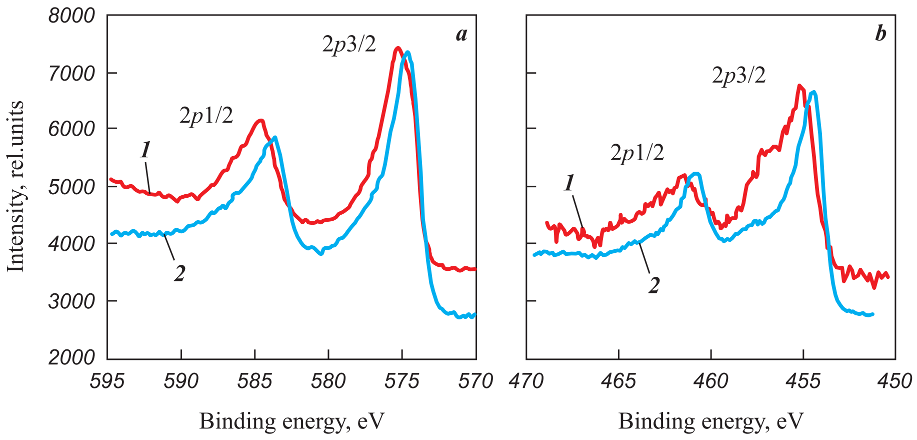

Fig. 1. XPS spectra of Cr2*p* (***a***) and Ti2*p* (***b***) in $Ti_{0.43}Cr_{0.57}N_{0.89}$ coating in the areas with Cr and Ti concentrations of 44 and 8 at. % (***1***), and 22 and 26 at. % (***2***), correspondingly

Рис. 1. РФЭ-спектры Cr2*p* (***a***) и Ti2*p* (***b***) в покрытии $Ti_{0,43}Cr_{0,57}N_{0,89}$ в областях с концентрациями Cr и Ti соответственно 44 и 8 ат. % (***1***) и 22 и 26 ат. % (***2***)

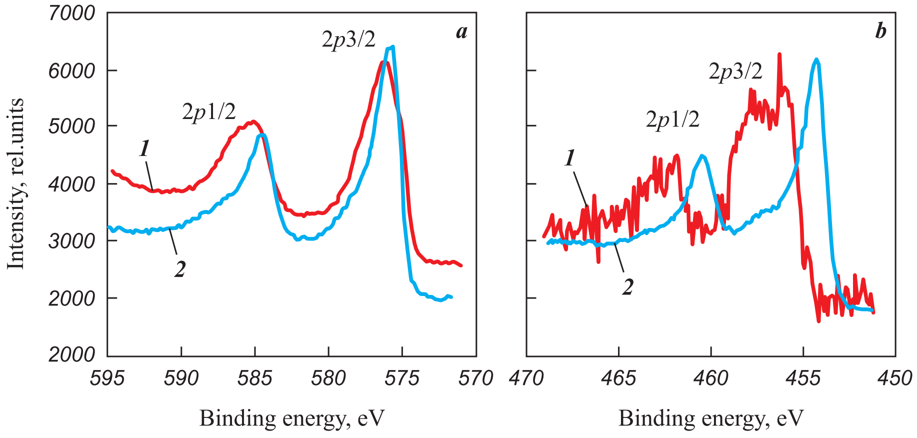

Fig. 2. XPS spectra of Cr2*p* (***a***) and Ti2*p* (***b***) in $Ti_{0.34}Cr_{0.66}N_{0.75}$–0.1Ni coatings in the areas with Cr) and Ti concentrations of 47 and 8 at. % (***1***), and 25 and 24 at. % (***2***), correspondingly

Рис. 2. РФЭ-спектры Cr2*p* (***a***) и Ti2p (***b***) *в* покрытиях $Ti_{0,34}Cr_{0,66}N_{0,75}$–0,1Ni в областях с концентрациями Cr и Ti соответственно 47 и 8 ат. % (***1***) и 25 и 24 ат. % (***2***)

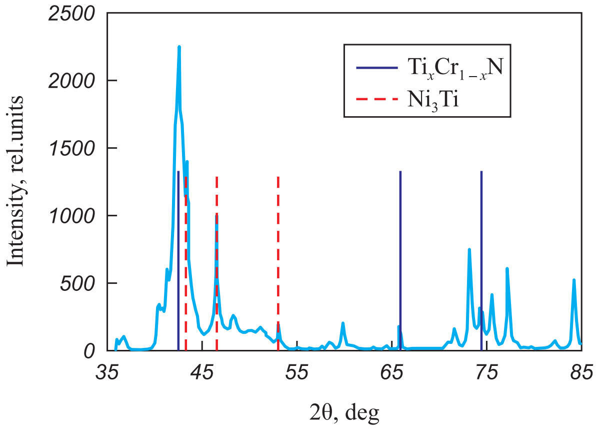

Fig. 3. The diffraction pattern of $Ti_{0.72}Cr_{0.28}N_{1.84}$–13.8Ni coatings

Рис. 3. Дифрактограмма покрытий $Ti_{0,72}Cr_{0,28}N_{1,84}$–13,8Ni

With an increase in the nickel concentration above 13 at. % in the coating, intermetallic Ti_3Ni is formed along with $Ti_xCr_{1-x}N$ solid solution and metallic nickel, as can be seen in the diffraction pattern for $Ti_{0.72}Cr_{0.28}N_{1.84}$–13.8Ni coatings (Fig. 3).

The increase of the nickel concentration in Ti–Cr–N–Ni coatings is accompanied by a change in their morphology (Fig. 4). The coatings with a nickel concentration of less than 13.8 at. % are characterized by a dense cellular surface, the formation of which is caused by the replica of the substrate surface by the coating. With increasing Ni concentration, the coatings turn loose and rough due to the formation of a large amount of the droplet phase, which poorly wets the nitrides [11].

According to TEM data (Fig. 5), nickel also affects the coating structure. Thus, for Ti–Cr–N systems, the coatings exhibit a columnar structure with a column size of about 400–500 nm (Fig. 5, *a*). The introduction of nickel into this system at concentrations up to 3 at. % causes the refinement of the structure, which is still characterized by well-defined columns elongated in the direction of coating growth, about 220–300 nm in size (Fig. 5, *b*). Upon that, the TEM images for these samples clearly show that the columns consist of sublayers with a thickness ranging from several nanometers to 25 nm. According to the modeling of plasma mass trans-

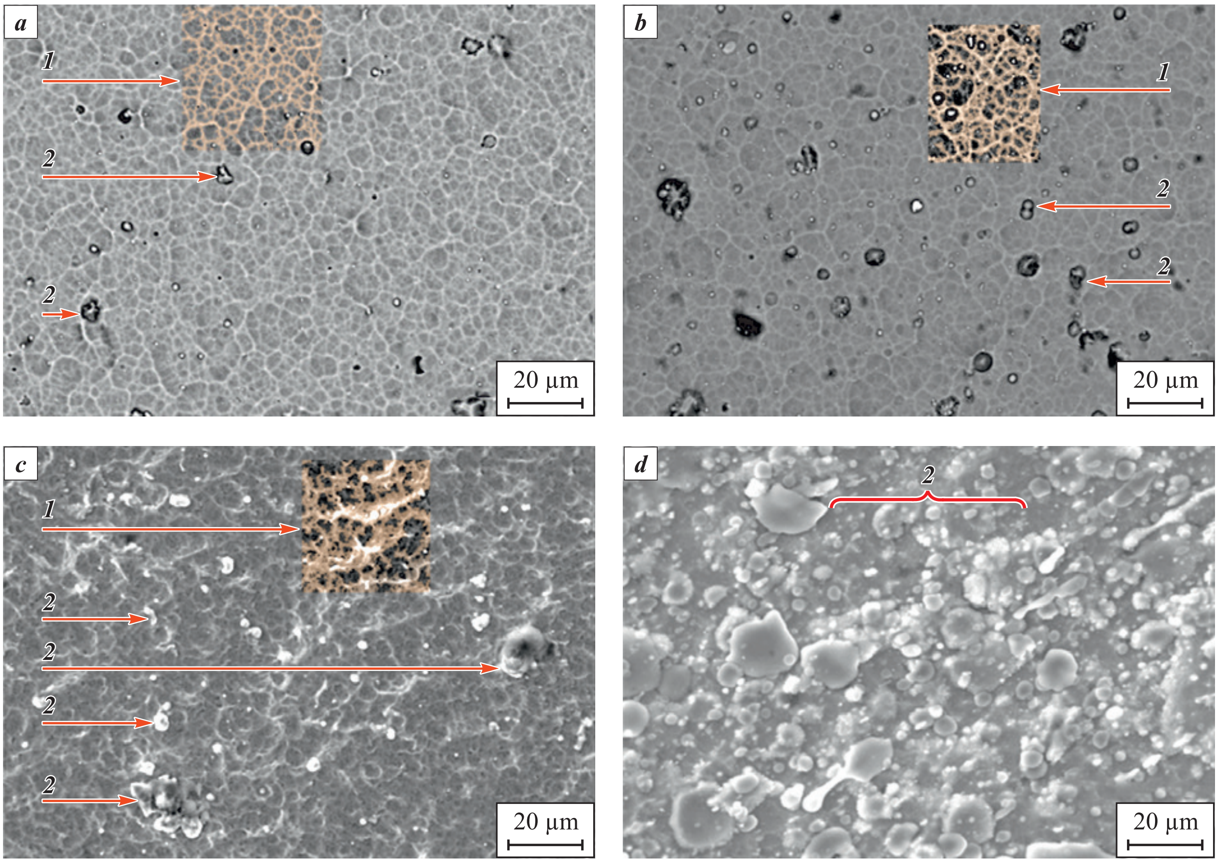

Fig. 4. The morphology of coatings of Ti–Cr–N and Ti–Cr–N–Ni systems
a – $Ti_{0.43}Cr_{0.57}N_{0.89}$, ***b*** – $Ti_{0.34}Cr_{0.66}N_{0.75}$–0.1Ni, ***c*** – $Ti_{0.15}Cr_{0.85}N_{0.51}$–8.7Ni, ***d*** – $Ti_{0.94}Cr_{0.06}N_{0.70}$–36.8Ni
1 – the elements of the cellular structure of the surface, ***2*** – droplet phase

Рис. 4. Морфология покрытий систем Ti–Cr–N и Ti–Cr–N–Ni
a – $Ti_{0,43}Cr_{0,57}N_{0,89}$, ***b*** – $Ti_{0,34}Cr_{0,66}N_{0,75}$–0,1Ni, ***c*** – $Ti_{0,15}Cr_{0,85}N_{0,51}$–8,7Ni, ***d*** – $Ti_{0,94}Cr_{0,06}N_{0,70}$–36,8Ni
1 – элементы ячеистой структуры поверхности, ***2*** – капельная фаза

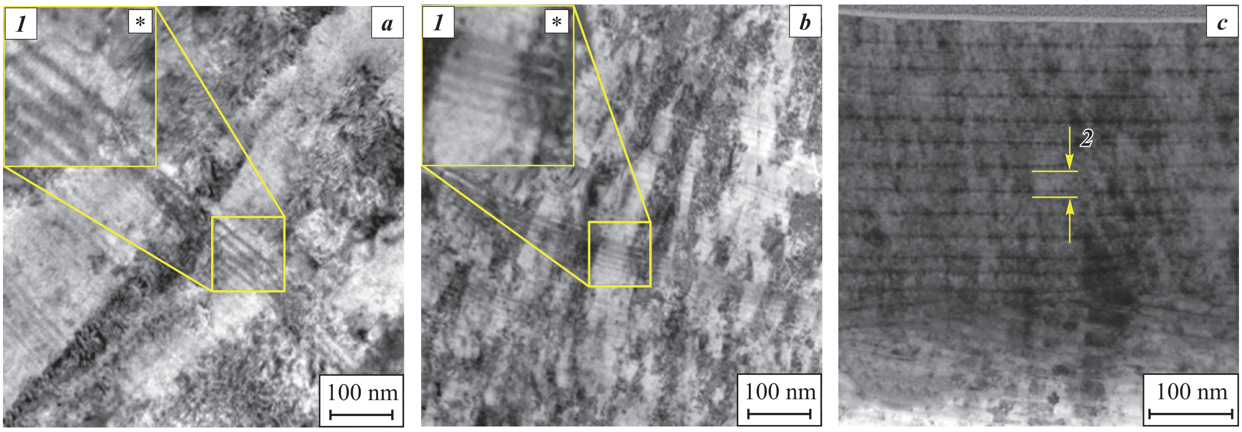

Fig. 5. The TEM image of the cross section of Ti–Cr–N–Ni coatings formed at U_b = 120 V
a – $Ti_{0.43}Cr_{0.57}N$, ***b*** – $Ti_{0.34}Cr_{0.66}N$–0.1Ni, ***c*** – $Ti_{0.26}Cr_{0.74}N$–10.9Ni
1 – sublayers in column volume, ***2*** – modulation period

Рис. 5. ПЭМ-изображение поперечного сечения покрытий Ti–Cr–N–Ni, сформированных при U_b = 120 В
a – $Ti_{0,43}Cr_{0,57}N$, ***b*** – $Ti_{0,34}Cr_{0,66}N$–0,1Ni, ***c*** – $Ti_{0,26}Cr_{0,74}N$–10,9Ni
1 – субслои в объеме столбцов, ***2*** – период модуляции

fer and the growth of coatings of these systems [23], they are caused by planetary rotation of substrates relative to evaporating cathodes and consist of solid solutions of variable concentrations of titanium and chromium ($Ti_{1-x}Cr_xN$ and $Ti_{1-y}Cr_yN$ ($x > y$)) and Cr_2N. With a subsequent increase in the nickel concentration up to 12 at.%, the coatings are already characterized by a multilayer polycrystalline architecture with a modulation period of 25 nm and an average grain size of 18 nm (Fig. 5, *c*). These results may show that, due to the low solubility of nickel in nitrides, it prevents their growth, refines the structure, and changes the architecture of the coatings.

$Ti_{0.43}Cr_{0.57}N_{0.89}$ and $Ti_{0.34}Cr_{0.66}N_{0.75}$–0.1Ni coatings are characterized by high compressive macrostresses, being 6.7 and 9.7 GPa, respectively. It is known that compressive macrostresses for nitride coatings obtained by the method of ion-plasma vacuum-arc deposition can range from 4 to 12 GPa. The formation of such a “highly stressed” structure is associated, first of all, with its defectiveness: during the deposition of coatings, the flow of high-energy particles bombarding the surface contributes to the appearance of a large number of point and linear defects [24]. The introduction of nickel increases the magnitude of macrostresses due to the refinement of nitride grains, bearing in mind that an increase in the interface length leads to an increase in the number of grain boundary defects. For coatings with a high nickel content (>12 at. %), there is a significant decrease in macrostresses due to the effect of their relaxation caused by plastic deformation of nickel in the field of emerging stresses.

The thermal stability of the composition and structure of the coatings was studied after their high-temperature annealing in vacuum at temperatures of 650 and 850 °C. For Ti–Cr–N and Ti–Cr–N–Ni samples with a low nickel content, it is typical (Fig. 6) that the diffraction lines corresponding to TiCrN compound split into TiN and CrN during the annealing. This is most likely due to the dissolution of the adjacent sublayers $Ti_{1-x}Cr_xN$ and $Ti_{1-y}Cr_yN$ ($x > y$) with different concentrations of titanium and chromium, thus forming solid solutions of average composition enriched with titanium and chromium, which we observe in the diffraction patterns. These conclusions are also confirmed by the TEM images (Fig. 7), demonstrating an increase in the average grain size after the annealing.

According to the XPS data, during oxidative annealing of $Ti_{0.43}Cr_{0.57}N_{0.89}$ coatings with a chromium concentration of 27 at. % at t = 800 °C, Cr_2O_3 and TiO_2 phases are formed, the oxygen concentration in the coating is ~4÷5 at. % with an oxidized layer thickness of about 0.25 μm (Fig. 8). Upon that, the coating remains intact. With an increase in the oxidation temperature to 850 °C, the oxygen content in the coating of this composition increases to ~19 at. %. Taking into account considerable differences in the molar volumes of titanium oxide and nitride, the surface layer of the coating becomes loose, its barrier functions with respect to oxygen decrease, the depth of oxygen penetration into the coating reaches 0.8 μm, as evidenced by the data of GDOES (Fig. 9). The analysis of the surface of the coatings by SEM method (Fig. 9) in this case demonstrated the destructive oxidation of samples of this composition, which is characterized by a local breaking of the coating to the substrate.

As the chromium concentration increases to 36 at. %, the fraction of oxygen in the coating after oxidative annealing at t = 850 °C decreases to 14 at. % with a decrease in the depth of the oxidized layer to 0.4 μm, but

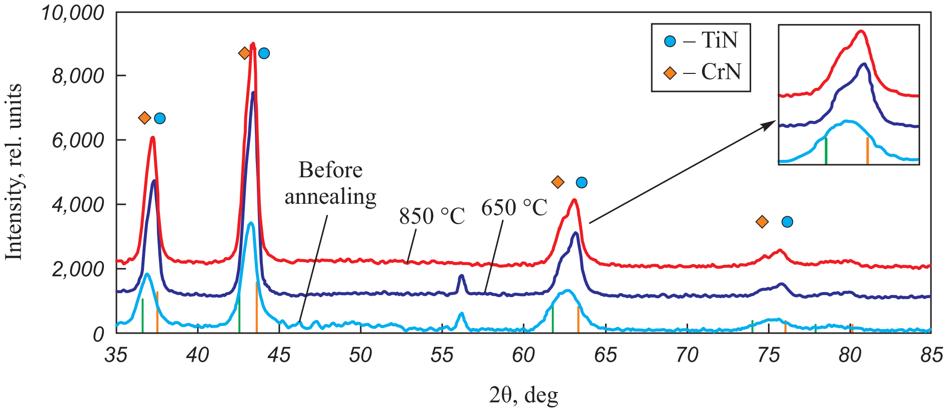

Fig. 6. The diffraction patterns of Ti–Cr–N coatings prior to and after the annealing

Рис. 6. Дифрактограммы покрытий Ti–Cr–N до и после отжига

the areas of local breaking of the coating to the substrate are still observed on the surface of the samples (Fig. 10).

The microindentation method was used to obtain data on the hardness of the studied coatings (Fig. 11), according to which $Ti_{0.34}Cr_{0.66}N_{0.75}$–0.1Ni coatings are characterized by the highest hardness (about 42 GPa), which can be explained by a high level of compressive macrostresses [25], being 9.7 GPa. With an increase in the nickel concentration, the hardness of the coatings decreases to 16 GPa (with a nickel content of 13.8 at. %), which is associated with an increased concentration of plastic metal phase Ni in the coating composition.

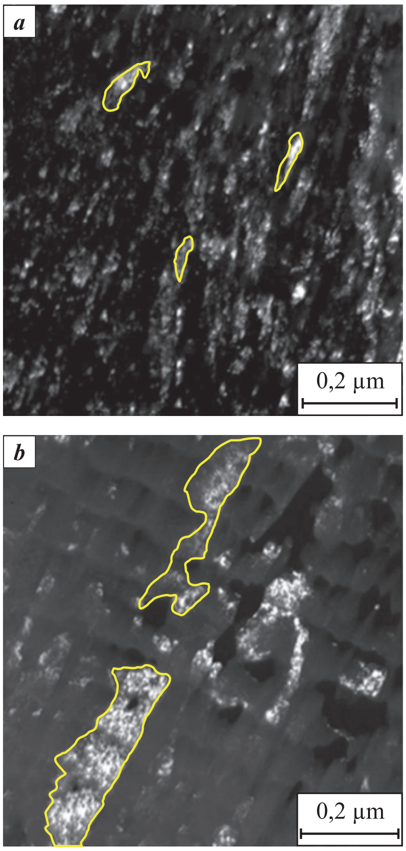

Fig. 7. The TEM images of the structure of Ti–Cr–N–Ni samples priot to (***a***) and after (***b***) the annealing
The coating grains elongated in the direction of growth are identified

Рис. 7. ПЭМ-изображения структуры образцов Ti–Cr–N–Ni до (***a***) и после (***b***) отжига
Выделены вытянутые в направлении роста зерна покрытий

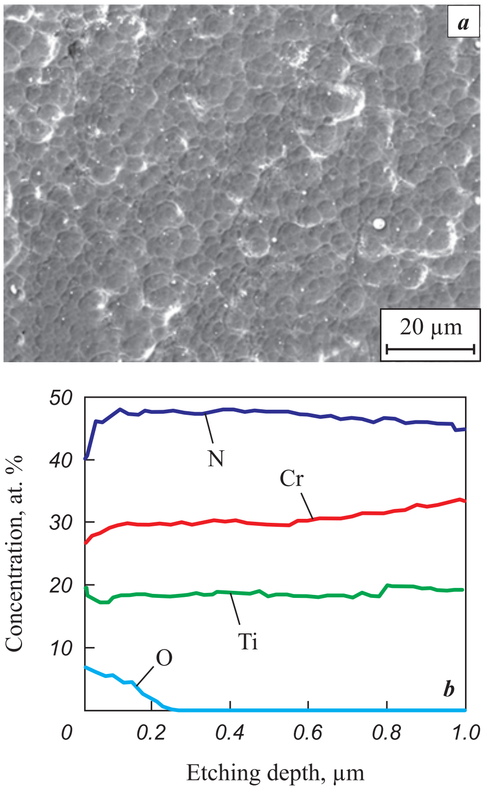

Fig. 8. The image of the surface (***a***) and the concentration profile of the distribution of elements (***b***) in $Ti_{0.43}Cr_{0.57}N_{0.89}$–0.1Ni coating after oxidative annealing at $t = 800$ °C

Рис. 8. Изображение поверхности (***a***) и концентрационный профиль распределения элементов (***b***) в покрытии $Ti_{0,43}Cr_{0,57}N_{0,89}$–0,1Ni после окислительного отжига при $t = 800$ °C

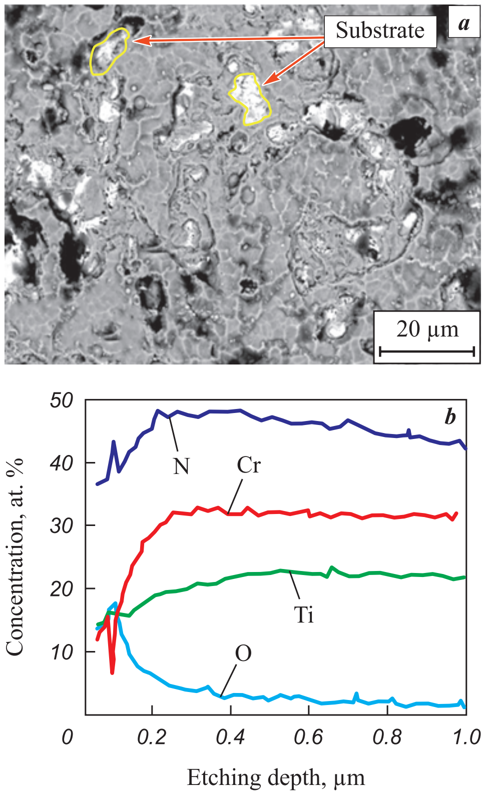

Fig. 9. The image of the surface (***a***)
and the concentration profile of the distribution of elements (***b***)
in $Ti_{0.43}Cr_{0.57}N_{0.89}$–0.1Ni coating
after oxidative annealing at t = 850 °C

Рис. 9. Изображение поверхности (***а***)
и концентрационный профиль распределения элементов (***b***)
в покрытии $Ti_{0,43}Cr_{0,57}N_{0,89}$–0,1Ni
после окислительного отжига при t = 850 °C

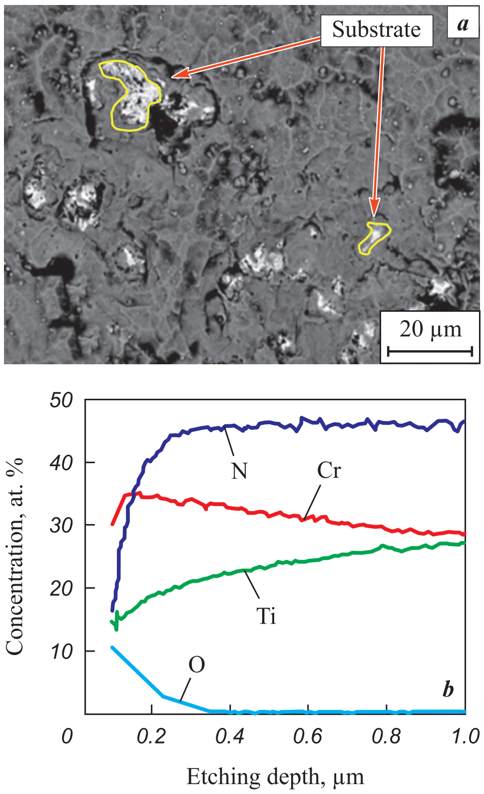

Fig. 10. The image of the surface (***a***)
and the concentration profile of the distribution of elements (***b***)
in $Ti_{0.34}Cr_{0.66}N_{0.75}$–0.1Ni coating
after oxidative annealing at t = 850 °C

Рис. 10. Изображение поверхности (***а***)
и концентрационный профиль распределения элементов (***b***)
в покрытии $Ti_{0,34}Cr_{0,66}N_{0,75}$–0,1Ni
после окислительного отжига при t = 850 °C

The results of scratch measurements (Figs. 12 and 13) indicate that up to a load of 75 N, the coatings of Ti–Cr–N and Ti–Cr–N–Ni systems (1 at. % Ni) do not exhibit any chips and cracks in the scratch body, the wear of the coating lies in partial abrasion of the protruding irregularities of the coating and plastic pressing of material out of the scratch body. When a load of 75 N is reached, cracks begin to form at the bottom of the scratch (Lc1), which is accompanied by a drastic increase in the amplitude of acoustic emission, and at a load of ~85÷87 N (Lc3), a local appearance of the substrate occurs. Such a high fracture toughness and wear resistance during measuring scratching testify to the high cohesive strength of the coatings and their adhesion to the substrate, as determined by the high values of compressive stresses realized in the coatings [26].

An increase in the plasticity of Ti–Cr–N–Ni coating material upon the growth of Ni concentration results in a considerable change in the nature of its destruction during scratching. The coating is destroyed through plastic deformation in the entire range of applied loads in the absence of cracking. This is evidenced by the acoustic emission data and visual observations of the scratch (Fig. 14). The destruction of the coa-

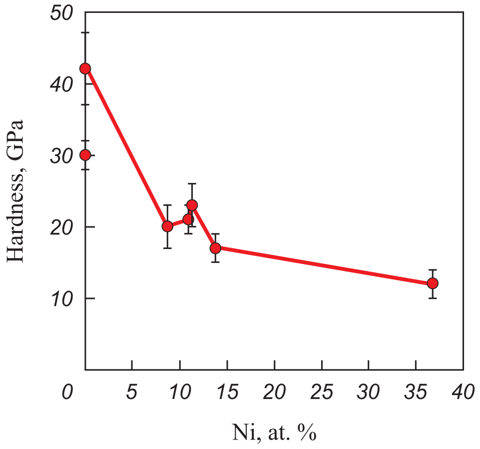

Fig. 11. The influence of nickel concentration
on the hardness of Ti–Cr–N–Ni coatings

Рис. 11. Влияние концентрации никеля
на твердость покрытий Ti–Cr–N–Ni

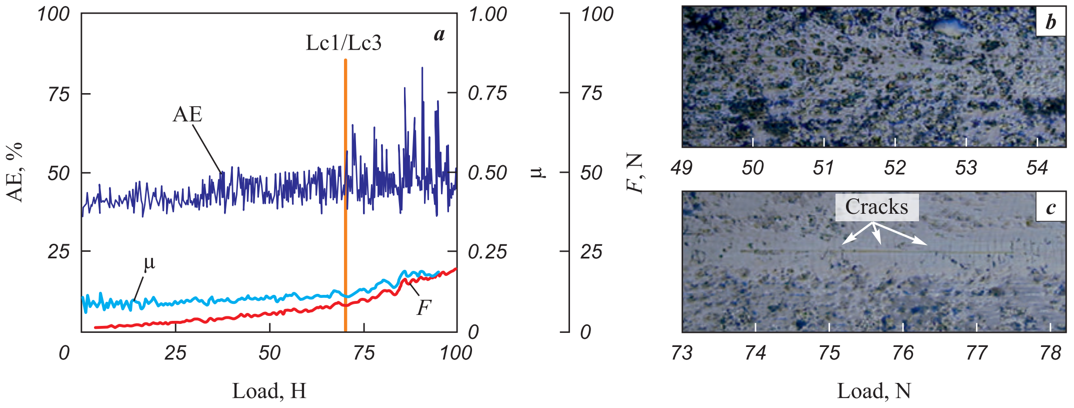

Fig. 12. The dependence of acoustic emission (AE), friction force (F) and friction coefficient (μ) on the load upon measuring scratching (***a***) and scratch images (***b***, ***c***) for $Ti_{0.43}Cr_{0.57}N_{0.89}$ coatings

Рис. 12. Зависимость акустической эмиссии (АЭ), силы трения (F) и коэффициента трения (μ) от нагрузки при измерительном царапании (***a***) и изображения царапины (***b***, ***c***) для покрытий $Ti_{0,43}Cr_{0,57}N_{0,89}$

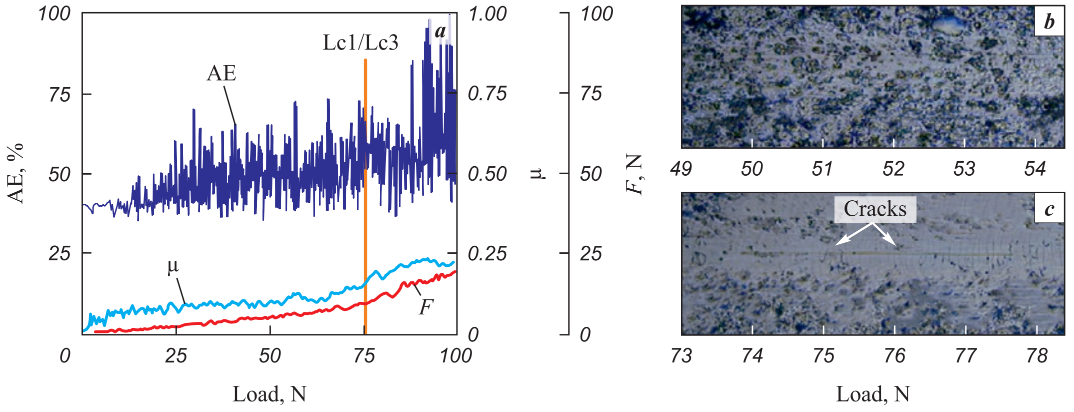

Fig. 13. The dependence of acoustic emission (AE), friction force (F) and friction coefficient (μ) on the load upon measuring scratching (***a***) and scratch images (***b***, ***c***) for $Ti_{0.34}Cr_{0.66}N_{0.75}$–0.1Ni coatings

Рис. 13. Зависимость акустической эмиссии (АЭ), силы трения (F) и коэффициента трения (μ) от нагрузки при измерительном царапании (***a***) и изображения царапины (***b***, ***c***) для покрытий $Ti_{0,34}Cr_{0,66}N_{0,75}$–0,1Ni

ting occurs through the pressing of the material out of the scratch body. At loads on the indenter of more than 90 N, the coating remains intact. This type of destruction is attributed to the influence of the plastic component in its composition (Ni) on the relaxation of stresses arising in the coating during scratching.

Upon the introduction of 0.1 at. % of nickel into Ti–Cr–N coatings, the friction coefficient increases from 0.6 to 0.7 (Fig. 15). A decrease in the wear resistance of coatings is not observed, and the wear intensity is approximately $2.5\cdot10^{-15}$ m^3/(N·m). The growth of the friction coefficient is associated with an increase in the hardness of coatings (from 30 to 42 GPa) and a decrease in their fracture toughness, as evidenced by a decrease in plastic deformation ratio (from 67 to 40 %), determined by indentation of the coating material.

As the nickel concentration in the coatings increases from 8.7 to 11.8 at. %, the wear coefficient increases from $3\cdot10^{-15}$ to $4.8\cdot10^{-15}$ m^3/(N·m), respectively. This is attributed to the relatively low hardness of the coatings.

Conclusion

Ti–Cr–Ni–N coatings obtained by arc-PVD method are composed of Cr_2N, $Ti_{1-x}Cr_xN_y$ nitrides and metallic Ni. The formation of nickel based intermetallic compounds is observed only at its concentration in the coating above 11 at. %.

The planetary rotation of the coated samples and the mutual solubility of chromium and titanium nitrides result in the formation of a complex architecture of coatings with the nickel content of tenths of at. %, consisting of columnar grains $Ti_{1-x}Cr_xN_y$, including sublayers, being several nanometers thick, which are made of Ti–Cr–N solid solution of variable composition and the sublayers of Cr_2N, being about 25 nm thick. As the nickel content in the structure of

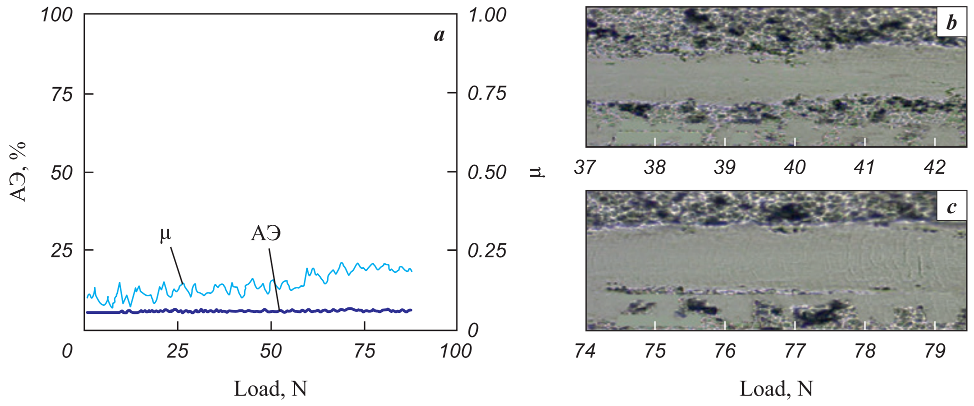

Fig. 14. The dependence of acoustic emission (AE) and friction coefficient (μ) on the load upon measuring scratching (***a***) and scratch images (***b***, ***c***) for $Ti_{0.25}Cr_{0.75}N_{0.76}$–11.3Ni coatings

Рис. 14. Зависимость акустической эмиссии (АЭ) и коэффициента трения (μ) от нагрузки при измерительном царапании (***a***) и изображения царапины (***b***, ***c***) для покрытий $Ti_{0,25}Cr_{0,75}N_{0,76}$–11,3Ni

Ti–Cr–Ni–N coatings increases, a multilayer architecture is formed.

The introduction of nickel into Ti–Cr–N coatings, resulting in the refinement of the grain structure of the nitride phase, is accompanied by an increase in compressive macrostresses from 6.7 to 9.7 GPa (at a nickel content of the order of tenths of at. %). With a further increase in its concentration, the values of compressive macrostresses decrease to 0.6 GPa, which may be caused by their relaxation through the process of plastic deformation of metallic nickel in the stress fields.

It has been established that coatings based on Ti–Cr–Ni–N multicomponent system exhibit the following properties, depending on the nickel content: hardness of 42–16 GPa; fracture toughness, characterized by the relative energy of plastic deformation, of 50–65 %; wear intensity being up to 10^{-15} $m^3/(m\cdot N)$; adhesive strength with substrate (Lc3) being over 75–80 N, heat resistance being up to 850 °C. The coatings of this composition have shown high efficiency for wear protection in sea water of a steel (20Х13) liner paired with carbon fiber in sliding-surface bearings used in the friction units of ship mechanisms [27].

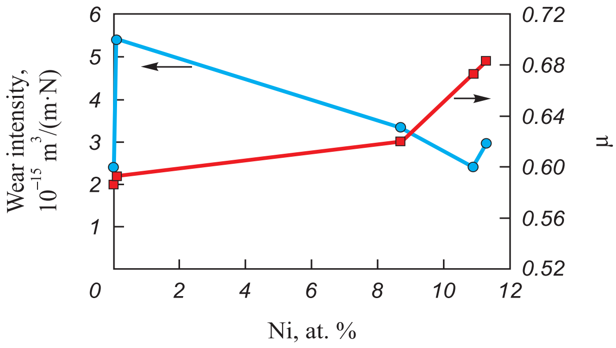

Fig. 15. The influence of nickel concentration on the tribological properties of the Ti–Cr–Ni–N coatings

Рис. 15. Влияние концентрации никеля на трибологические свойства покрытий Ti–Cr–Ni–N

References / Список литературы

1. Martin P. Handbook of deposition technologies for films and coatings: Science, applications and technology. 3rd ed. Amsterdam: William Andrew, 2009. 936 p.
2. Kanoun M.B., Goumri-Said, Jacuen M. Structure and mechanical stability of molybdenum nitrides: A first-principles study. *Physical Review B*. 2007;76(13):1–4. https://doi.org/10.1103/PhysRevB.76.134109
3. Kazmanli M.K., Urgen M., Çakir A.F. Effect of nitrogen pressure, bias voltage and substrate temperature on the phase structure of Mo–N coatings produced by cathodic arc PVD. *Surface and Coatings Technology*. 2003;167(1): 77–82. https:// doi.org/10.1016/S0257-8972(02)00866-6
4. Gilewicz A., Warcholinski B., Murzynski D. The properties of molybdenum nitride coatings obtained by cathodic arc evaporation. *Surface and Coatings Technology*. 2013;236:149–158. https://doi.org/10.1016/j.surfcoat.2013.09.005
5. Kumar D.D., Kumar N., Kalaiselvam S. Micro-tribo-mechanical properties of nanocrystalline TiN thin films for small scale device applications. *Tribology International*. 2015; 88:25–30. https://doi.org/10.1016/j.triboint.2015.02.031
6. Vaz F., Ferreira J., Ribeiro E. Influence of nitrogen content on the structural, mechanical and electrical properties of TiN thin films. *Surface and Coatings Technology*. 2005;191:317–323.
7. Akbarzadeh M., Shafyei A., Salimijazi H.R. Characterization of TiN, CrN and (Ti, Cr)N coatings deposited by cathodic ARC evaporation. *International Journal of Engineering*. 2014;27(7):1127–1132.
8. Shan L., Wang Y., Li J.-L., Li H., Lu X., Chen J. Structure and mechanical properties of thick Cr/Cr_2N/CrN multilayer coating deposited by multi-arc ion plating. *Transactions of Nonferrous Metals Society of China*. 2015:25(4):1135–1143. https://doi.org/10.1016/S1003-6326(15)63708-6

9. Song G.-H., Luo Z., Li F., Chen L., He C. Microstructure and indentation toughness of Cr/CrN multilayer coatings by arc ion plating. *Transactions of Nonferrous Metals Society of China*. 2015;25(3):811–816.
https://doi.org/10.1016/S1003-6326(15)63667-6

10. Mayerhofer P.H., Willmann H., Mitterer C. Oxidation kinetics of sputtered Cr–N coatings. *Surface and Coatings Technology*. 2001;146–147:222–228.
https://doi.org/10.1016/S0257-8972(01)01471-2

11. Belov D.S., Blinkov I.V., Volkhonskii A.O. The effect of Cu and Ni on the nanostructure and properties of arc-PVD coatings based on titanium nitride. *Surface and Coatings Technology*. 2014;260:186–197.
https://doi.org/10.1016/j.surfcoat.2014.09.069

12. Chernogor A.V., Blinkov I.V., Belov D.S., Volhonksiy A.O. Analysis of the structure of multilayer nanocrystalline coatings based on plasma mass transfer parameters calculated by the Monte Carlo method. *Technical Physics Letters*. 2019;45(2):75–78.
https://doi.org/10.1134/S1063785019020056

13. Mauchamp N.A., Isobe M., Hamaguchi S. Evaluation of nickel self-sputtering yields by molecular-dynamics simulation. *Journal of Vacuum Science & Technology A*. 2021; 39(4):043005. https://doi.org/10.1116/6.0000979

14. Ferro R., Marazza R. The Mo–N (molybdenum–nitrogen) system. *Bulletin of Alloy Phase Diagrams*. 1980;1(2): 82–85. https://doi.org/10.1007/BF02881198

15. Okamoto H. N–Ti (nitrogen – titanium). *Journal of Phase Equilibria and Diffusion*. 2013;34(2):151–152.
https://doi.org/10.1007/s11669-012-0153-6

16. Frisk K. A thermodynamic evaluation of the Cr–N, Fe–N, Mo–N and Cr–Mo–N systems. *Calphad*. 1991;15(1): 79–106. https://doi.org/10.1016/0364-5916(91)90028-I

17. Guillermet A.F., Frisk K. Thermodynamic properties of ni nitrides and phase stability in the Ni–N system. *International Journal of Thermophysics*. 1991;12(2):417–431.
https://doi.org/10.1007/BF00500762

18. Wagner C.D., Naumkin A.V., Kraut-Vass A., Allison J.W., Powell C.J., Rumble J.R.Jr. *NIST standard reference database 20*. 2003;3:251–252.

19. Lippitz A., Hübert Th. XPS investigations of chromium nitride thin films. *Surface and Coatings Technology*. 2005 200(1–4):250–253.
https://doi.org/10.1016/j.surfcoat.2005.02.091

20. Kunchenko Yu.V., Kunchenko V.V., Neklyudov I.M. Multilayer Ti–Cr–N coatings produced by the vacuum-arc deposition. *Voprosy atomnoi nauki i tekhniki*. 2007;(2):203–214. (In Russ.).

Кунченко Ю.В., Кунченко В.В., Неклюдов И.М. Слоистые Ti–Cr–N покрытия, получаемые методом вакуумно-дугового осаждения. *Вопросы атомной науки и техники*. 2007;(2):203–214.

21. Huang Z., Yu H., Song C., Li S. Precipitation and mechanical property of V-alloyed steel: Role of cooling rate. *Steel Research International*. 2020;91(2):1900444.
https://doi.org/10.1002/srin.201900444

22. Qiu, Y., Gao L. Preparation and characterization of CrN/CN and nano-TiN/CN composites. *Journal of the American Ceramic Society*. 2005;88(2):494–496.
https://doi.org/10.1111/j.1551-2916.2005.00087.x

23. Chernogor A.V., Blinkov I.V., Belov D.S., Sergevnin V.S., Volkhonskii A.O. Analysis of the structure of multilayer nanocrystalline coatings based on plasma mass transfer parameters calculated by the Monte Carlo method. *Technical Physics Letters*. 2019;45(2):75–78.
https://doi.org/10.1134/S1063785019020056

Черногор А.В., Блинков И.В., Белов Д.С., Сергевнин В.С., Волхонский А.О. Анализ структуры многослойных нанокристаллических покрытий на основе параметров массопереноса плазмы, вычисленных методом Монте-Карло. *Письма в журнал технической физики*. 2019;45(3):16–19.
https://doi.org/10.21883/PJTF.2019.03.47265.17575

24. Petrov I., Hultman L., Barna P. Microstructural evolution during film growth. *Journal of Vacuum Science & Technology A*. 2003;21(5):S117–S128.
https://doi.org/10.1116/1.1601610

25. Veprek S., Veprek-Heijman G.J., Karvankova P. Different approaches to superhard coatings and nanocomposites. *Thin Solid Films*. 2005;476(1):1–29.
https://doi.org/10.1016/j.tsf.2004.10.053

26. Petrov Y., Borodin E., Cadoni E, Selyutina N.. Relaxation model for dynamic plastic deformation of materials. *EPJ Web of Conferences*. 2015;94:4039.
https://doi.org/10.1051/epjconf/20159404039

27. Sergevnin V.S., Anisimov A.V., Chernogor A.V., Volkhonskii A.O., Demirov A.P., Lishevich I.V., Sobolev M.Yu., Kayamutdinov Sh.D. Electrochemical stability of nitride coatings for a steel-carbon fiber tribopair under conditions of imitation of a marine environment. *Journal of Physics Conference Series*. 2021;1954(1):012040.
https://doi.org/10.1088/1742-6596/1954/1/012040

Information about the Authors

Alexey V. Chernogor – Junior Researcher of the Department of functional nanosystems and high-temperature materials of the National University of Science and Technology "MISIS" (NUST MISIS)
ORCID: 0000-0001-5385-5369
E-mail: avchernogor@gmail.com

Igor V. Blinkov – Dr Sci. (Eng.), Professor of the Department of functional nanosystems and high-temperature materials, NUST MISIS
ORCID: 0000-0001-8619-6259
E-mail: biv@misis.ru

Сведения об авторах

Алексей Витальевич Черногор – мл. науч. сотрудник кафедры функциональных наносистем и высокотемпературных материалов Национального исследовательского технологического университета «МИСИС» (НИТУ МИСИС)
ORCID: 0000-0001-5385-5369
E-mail: avchernogor@gmail.com

Игорь Викторович Блинков – д.т.н, профессор кафедры функциональных наносистем и высокотемпературных материалов, НИТУ МИСИС
ORCID: 0000-0001-8619-6259
E-mail: biv@misis.ru

Dmitry S. Belov – Cand. Sci. (Eng.), Senior Researcher of the Department of functional nanosystems and high-temperature materials, NUST MISIS
ORCID: 0000-0002-7053-5540
E-mail: dm.blv@yandex.ru

Viktor S. Sergevnin – Cand. Sci. (Eng.), Engineer of the Department of functional nanosystems and high-temperature materials, NUST MISIS
ORCID: 0000-0002-7053-5540
E-mail: v.s.sergevnin@gmail.com

Aleksandr P. Demirov – Assistant of the Department of functional nanosystems and high-temperature materials, NUST MISIS
ORCID: 0000-0002-5014-2993
E-mail: apdemirov@misis.ru

Дмитрий Сергеевич Белов – к.т.н., ст. науч. сотрудник кафедры функциональных наносистем и высокотемпературных материалов, НИТУ МИСИС
ORCID: 0000-0002-7053-5540
E-mail: dm.blv@yandex.ru

Виктор Сергеевич Сергевнин – к.т.н., инженер кафедры функциональных наносистем и высокотемпературных материалов, НИТУ МИСИС
ORCID: 0000-0002-7053-5540
E-mail: v.s.sergevnin@gmail.com

Александр Павлович Демиров – ассистент кафедры функциональных наносистем и высокотемпературных материалов, НИТУ МИСИС
ORCID: 0000-0002-5014-2993
E-mail: apdemirov@misis.ru

Contribution of the Authors

A. V. Chernogor – formation of the basic concept, statement of the purpose and objectives of the study, preparation of the text, formulation of conclusions, conducting experiments on deposition of coatings.
I. V. Blinkov – scientific guidance, text editing and conclusions.

D. S. Belov – analysis of research results, preparation of illustrative material, conducting experiments to study the physicomechanical properties of coatings.
V. S. Sergevnin – carrying out tribological studies of samples with coatings.
A. P. Demirov – conducting research on the structure and composition of coatings, providing resources.

Вклад авторов

А. В. Черногор – формирование основной концепции, постановка цели и задачи исследования, подготовка текста, формулирование выводов, проведение экспериментов по осаждению покрытий.
И. В. Блинков – научное руководство, редактирование текста и выводов.
Д. С. Белов – анализ результатов исследований, подготовка иллюстративного материала, проведение экспериментов по изучению физико-механических свойств покрытий.
В. С. Сергевнин – проведение трибологических исследований образцов с покрытиями.
А. П. Демиров – проведение исследований структуры и состава покрытий, обеспечение ресурсами.

Received 27.07.2022
Revised 07.11.2022
Accepted 10.11.2022

Статья поступила 27.07.2022 г.
Доработана 07.11.2022 г.
Принята к публикации 10.11.2022 г.

Application of Powder Materials and Functional Coatings
Применение порошковых материалов и функциональных покрытий

UDC 621.762

https://doi.org/10.17073/1997-308X-2023-1-75-84

Research article
Научная статья

Comparative analysis of the tool life of submicron hard alloy WC–10Co sintered from powder obtained by electro discharge in oil

M. I. Dvornik, N. M. Vlasova

Institute of Materials Science of the Khabarovsk Federal Research Center
of the Far Eastern Branch of the Russian Academy of Sciences
153 Tikhookeanskaya Str., Khabarovsk 680042, Russian Federation

vlasova64@yandex.ru

Abstract. In this paper, comparative studies of the microstructure, mechanical characteristics and service life of a cutting insert made of submicron cemented carbide WC–10Co, obtained as a result of recycling VK10 cemented carbide by Electro Discharge Erosion (EDE) in oil, were carried out. The specific energy consumption directly for the formation of pulses in the process of EDE is to a relatively small value (5.7 kW·h/kg). Excess carbon formed as a result of oil pyrolysis during EDE was removed by heat treatment. The granulometric composition of the obtained powder and the microstructure of the particles were studied. It is shown that the particles of the resulting powder consist of plate-like WC grains with an average diameter of 0.46 μm and interlayers of cobalt. The WC–10Co cutting insert, obtained by sintering this powder in vacuum, was used for a comparative analysis of service life during fine turning of aluminum alloy D16T. As objects for comparative analysis, cutters equipped with blades made of industrial alloys VK8 and VK6OM of a similar design were used. The microstructure and mechanical characteristics of the experimental alloy and the analogues presented have been studied. On the basis of studies of the microstructure and chemical composition of the back surface of the cutting inserts, the wear mechanism of the cutters was analyzed. It is shown that the hardness of the alloys has the main effect on their wear resistance when cutting an aluminum alloy with the presented cutters. The influence of the hardness of the cutters on the surface roughness of the resulting part was also studied. The obtained submicron cemented carbide WC–10Co exhibits the highest hardness (1590 HV) and wear resistance of the presented samples due to the smallest WC grain diameter (0.59 μm).

Keywords: cemented carbide, service life, wear, recycling, electro discharge erosion

For citation: Dvornik M.I., Vlasova N.M. Comparative analysis of the tool life of submicron hard alloy WC–10Co sintered from powder obtained by electro discharge in oil. *Powder Metallurgy and Functional Coatings*. 2023;17(1):75–84. https://doi.org/10.17073/1997-308X-2023-1-75-84

Сравнительный анализ эксплуатационной стойкости субмикронного твердого сплава WC–10Co, спеченного из порошка, полученного электроэрозионным диспергированием в масле

М. И. Дворник, Н. М. Власова

Институт материаловедения Хабаровского федерального исследовательского центра
Дальневосточного отделения РАН
Россия, 680042, г. Хабаровск, ул. Тихоокеанская, 153

✉ vlasova64@yandex.ru

Аннотация. Проведены сравнительные исследования микроструктуры, механических характеристик и эксплуатационной стойкости режущей пластины из субмикронного твердого сплава WC–10Co, полученного в результате переработки отходов твердого сплава ВК10 электроэрозионным диспергированием (ЭЭД) в масле. Удельные затраты энергии непосредственно на формирование импульсов в процессе ЭЭД составили относительно небольшую величину (5,7 кВт·ч/кг). Избыток углерода, образованный в результате пиролиза масла при ЭЭД, был удален путем термообработки. Изучены гранулометрический состав полученного порошка и микроструктура его частиц. Показано, что частицы порошка состоят из вытянутых зерен WC ($d_{\text{ср}}$ = 0,46 мкм) и прослоек кобальта. Пластина WC–10Co для резца, полученная спеканием этого порошка в вакууме, была использована для сравнительного анализа эксплуатационной стойкости при чистовом точении алюминиевого сплава Д16Т. В качестве объектов для сравнительного анализа применяли резцы, оснащенные пластинами из промышленных сплавов ВК8 и ВК6ОМ аналогичной конструкции. Изучены микроструктура и механические характеристики экспериментального сплава и представленных аналогов. На основе исследований микроструктуры и химического состава задней поверхности режущих пластин был проанализирован механизм износа резцов. Показано, что твердость сплавов оказывает основное влияние на их износостойкость при резании алюминиевого сплава сравниваемыми резцами. Также исследовано влияние твердости резцов на шероховатость поверхности обрабатываемой детали. Полученный субмикронный твердый сплав WC–10Co обладает наивысшей твердостью (1590 HV) и лучшей износостойкостью из изученных образцов за счет наименьшего диаметра зерен WC (0,59 мкм).

Ключевые слова: твердый сплав, эксплуатационная стойкость, износ, переработка, электроэрозионное диспергирование

Для цитирования: Дворник М.И., Власова Н.М. Сравнительный анализ эксплуатационной стойкости субмикронного твердого сплава WC–10Co, спеченного из порошка, полученного электроэрозионным диспергированием в масле. *Известия вузов. Порошковая металлургия и функциональные покрытия*. 2023;17(1):75–84. https://doi.org/10.17073/1997-308X-2023-1-75-84

Introduction

Due to the combination of high indices of strength, hardness and wear resistance, tungsten-cobalt (WC–Co) cemented carbides are extensively used in industry [1–3]. Obtaining submicron and ultrafine grained cemented carbides of high hardness and wear resistance as well as reducing the costs of their production represent an urgent task nowadays [4; 5]. High cost of cemented carbides associated with the limited reserves of cobalt and tungsten. In the view of this, all cemented carbide wastes are recycled and used for the production of new articles. Owning to high hardness, strength and chemical stability, the cemented carbides are to be processed by costly chemical methods using hazardous and environmentally destructive chemicals [6–9]. One of the promising alternative methods for obtaining powders directly from pieces of material without using of hazardous reagents is Electro Discharge Erosion (EDE) [10–16].

The EDE method is based on the erosion of electrodes and the formation of particles during a spark discharge passing in a dielectric liquid. Under the impact of a spark discharge, the surface of the electrodes is heated up to ~10^4 K [17; 18] that results in the melting and boiling of the initial material inside a vapor bubble formed upon the boiling of dielectric liquid. After the spark discharge passes, the vapor bubble collapses, the molten and boiling material is ejected into the interelectrode gap and cooled at a rate of 10^6–10^9 K/s. Cooling results in the formation of ultrafine-grained particles of predominantly spherical shape.

Researchers have already developed a technology for processing the alloy, including the production of powders by EDE method, thermochemical treatment and vacuum sintering [14; 15]. Due to a small grain size, the obtained samples of cemented carbides are not inferior to their analogues, obtained by other methods, in terms of the combination of hardness and fracture toughness. However, no works on the research of the service life of the cutting tools equipped with these carbides have been found in the available literature, which makes it difficult to identify the prospects for their application. This problem applies to all ultrafine-grained and submicron carbides whose production has commenced in recent decades.

To answer the question about the prospects of using submicron cemented carbides produced by sintering the powders obtained by EDE and other methods, it is required to research their service life in comparison with their analogues during the mechanical processing of the material in the conditions corresponding to these carbides. The closest analogues of submicron cemented carbides are medium-grained and extra fine-grained cemented carbides produced by modern industry and applied for the treatment of non-ferrous alloys.

The paper was aimed at the research of wear resistance of submicron cemented carbide, produced by sintering of the powder, obtained by recycling by EDE method, and its analogues during the cutting of aluminum alloy.

Methods

The powder for the initial carbide was obtained by electro discharge erosion of VK10 (90 % WC + 10 % Co)

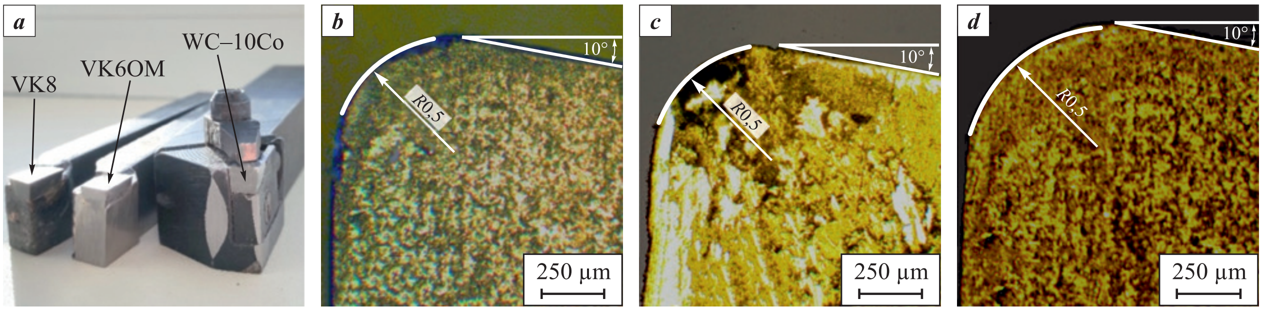

Fig. 1. Cutters studied for wear resistance (***a***) and the top view of cutting inserts made of VK8 (***b***), VK6OM (***c***), and WC–10Co (***d***) alloys

Рис. 1. Исследованные на износостойкость резцы (***a***) и вид сверху режущих пластин из сплава ВК8 (***b***), ВК6ОМ (*c*) и WC–10Co (***d***)

medium-grained carbide. The refined carbide inserts with the dimensions of 10–20 mm and a total initial weight of 50 g were subjected to electro discharge erosion for 60 min on a specially designed plant [14; 15]. The pulse generator parameters are as follows: average pulse energy – 5 J, pulse frequency – 35 Hz, pulse voltage – 250 V, used liquid – dielectric oil (GK-1), EDE duration – 1 h. The energy expended directly for the passage of power pulses was calculated based on the current-voltage characteristics, which were measured by means of analogue-to-digital converter connected to the anode and cathode through a voltage divider.

After EDE, the powder was collected as a deposit. The obtained paste was placed in a ceramic crucible and subjected to vacuum drying at a temperature $t = 500$ °C in "Carbolite STF" vacuum furnace. Afterwards, the powder was ground for 5 min by means of "Retsch PM 400" grinder, weighed, analyzed for carbon content using "Emia 320V2" analyzer, and excess carbon was removed by heating the powder at $t = 1000$ °C for 20 min in CO_2 environment. The granulometric analysis was performed by means of "Analysette 22 Microtec" analyzer. The microstructure of the particles was studied after they were mixed with epoxy resin and polished. A batch of the obtained powder was mixed with a binder (benzine-based adhesive), then dried (the concentration of the binder was 1 wt. %), granulated, and 3 blanks were pressed from it. The blanks were sintered at $t = 1410$ °C in a vacuum furnace for 1 h.

Standard straight-turning side cutters equipped with brazed inserts made of VK8 and VK6OM hard alloys were used as analogues for the analysis of wear resistance. A cutting insert of experimental WC–10Co alloy with the same shape of cutting edge was made and fixed mechanically (Fig. 1, *a*). The main parameters of the used cutters were the same: primary back clearance angle – 10°, primary front clearance angle – 0°, primary entering angle – 80°, root radius – 0,5 mm (Fig. 1, *b*–*d*).

The microstructure of the samples was studied after grinding and polishing of the surface. The average WC grain diameter was calculated according to the standard method (ASTM E112-13:2021), namely by intercept method. Vickers hardness of all alloys was measured by means of HVS-50 hardness meter (error 2 %) under load $P = 294$ H (30 kgf). Fracture toughness (K_{1C}) calculated according to the total length of the cracks ($\sum l$) under Palmqvist scheme (ISO 28079) using Shetty equation:

$$K_{1C} = 0.028\sqrt{HV\frac{P}{\sum l}}.$$

The service life of the cutters was studied by fine turning of aluminum alloy D16T, which is one of the most demanded structural materials for the manufacture of parts in the aerospace and shipbuilding industry. The turning of the blank (Fig. 2) was performed on 16K20 turner under the same conditions until the wear of back face of 100 μm was reached. The maximum possible cutting speed $V = 300 \pm 20$ m/min, ensured by this turner, was chosen. The depth of cut was 0.5 mm, the feed was 0.07 mm/rev. Back surface wear was measured by means of "Altami" optical

Fig. 2. The machined blank and the cutter during turning

Рис. 2. Обрабатываемая заготовка и резец в процессе точения microscope every 15 min (4.5 km) for VK8 alloy and every 45 min (13.5 km) for VK6OM and WC–10Co alloys. The microstructure of the back surface of the cutting inserts was studied using "Tescan Vega" scanning microscope. The surface of the cutting inserts was previously cleaned with alkali to remove build-up and adhered chips. The content of oxygen and metals in the back surface of the cutter was studied using "Oxford X-Max 80 SDD-EDXS" energy dispersive *X*-ray fluorescence detector.

Results and Discussion

As a result of recycling VK10 cemented carbide by Electro Discharge Erosion (EDE) in oil, spherical microparticles and agglomerates of nanodispersed particles mixed with free carbon, formed as a result of pyrolysis of hydrocarbons, were obtained. The process rate was 32 g/h, the specific energy consumption for the passage of current pulses through the unit made up 5.7 kW·h per 1 kg of powder. If required, the process rate can be increased many times by increasing the power of the pulse generator [16].

The phase composition of the obtained powder after drying at a temperature of 600 °C does not differ from the original carbide (WC + Co). The total carbon content in the powder increased to 8.1 % due to the formation of free carbon during the oil pyrolysis. Using the proven methodology [14], excess carbon (2.6 %) was totally removed by means of powder annealing at $t = 1000$ °C in vacuum furnace, filled with the equivalent CO_2 content. The powder obtained after the removal of free carbon, consisted of WC–Co particles (Fig. 3, *a*), the average diameter of which was 11.2 μm (Fig. 3, *b*). The spherical particles were plate-like WC grains with an average diameter of 0.46 μm (Fig. 3, *c*), the space between which was filled with cobalt.

When sintering WC–10Co carbide, the average diameter of WC grains increased up to 0.59 μm (Fig. 4, *a*). After sintering, WC–10Co cutting insert was produced, then it was mechanically fastened on the holder and turned. The reduced rigidity of the insert with mechanical fastening does not cause deformations that impact the wear of the cutters, since cutting forces do not reach significant values with the selected cutting mode (fine turning). Due to the low hardness of the alloy being processed and the small depth of cut (finishing), the resulting forces could not cause cracking of the brazed inserts and displacement of the insert with mechanical fastening. The characteristics of alloy materials, which primarily depend on their composition and microstructure, exert a major influence on the wear resistance of the cutter.

The hard alloys used are distinguished from each other by their cobalt content, the presence of TaC in VK6OM alloy, as well as grain shape and size. Since the selected alloys differ slightly in their chemical composition, the mechanical characteristics of the alloys, which depend on the grain diameter and cobalt content, have a major influence on the wear rate. The microstructure of the alloys (Fig. 4) clearly shows that VK8 alloy exhibits the largest grain diameter and the experimental WC–10Co alloy – the smallest.

Using data on the average grain diameter, mass fraction of cobalt (see the Table) and the simple ratios for calculating the volume fraction of cobalt and adjacency, the theoretical hardness values for the presented hard alloys were calculated based on the Gerland and Lee model [19; 20]. The obtained results are in satisfactory agreements with the experimental values (Fig. 5, *a*). Medium-grained VK8 alloy exhibits the lowest hardness. WC–10Co and VK6OM submicron alloys have approximately equal values *HV*. The high hardness of WC–10Co alloy is provided by a smaller average

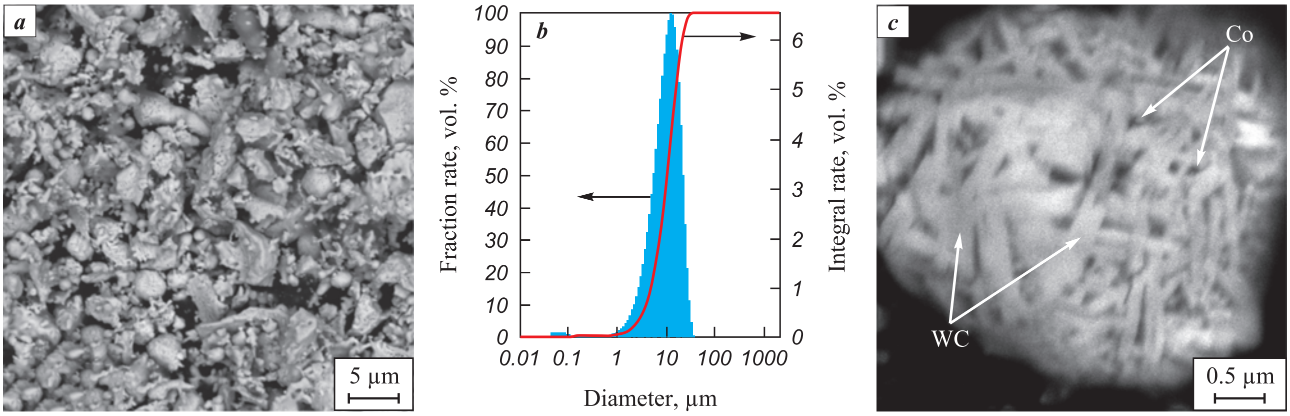

Fig. 3. Powder morphology (***a***), its granulometric composition (***b***) and particle microstructure (***c***) after drying and heat treatment

Рис. 3. Морфология порошка (***a***), его гранулометрический состав (***b***) и микроструктура частицы (***c***) после высушивания и термообработки grain diameter, despite the higher cobalt content compared to VK6OM alloy. VK8 alloy is characterized by the highest fracture toughness among the presented alloys, VK6OM alloy is characterized by the lowest fracture toughness due to the low cobalt content. The fracture toughness of experimental WC–10Co alloy turned out to be slightly higher than that of VK6OM alloy (Fig. 5, *b*) due to the higher cobalt content and the presence of plate-like WC grains, which improve the overall characteristics of the alloy [14; 21]. The conducted tests were selected in accordance with the application of VK6OM and VK8 alloys used, among other things, for turning aluminum alloys.

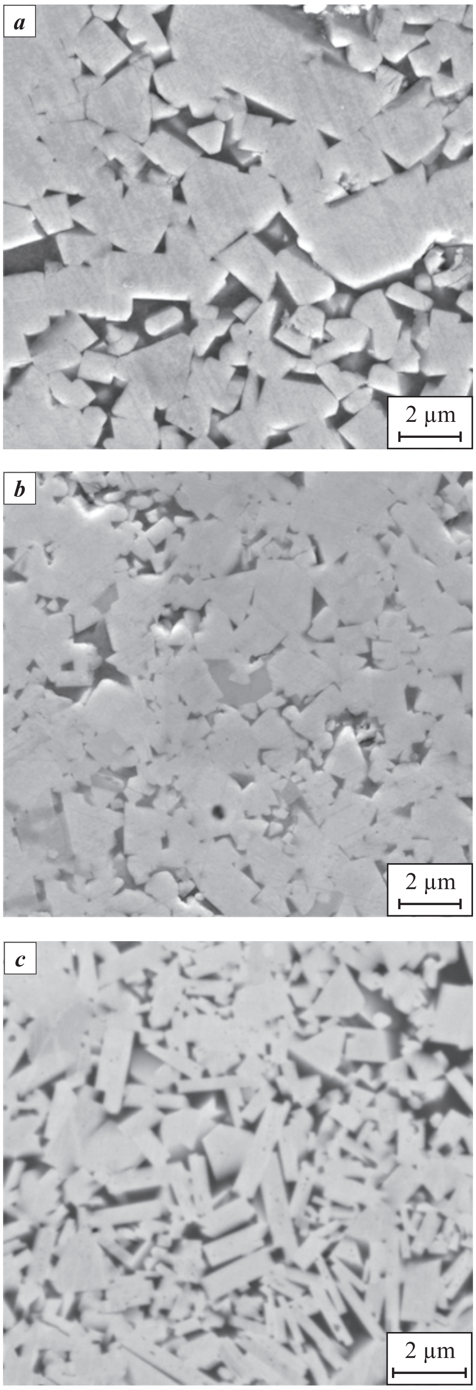

Fig. 4. The microstructures of hard alloys WC–10Co (***a***), VK8 (***b***), and VK6OM (***c***)

Рис. 4. Микроструктуры твердых сплавов WC–10Co (***a***), ВК8 (***b***) и ВК6ОМ (***c***)

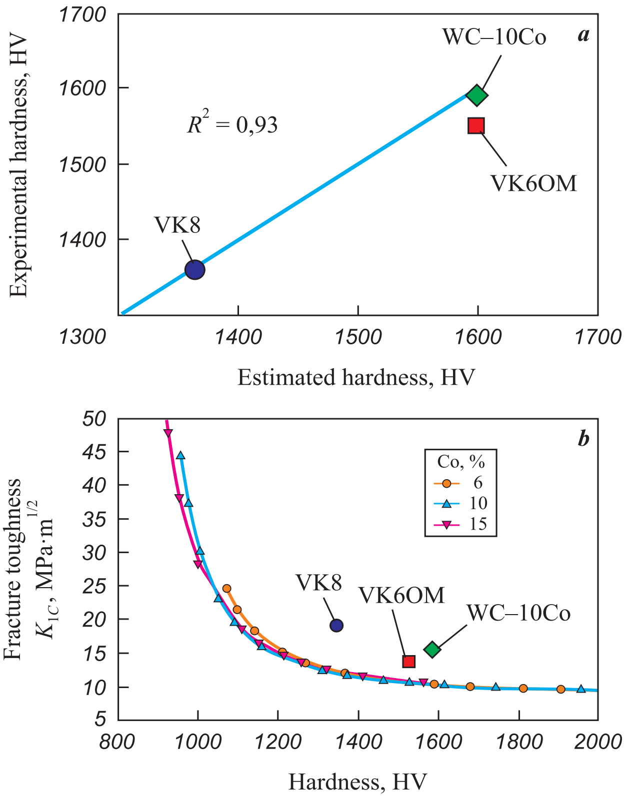

Fig. 5. The comparison of experimental values (symbols) and estimated values (straight line) of hardness (***a***) and dependence of fracture toughness of the studied alloys and their analogues [23] on hardness (***b***)

Рис. 5. Сопоставление экспериментальных (значки) и расчетных (прямая) значений твердости (***a***) и зависимость вязкости разрушения исследуемых сплавов и их аналогов [23] от твердости (***b***)

Main characteristics of alloys

Основные характеристики сплавов

Alloy	Cobalt content, wt. %	Average grain diameter of WC, μm	Hardness, HV	Fracture toughness, MPa·m$^{1/2}$
VK8	8	1.54	1360	19.0
VK6OM	6	1.09	1550	13.2
WC–10Co	10	0.59	1590	14.1

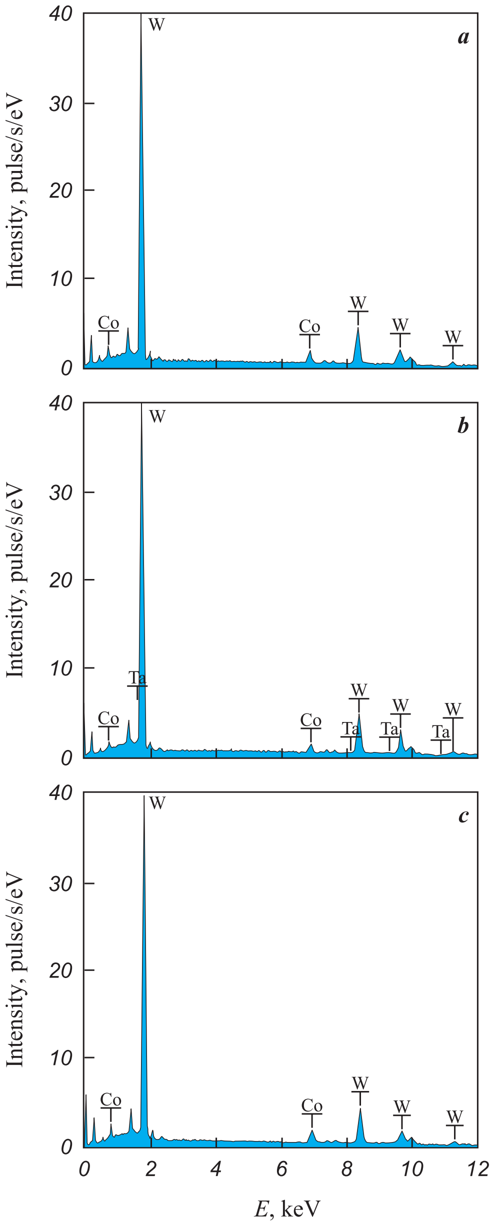

Alloy	Fraction, wt. %		
	W	Co	Ta
VK8	94.6 ± 0.2	6.4 ± 0.2	–
VK6OM	93.3 ± 0.5	4.6 ± 0.1	2.1 ± 0.5
WC–10Co	92.0 ± 0.1	8.0 ± 0.1	–

Fig. 6. The results of energy dispersive analysis of the back surface of VK8 (***a***), VK6OM (***b***) and WC–10Co (***c***) cutting inserts after wear resistance testing

Рис. 6. Результаты энергодисперсионного анализа задней поверхности режущих пластин ВК8 (***а***), ВК6ОМ (***б***) и WC–10Co (***в***) после испытания на износостойкость

The Mechanism of Wear

According to modern researches [22], when turning an aluminum alloy, the adhesive, diffusion and abrasive wear of carbide cutting inserts is observed. The temperature of the cutter tip under close turning conditions (cutting speed of 360 m/min) is 315 °C [22]. Increased temperature and high contact pressure on the tip of the cutter on the side of the machined workpiece result in mechanical sticking or fusing of the machined aluminum alloy on the back surface of the cutter. The diffusion wear is insignificant in such conditions, since the solubility of cobalt in aluminum is low at this temperature [24]. An adhesive layer is formed under the build-up surface, it contains the compounds of cobalt, tungsten, aluminum and their oxides, which are removed during cutting. The formed build-up is involved in cutting and is periodically cut off. When it is cut, the wear of the edge and the back surface of the cutter occurs.

Upon cutting, the cobalt layers are removed first because of their lower hardness and greater chemical reactivity. The energy-dispersive analysis of the studied sections confirmed that there was a decrease in the concentration of cobalt on the back surface of the cutter by a constant value of 25 % of its initial content (Fig. 6). Since the decrease in the fraction of cobalt indicates the depth of its location, it can be concluded that it is removed to a certain depth, regardless of the size of WC grains. The removal of cobalt results in the formation of microroughnesses from protruding carbide grains, which are clearly visible at high magnification (Fig. 7, *b*, *d*, *f*). The results of energy-dispersive analysis also indicate that the components of the aluminum alloy do not penetrate into the surface layers of the hard alloy (Fig. 6). The oxygen content in the surface layers of wear (1.5–2.0 %) exceeds its concentration in the surface of alloy (1.1 %), which may indicate oxygen diffusion and oxide layer formation.

The wear surface of VK8 alloy (Fig. 7, *a*, *b*) shows shallow, smooth grooves with slip bands in them, formed by shearing off the adhesive layer. In the VK6OM and WC–10Co alloys, no grooves are detected even at the highest magnification (Fig. 7, *d*, *f*). Namely, the removal of components of harder alloys (VK6OM and WC–10Co) occurs only in a layer less than 1 μm thick. The wear of the edge of VK8 hard alloy can also be noticed (Fig. 7, *a*). The wear of the edge of VK6OM and WC–10Co alloys is insignificant, since their hardness is higher.

The kinetic dependence of increase of wear value along the back face on the covered distance consists of cutting-in and linear wear sections (Fig. 8, *a*). The wear of the studied alloys at the initial stage differs insignificantly (~0.03 mm). Deviations from a straight line in a linear section are also insignificant. An increase in hardness results in an increase in service life of hard alloys (Fig. 8, *b*), what is typical for micro-abrasive wear. VK8 alloy has the least service life (the reciprocal of wear) (90 min). Due to the higher

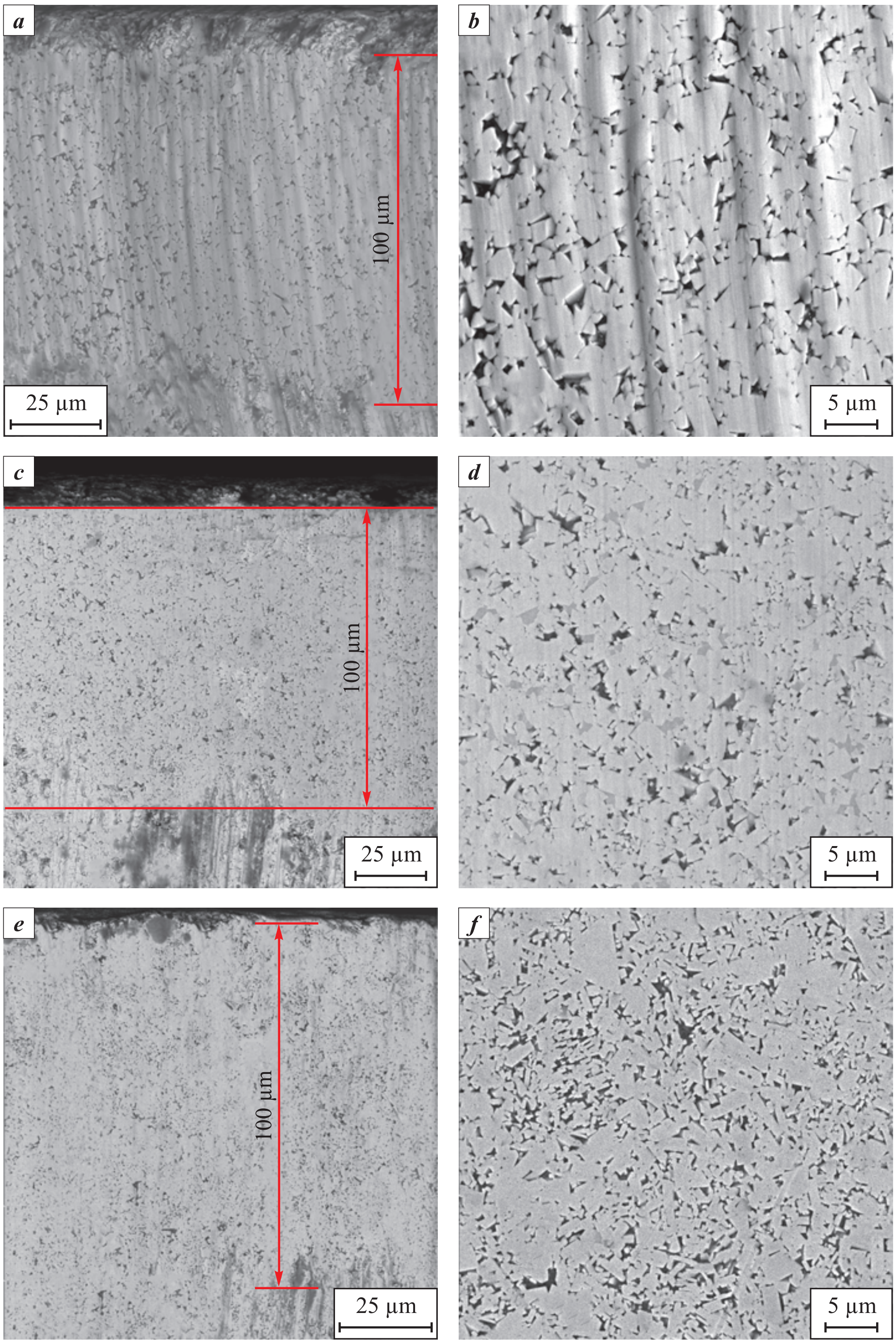

Fig. 7. The photos of the worn back surface of VK8 (***a***, ***b***), VK6OM (***c***, ***d***) and WC–10Co (***e***, ***f***) cutters after testing

Рис. 7. Фотографии изношенной задней поверхности резцов ВК8 (***a***, ***b***), ВК6ОМ (***c***, ***d***) и WC–10Co (***e***, ***f***) после испытаний

hardness, the service life of experimental WC–10Co alloy (360 min) exceeds that of VK6OM alloy (315 min) by 45 min. The service life of all studied hard alloys is sufficiently high (>35 min) and meets the standard requirements (GOST 5688-61). However, a further increase in tool life is necessary to save cutters and time. Due to the high hardness, the cutting distance (about 100 km) covered by cutters equipped with VK6OM and WC–10Co alloys turned out to be longer than the distance (20 km) covered in a similar study (ISO K10 Sandvik Coromant carbide) [25].

The average wear rate in the linear section (normal wear) decreases with increasing hardness according to the Archard law (Fig. 8, *c*). This is consistent with modern research showing an increase in wear resistance along with an increase in hardness as a result of a reduction in the average grain diameter in the hard alloys [5; 22]. For the aforementioned reasons, the wear resistance of hard alloys is to decrease with an increase in fracture toughness both upon micro-abrasive and adhesive wear [23].

The roughness of a workpiece depends on cutting speed, depth of cut, feed, rigidity of the technological system, hardness and strength of the cutting edge.

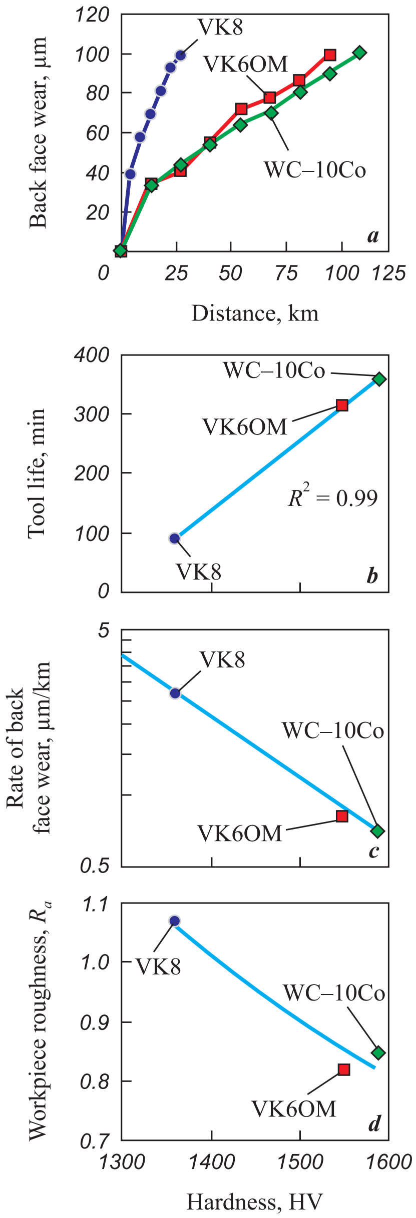

Fig. 8. The dependence of hard alloy wear on the covered distance (***a***); the dependencies of tool life of the hard alloy (***b***), the rates of wear along its back face (***c***) and the workpiece roughness (***d***) on the hardness of the cutting inserts

Рис. 8. Зависимость износа твердого сплава от пройденного пути (***a***); зависимости периода стойкости твердого сплава (***b***), скорости износа по его задней грани (***c***) и шероховатости обрабатываемой детали (***d***) от твердости режущих пластин

After machining, the profiles of the workpiece differ in roughness height only. The back surface of VK8 alloy contains a number of grooves, being caused by deformation due to the relatively low hardness of the alloy. In addition, the edge of the cutter is deformed that results in the increase of cutting force and the deformation of the cutter tip. As a result, the surface roughness of the workpiece during the machining with VK8 alloy increases up to $R_a = 1.07$ µm. Almost no grooves can be seen on the back surface of VK6OM and WC–10Co. There is no change in the edges of these cutters, which is to facilitate the reduction of the workpiece roughness as well. Upon machining using the cutters equipped with VK6OM and WC–10Co, the workpiece roughness makes up $R_a = 0.85$ and 0.82 correspondingly.

Conclusion

This paper presents a method for obtaining WC–10Co cemented carbide, which outperforms one of the hardest industrial hard alloys VK6OM in terms of the service life due to its higher hardness, from scrap. As a result of Electro Discharge Erosion (EDE) of the medium-grained VK10 alloy scrap, a powder with the required phase composition is formed. The specific energy consumption directly for the formation of pulses made up 5.7 kW·h/kg. Submicron WC–10Co alloy with an average grain diameter of 0.59 µm and increased hardness (1590 HV) was obtained by sintering the produced powder after its heat treatment.

A comparative analysis of tool life upon turning of aluminum alloy with the experimental submicron alloy and its industrial analogues (VK8 and VK6OM) showed that the tool life increases in proportion to the increase in hardness of the hard alloys used. Due to high hardness, the tool life of experimental WC–10Co alloy (360 min) turned out to be higher than that of the extra fine-grained VK6OM alloy (315 min) and VK8 alloy (90 min). The workpiece roughness after turning with harder alloys (VK6OM and WC–10Co) was lower ($R_a = 0.85$ and 0.82 correspondingly) than the workpiece roughness exhibited by turning with VK8 alloy ($R_a = 1.07$) due to the higher hardness.

References / Список литературы

1. Prakash Leo. Fundamentals and general applications of hardmetals. In: *Comprehensive Hard Materials*. 2014;1: 29–90.https://doi.org/10.1016/B978-0-08-096527-7.00002-7

2. Levashov E.A., Panov V.S., Konyashin I.Yu. History of domestic hard alloys. *Powder Metallurgy and Functional Coatings*. 2017;(3):14–21. (In Russ.). https://doi.org/10.17073/1997-308X-2017-3-14-21

Левашов Е.А., Панов В.С., Коняшин И.Ю. История отечественных твердых сплавов. *Известия вузов. По-*

рошковая металлургия и функциональные покрытия. 2017;(3):14–21.
https://doi.org/10.17073/1997-308X-2017-3-14-21

3. Ortner H., Kolaska H., Ettmayer P. The history of the technological progress of hardmetals. *International Journal of Refractory Metals and Hard Materials*. 2014;44(1):148–159.
https://doi.org/10.1016/j.ijrmhm.2013.07.014
4. Wang B., Wang Z., Yin Z., Yuan J., Jia J. Preparation and properties of the VC/Cr_3C_2/TaC doped ultrafine WC–Co tool material by spark plasma sintering. *Journal of Alloys and Compounds*. 2020;816(2):152598.
https://doi.org/10.1016/j.jallcom.2019.152598
5. Dvornik M.I., Mokritskii B.Ya., Zaitsev A.V. Comparative analysis of micro-abrasive wear resistance of traditional hard alloys and submicron hard alloy WC–8Co–1Cr_3C_2. *Voprosy materialovedeniya*. 2015;(1(81)):45–51. (In Russ.).

   Дворник М.И., Мокрицкий Б.Я., Зайцев А.В. Сравнительный анализ микроабразивной износостойкости традиционных твердых сплавов и субмикронного твердого сплава WC–8Co–1Cr_3C_2. *Вопросы материаловедения*. 2015;(1(81)):45–51.
6. Katiyar P.K., Randhawa N.S. A comprehensive review on recycling methods for cemented tungsten carbide scraps highlighting the electrochemical techniques. *International Journal of Refractory Metals and Hard Materials*. 2020;90(2012):105251.
https://doi.org/10.1016/j.ijrmhm.2020.105251
7. Sun F., Zhao Z., Chen X. Recovery of WC and Co from cemented carbide scraps by remelting and electrodissolution. *International Journal of Refractory Metals and Hard Materials*. 2019;80:23–29.
https://doi.org/10.1016/j.ijrmhm.2018.12.014
8. Zhang Q., Xi X., Nie Z., Zhang L., Ma L. Electrochemical dissolution of cemented carbide scrap and electrochemical preparation of tungsten and cobalt metals. *International Journal of Refractory Metals and Hard Materials*. 2019;79: 145–153. https://doi.org/10.1016/j.ijrmhm.2018.12.001
9. Shemi A., Magumise A., Ndlovu S., Sacks N. Recycling of tungsten carbide scrap metal: A review of recycling methods and future prospects. *Minerals Engineering*. 2018;122: 195–205. https://doi.org/10.1016/j.mineng.2018.03.036
10. Dvornik M.I. Nanostructured WC–Co particles produced by carbonization of spark eroded powder: Synthesis and characterization. *International Journal of Refractory Metals and Hard Materials*. 2010;28(4):523–528.
https://doi.org/10.1016/j.ijrmhm.2010.02.011
11. Kabirinia F., Shabgard M., Salman Tabrizi N. Study on effect of dielectric gas type on electrical discharge erosion synthesis of tungsten carbide nanopowder. *Applied Physics A*. 2019;125(9):610.
https://doi.org/10.1007/s00339-019-2888-y
12. Kumar P., Singh P.K., Kumar D., Prakash V., Hussain M., Das A.K. A novel application of micro-EDM process for the generation of nickel nanoparticles with different shapes. *Materials and Manufacturing Processes*. 2017;32(5)564–572.
https://doi.org/10.1080/10426914.2016.1244832
13. Mondal S., Singh P.K., Bishwakarma H., Mishra S.K., Gupta H.S., Mishra A.K., Das A.K. A facile green synthesis of tungsten nanoparticles through Micro-EDM. *Materials Today: Proceedings*. 2019;11(2):761–766.
https://doi.org/10.1016/j.matpr.2019.03.039
14. Dvornik M.I., Mikhailenko E.A., Nikolenko S.V. Development of a method for producing submicron cemented carbide from a powder obtained by electrical discharge erosion of scrap in oil. *Powder Technology*. 2021;383(3):175–182.
https://doi.org/10.1016/j.powtec.2021.01.048
15. Dvornik M.I., Mikhailenko E.A. Production of WC–15Co ultrafine-grained hard alloy from powder obtained by the electroerosive dispersion of VK15 alloy wastes in water. *Russian Journal of Non-Ferrous Metals*. 2021;62(1):97–106.
https://doi.org/10.3103/S1067821221010065
16. Fominskii L.P. Method for obtaining powders and pastes: Copyright certificate 1107965 (USSR). 1984. (In Russ.).

    Фоминский Л.П. Способ получения порошков и паст: A.c. 1107965 (СССР). 1984.
17. Li S., Yin X., Jia Z., Li Z., Han L. Modeling of plasma temperature distribution during micro-EDM for silicon single crystal. *The International Journal of Advanced Manufacturing Technology*. 2020;107(3):1731–1739.
https://doi.org/10.1007/s00170-020-05135-x
18. Salah N.B., Ghanem F., Atig K.B. Numerical study of thermal aspects of electric discharge machining process. *International Journal of Machine Tools and Manufacture*. 2006;46(7–8):908–911.
https://doi.org/10.1016/j.ijmachtools.2005.04.022
19. Lee H.C., Gurland J. Hardness and deformation of cemented tungsten carbide. *Materials Science and Engineering*. 1978;33(1):125–133.
https://doi.org/10.1016/0025-5416(78)90163-5
20. Dvornik M.I., Zaitsev A.V. Variation in strength, hardness, and fracture toughness in transition from medium-grained to ultrafine hard alloy. *Russian Journal of Non-Ferrous Metals*. 2018;59(5):563–569.
https://doi.org/10.3103/S1067821218050024
21. Yang Q., Deng D., Li J., Chen L., Guo S., Liu J., Chen H. Fabrication and mechanical properties of WC–10Co cemented carbides with plate-like WC grains. *Journal of Alloys and Compounds*. 2019;803:860–865.
https://doi.org/10.1016/j.jallcom.2019.06.328
22. List G., Nouari M., Géhin D., Gomez S., Manaud J.P., Le Petitcorps Y., Girot F. Wear behaviour of cemented carbide tools in dry machining of aluminium alloy. *Wear*. 2005;259(7):1177–1189.
https://doi.org/10.1016/j.wear.2005.02.056
23. Roebuck B., Gant A.J., Gee M.G. Abrasion and toughness property maps for WC/Co hardmetals. *Powder Metallurgy*. 2007;50(2):111–114.
https://doi.org/10.1179/174329007X211526
24. Nouari M., List G., Girot F., Coupard D. Experimental analysis and optimisation of tool wear in dry machining of aluminium alloys. *Wear*. 2003 255(7):1359–1368.
https://doi.org/10.1016/S0043-1648(03)00105-4
25. Umroh B., Muhathir Darianto. The optimum cutting condition when high speed turning of aluminum alloy using uncoated carbide. *IOP Conference Series Materials Science and Engineering*. 2019;505(1):012041.
https://doi.org/10.1088/1757-899X/505/1/012041

Information about the Authors

Maksim I. Dvornik – Cand. Sci. (Eng.), Senior Researcher, Head of the Laboratory of powder metallurgy of the Institute of Materials Science of the Khabarovsk Federal Research Center of the Far Eastern Branch of the Russian Academy of Sciences
ORCID: 0000-0002-1216-4438
E-mail: maxxxx80@mail.ru

Nuriya M. Vlasova – Cand. Sci. (Eng.), Researcher of the Laboratory of powder metallurgy of the Institute of Materials Science of the Khabarovsk Federal Research Center of the Far Eastern Branch of the Russian Academy of Sciences
ORCID: 0000-0003-0198-0912
E-mail: vlasova64@yandex.ru

Сведения об авторах

Максим Иванович Дворник – к.т.н., ст. науч. сотрудник, заведующий лабораторией порошковой металлургии, Институт материаловедения Хабаровского федерального исследовательского центра Дальневосточного отделения РАН
ORCID: 0000-0002-1216-4438
E-mail: maxxxx80@mail.ru

Нурия Мунавировна Власова – к.т.н., науч. сотрудник лаборатории порошковой металлургии, Институт материаловедения Хабаровского федерального исследовательского центра Дальневосточного отделения РАН
ORCID: 0000-0003-0198-0912
E-mail: vlasova64@yandex.ru

Contribution of the Authors

M. I. Dvornik – formation of the main concept, setting the goal and objectives of the study, conducting experiments, processing the results of the research, preparing the text, analyzing the results of the research, formulation of the conclusions.
N. M. Vlasova – conducting experiments, testing samples, correcting the text, processing of the research results.

Вклад авторов

М. И. Дворник – формирование основной концепции, постановка цели и задачи исследования, проведение экспериментов, обработка результатов исследований, подготовка текста, анализ результатов исследований, формулировка выводов.
М.Н. Власова – проведение экспериментов, проведение испытаний образцов, корректировка текста.

Received 06.04.2022
Revised 20.06.2022
Accepted 23.06.2022

Статья поступила 06.04.2022 г.
Доработана 20.06.2022 г.
Принята к публикации 23.06.2022 г.

Зарегистрирован Федеральной службой по надзору
в сфере связи, информационных технологий
и массовых коммуникаций.
Свидетельство о регистрации **ПИ № ФС77-79230**

Журнал распространяется агентством «Урал-Пресс»
Подписной индекс: 80752 (печатная версия)
05108 (электронная версия)